Baryons, salt and popcorn in holographic QCD

Matthew Kevin Ian David Elliot-Ripley

A Thesis presented for the degree of
Doctor of Philosophy

Centre for Particle Theory
Department of Mathematical Sciences
Durham University
United Kingdom

May 2017

Baryons, salt and popcorn in holographic QCD

Matthew Kevin Ian David Elliot-Ripley

Submitted for the degree of Doctor of Philosophy

May 2017

Abstract:

The Sakai-Sugimoto model [1, 2] is the leading model of holographic QCD. It has an effective five-dimensional description in which baryons correspond to the bulk topological solitons of a Yang-Mills-Chern-Simons theory. However, the large dimensionality of the model means studying soliton solutions either analytically or numerically is difficult.

Sakai-Sugimoto solitons in the high density limit should provide an analogue of cold, dense QCD. Two competing theories for high-density solutions are the dyon salt model [3], in which the appropriate crystal is a salt-like arrangement of dyons, and the baryonic popcorn model [4, 5] in which a series of transitions occurs where the three-dimensional soliton crystal develops extra layers in the holographic direction.

In this thesis we consider a range of low-dimensional analogues and approximations to the Sakai-Sugimoto model. We first investigate an $O(3)$ sigma model stabilised by vector mesons, and a baby Skyrme model in pure AdS spacetime, before moving on to consider homogeneous ansätze in both the holographic baby Skyrme and full Sakai-Sugimoto models. In each case we look for analogues of the dyon salt and baryonic popcorn configurations, and find evidence for new features in the high-density regime of holographic QCD.

Declaration

The work in this thesis is based on research carried out in the Centre for Particle Theory, Department of Mathematical Sciences, Durham University, United Kingdom. No part of this thesis has been submitted elsewhere for any other degree or qualification and it is all my own work unless referenced to the contrary in the text.

The material presented in this thesis relates to four published papers [6, 7, 8, 9] corresponding to Chapters 2, 3, 4 and 5 respectively. The first and third of these papers consist entirely of my own work, and the other two were written as collaborations.

Acknowledgements

I would like to thank my family, friends and colleagues for their support during my postgraduate study at Durham University. In particular I would like to thank my supervisor, Paul; my office-mates Sam, Becca, Richard, Alex, Vaios and Xin; former PhD students Andy, Tom and Paul for proof-reading thesis drafts; paper co-authors Tom, Paul and Marija; my housemates Lizzie, Jules, Helen and David; the members of the DST theatre companies Ooook! Productions, Duck in a Hat and DULOG; Alyson and co. at The Woolly Workshop; and, of course, my parents.

Finally, I would like to thank Andrew Frankenburg for setting me on this path in the first place.

Contents

List of Figures

List of Tables

Chapter 1

Introduction

Solitons are solitary waves, obtained as the solutions to certain classes of nonlinear partial differential equations. Loosely speaking, they are spatially localised waves of fixed form which can interact with other solitons and emerge from collisions unchanged. Solitons were first observed in 1834 by Scottish engineer John Scott Russell in the form of bow waves on the Union Canal [10]. Such solitary waves were later found mathematically, in 1895, as nonlinear solutions to the Korteweg-de Vries equation [11].

The existence and stability of topological solitons can be attributed to topological properties, often linked to boundary conditions of the system in question. To each topological soliton solution one can assign an invariant, often integer-valued, known as the topological charge or soliton number. This allows us to divide the space of solutions into distinct classes. Solutions from different topological charge sectors cannot be smoothly deformed into each other: more specifically they cannot be smoothly deformed to a vacuum solution, thus providing their stability. Solitons of this form were proposed as an approximate model of nuclear physics by Tony Skyrme [12, 13] to describe baryons using a (3+1)-dimensional family of solitons known as Skyrmions. The study of topological solitons has become an important aspect across a broad range of physics, such as in the context of superfluids [14] and superconductors [15] in condensed matter physics, cosmic strings [16] and magnetic monopoles [17, 18] in cosmology, and even protein folding [19, 20] in biological physics.

In this introductory chapter we will begin by introducing four prototypical examples of topological solitons in up to 4 spatial dimensions and use them to introduce some of

the key mathematical features of soliton theory that will be used in this thesis. We will then introduce the idea of solitons in the context of holographic QCD, with particular reference to the Sakai-Sugimoto model.

1.1 Solitons in 1-d: kinks

We start with a $(1+1)$-dimensional model given in terms of a single scalar field ϕ, defined by the Lagrangian density

$$\mathcal{L} = -\frac{1}{2}\partial_\mu\phi\partial^\mu\phi - U(\phi)\,. \tag{1.1.1}$$

where $U(\phi)$ is some potential term (note we use the "mostly plus" metric convention $\eta_{00} = -1$, $\eta_{ij} = \delta_{ij}$, which we will use throughout the thesis). For $U(\phi) = 1 - \cos\phi$ this is called the sine-Gordon model [21], and the associated field equation and static energy for this model are given by

$$-\partial_\mu\partial^\mu\phi + \sin\phi = 0\,, \tag{1.1.2}$$

$$E = \int_{-\infty}^{\infty}\left\{\frac{1}{2}(\phi')^2 + (1-\cos\phi)\right\}dx\,. \tag{1.1.3}$$

This system has vacua whenever $U(\phi) = 0$ i.e. $\phi = 2\pi n$, $n \in \mathbb{Z}$. The presence of multiple vacua gives rise to topological soliton solutions which interpolate between different vacua. In 1-dimension, such solitons are known as kinks. The topological charge of the kink is given by

$$N = \frac{\phi_+ - \phi_-}{2\pi} = \frac{1}{2\pi}\int_{-\infty}^{\infty}\phi'\,dx\,, \tag{1.1.4}$$

where $\phi_\pm$ are the vacuum values the field interpolates between as $x \to \pm\infty$. The system is invariant under transformations of the form $\phi \to \phi \pm 2n\pi$, so we can always perform such a transformation to set $\phi_- = 0$. Solutions with $N < 0$ are known as anti-kinks.

We now introduce the first important concept in soliton theory: that of the Bogomolny bound [22]. This is where we use the topological properties of the system to place a

lower bound on the static energy (1.1.3). Writing $U(\phi) = 1 - \cos\phi$ we have

$$\begin{aligned} & \left(\frac{1}{\sqrt{2}}\phi' \pm \sqrt{U(\phi)}\right)^2 \geq 0 \\ \Rightarrow \quad & \frac{1}{2}(\phi')^2 + U(\phi) \geq \pm\sqrt{2U(\phi)}\phi' \\ \Rightarrow \quad & \frac{1}{2}(\phi')^2 + U(\phi) \geq \left|\sqrt{2U(\phi)}\phi'\right| \end{aligned} \tag{1.1.5}$$

where in the second line we have expanded the square. We can then integrate over the full spatial domain, identifying the left-hand side with the static energy (1.1.3) to obtain

$$\begin{aligned} E = \int_{-\infty}^{\infty}\left\{\frac{1}{2}(\phi')^2 + U(\phi)\right\}dx \quad & \geq \int_{-\infty}^{\infty}\left|\sqrt{2U(\phi)}\phi'\right| dx \\ & = \int_0^{\phi_+}\left|\sqrt{2U(\phi)}\right| d\phi \\ & = \int_0^{2\pi N} 2\left|\sin\frac{\phi}{2}\right| d\phi = 8|N|\,. \end{aligned} \tag{1.1.6}$$

In the second and third lines we have performed a change of variable in the integration, identified $\phi_+ = 2\pi N$ from (1.1.4), substituted the explicit form for $U(\phi)$ back in and computed the integral using N-fold symmetry of the integrand.

Such bounds are a typical feature of models that permit topological soliton solutions, as we shall see in future examples. Saturation of the Bogomolny bound gives us a first-order Bogomolny equation from the first line of (1.1.5)

$$\phi' = \pm\sqrt{2U(\phi)} = \pm 2\sin\frac{\phi}{2}\,, \tag{1.1.7}$$

whose solutions also satisfy the sine-Gordon field equation (1.1.2). In this case, the Bogomolny equation can be integrated exactly to obtain

$$\phi(x) = 4\arctan\left(\exp\left(x - a\right)\right), \tag{1.1.8}$$

where a is a constant of integration describing the position of the kink. This solution has $\phi_+ = 2\pi$, so we see that this does indeed describe a single kink. Multi-kink solutions can be obtained via Bäcklund transformations [23], but these solutions are not static so cannot be obtained from the Bogomolny equation (there is, in fact, a repulsive force between kinks [24]).

The last key aspect of soliton theory we will introduce here is Derrick's Theorem [25].

This provides a non-existence theorem for topological solitons by considering spatial rescalings (for any number of dimensions) of the form $\boldsymbol{x} \to \Lambda \boldsymbol{x}$, $\Lambda > 0$. We denote the static energy after rescaling by $E(\Lambda)$. Derrick's Theorem then states that, if $E(\Lambda)$ has no stationary points (with respect to spatial rescalings) for non-vacuum finite energy field configurations, then the system can have no static, finite energy solutions to the field equations other than the vacuum. For the sine-Gordon model above we can write

$$E = \int_{-\infty}^{\infty} \left\{ \frac{1}{2}(\phi')^2 + (1 - \cos\phi) \right\} dx \equiv E_2 + E_0 \,, \tag{1.1.9}$$

where subscripts denote the order of the derivatives. We then have

$$E(\Lambda) = \Lambda^{-1} E_2 + \Lambda E_0 \,, \tag{1.1.10}$$

which is stationary when $\Lambda = \sqrt{E_2/E_0}$. We see that soliton solutions are not ruled out.

1.2 Solitons in 2-d: sigma model lumps and baby Skyrmions

One model that admits topological soliton-like solutions in 2 spatial dimensions is the $O(3)$ sigma model [26], described by a three-component unit vector field $\boldsymbol{\phi}(\boldsymbol{x})$ with the Lagrangian density

$$\mathcal{L} = -\frac{1}{2}\partial_\mu \boldsymbol{\phi} \cdot \partial^\mu \boldsymbol{\phi} - \frac{1}{2}\lambda(1 - \boldsymbol{\phi} \cdot \boldsymbol{\phi}) \,. \tag{1.2.1}$$

The Lagrange multiplier λ is dependent on the field and enforces the constraint $\boldsymbol{\phi} \cdot \boldsymbol{\phi} = 1$ as follows. By calculating the variation of (1.2.1) with respect to the field $\boldsymbol{\phi}$ we find

$$\begin{aligned} & \lambda \boldsymbol{\phi} = -\partial_\mu \left(\partial^\mu \boldsymbol{\phi} \right) \\ \Rightarrow \quad & \lambda \;\; = -\partial_\mu \left(\partial^\mu \boldsymbol{\phi} \right) \cdot \boldsymbol{\phi} \\ & \qquad = -\partial_\mu \left((\partial^\mu \boldsymbol{\phi}) \cdot \boldsymbol{\phi} \right) + \partial_\mu \boldsymbol{\phi} \cdot \partial^\mu \boldsymbol{\phi} \\ & \qquad = \partial_\mu \boldsymbol{\phi} \cdot \partial^\mu \boldsymbol{\phi} \,, \end{aligned} \tag{1.2.2}$$

where we have eliminated the first term in the penultimate line using the constraint. The associated field equation and static energy of this model are then given by

$$-\partial_\mu \partial^\mu \boldsymbol{\phi} - (\partial_\mu \boldsymbol{\phi} \cdot \partial^\mu \boldsymbol{\phi})\boldsymbol{\phi} = 0\,, \tag{1.2.3}$$

$$E = \frac{1}{2}\int \partial_i \boldsymbol{\phi} \cdot \partial_i \boldsymbol{\phi}\, d^2\boldsymbol{x}\,. \tag{1.2.4}$$

We use lower case Greek letters $\mu, \nu, \ldots$ to indicate spacetime indices $0, 1, 2$ and lower case Latin letters $i, j, \ldots$ to indicate purely spatial indices $1, 2$.

For finite energy field configurations we require the field $\boldsymbol{\phi}$ to tend to a constant vector at spatial infinity, which we can take to be $\boldsymbol{\phi}^\infty = (0, 0, 1)$ without loss of generality. This compactifies space to $\mathbb{R}^2 \cup \{\infty\} \cong S^2$, meaning that the field is a map $\boldsymbol{\phi} : S^2 \to S^2$. Such a field has an associated integer B, the topological degree of the map $\boldsymbol{\phi}$, arising from the homotopy group $\pi_2(S^2) = \mathbb{Z}$. This integer tells us how many times the domain wraps around the target space under the mapping. In 1-dimension this is called the winding number, and this terminology is sometimes also used for higher dimensional systems. In topological soliton theory, the topological degree of a soliton is also known as the topological charge.

The topological degree can be explicitly calculated as

$$B = \int \boldsymbol{\phi}^\star(\Omega)\,, \tag{1.2.5}$$

where $\boldsymbol{\phi}^\star(\Omega)$ is the pull-back of the normalised volume measure Ω on the target space. In the case of the $O(3)$ sigma model our target space is S^2 and the volume measure on this space (using spherical polar coordinates) is

$$\Omega = \frac{1}{4\pi}\sin\theta\, d\theta d\phi\,. \tag{1.2.6}$$

After the parametrisation $\boldsymbol{\phi}(\boldsymbol{x}) = (\cos\theta(\boldsymbol{x}), \sin\theta(\boldsymbol{x})\cos\phi(\boldsymbol{x}), \sin\theta(\boldsymbol{x})\sin\phi(\boldsymbol{x}))$ we can then calculate the pull-back:

$$\begin{aligned} \boldsymbol{\phi}^\star(\Omega) &= \frac{1}{4\pi}\sin\theta(\boldsymbol{x}) J(\boldsymbol{x})\, d^2\boldsymbol{x} \\ &= \frac{1}{4\pi}\boldsymbol{\phi}\cdot(\partial_1\boldsymbol{\phi}\times\partial_2\boldsymbol{\phi})\, d^2\boldsymbol{x} \end{aligned} \tag{1.2.7}$$

where $J(\boldsymbol{x}) = \partial_1\theta\partial_2\phi - \partial_2\theta\partial_1\phi$ is the Jacobian of the map at $\boldsymbol{x}$. Finally, this yields an

explicit expression for the topological charge:

$$B = \frac{1}{4\pi}\int \boldsymbol{\phi}\cdot(\partial_1\boldsymbol{\phi}\times\partial_2\boldsymbol{\phi})\,d^2\boldsymbol{x}\,. \tag{1.2.8}$$

The topological degree of a map is a very important concept in topological soliton theory, and can be calculated in a number of other ways. One such way is by counting pre-images: since the degree can be thought of as a generalised winding number, it is equivalent to counting the pre-images of points on the target space with multiplicity (see [27] for an detailed explanation of why the two definitions are equivalent).

As with kinks in 1-d, we can find a Bogomolny bound and Bogomolny equation for the $O(3)$ sigma model. By integrating the inequality

$$(\partial_i\boldsymbol{\phi}\pm\varepsilon_{ij}\boldsymbol{\phi}\times\partial_j\boldsymbol{\phi})\cdot(\partial_i\boldsymbol{\phi}\pm\varepsilon_{ik}\boldsymbol{\phi}\times\partial_k\boldsymbol{\phi})\geq 0\,, \tag{1.2.9}$$

we can find an inequality in terms of the static energy (1.2.4) and topological charge (1.2.8), yielding $E\geq 4\pi|B|$.

Exact solutions in this model for topological charge B can easily be found by re-writing the problem in terms of Riemann sphere coordinates

$$W(\zeta)=\frac{\phi_1+i\phi_2}{1-\phi_3}\,, \tag{1.2.10}$$

where we have introduced the complex coordinate $\zeta=x_1+ix_2$. The static energy and topological charge now take the form

$$E = 4\int\frac{|\partial_\zeta W|^2+|\partial_{\bar\zeta}W|^2}{(1+|W|^2)^2}\,d^2\boldsymbol{x}\,, \tag{1.2.11}$$

$$B = \frac{1}{\pi}\int\frac{|\partial_\zeta W|^2-|\partial_{\bar\zeta}W|^2}{(1+|W|^2)^2}\,d^2\boldsymbol{x}\,, \tag{1.2.12}$$

where $\partial_\zeta=\frac{1}{2}(\partial_1-i\partial_2)$ and $\partial_{\bar\zeta}=\frac{1}{2}(\partial_1+i\partial_2)$. Finite energy solutions satisfy $W\to\infty$ as $|\zeta|\to\infty$ (since $\boldsymbol{\phi}\to(0,0,1)$), and the Bogomolny bound for $B>0$ is saturated by fields satisfying $\partial_{\bar\zeta}W=0$ i.e. holomorphic functions of ζ. Recalling that the topological degree of a map can be obtained by counting pre-images, and demanding finite energy, gives soliton solutions as rational functions

$$W(\zeta)=\frac{p(\zeta)}{q(\zeta)}\,, \tag{1.2.13}$$

where $p(\zeta)$ and $q(\zeta)$ are polynomials which share no common factors. In addition, $p(\zeta)$ must be a polynomial of degree B and $q(\zeta)$ must have degree strictly less than B in order to preserve the condition $W \to \infty$ as $|\zeta| \to \infty$.

Strictly speaking, solutions of this form are not solitons since they exhibit an instability to spatial rescalings. This can be shown by looking to Derrick's Theorem. The static energy (1.2.4) is, in fact, invariant under spatial rescalings

$$E(\Lambda) = E_2 = E\,, \tag{1.2.14}$$

and so the solutions described above are sometimes instead called $O(3)$ sigma lumps (or instantons).

This problem can be circumvented by adding further terms to the Lagrangian. If a scalar potential and a term fourth-order in derivatives are added then we can write

$$E = E_2 + E_0 + E_4\,, \tag{1.2.15}$$

$$E(\Lambda) = E_2 + \Lambda^2 E_0 + \Lambda^{-2} E_4\,, \tag{1.2.16}$$

which now has stationary points with respect to spatial rescalings, and so true soliton solutions are not ruled out. One well-studied example of this form is the baby Skyrme model [28]

$$\mathcal{L} = -\frac{1}{2}\partial_\mu \boldsymbol{\phi}\cdot\partial^\mu\boldsymbol{\phi} - m^2(1-\boldsymbol{\phi}\cdot\boldsymbol{n}) - \frac{\kappa^2}{4}(\partial_\mu\boldsymbol{\phi}\times\partial_\nu\boldsymbol{\phi})\cdot(\partial^\mu\boldsymbol{\phi}\times\partial^\nu\boldsymbol{\phi}) \tag{1.2.17}$$

where m and κ are positive constant parameters, and $\boldsymbol{n}$ is a constant unit vector, usually set to $\boldsymbol{n} = (0,0,1)$. The topology is fixed by the winding number above, and we find the same Bogomolny bound $E \geq 4\pi|B|$. Further details of this model will be described in Chapter 2 where we discuss the baby Skyrme model (and another related model) in a curved spacetime as a low-dimensional analogue of holographic QCD. It should be noted that the baby Skyrme model does exhibit multi-soliton solutions, but none of these solutions (even for $B = 1$) saturate the Bogomolny bound.

Baby Skyrmions have been studied extensively as a low-dimensional analogue of Skyrmions [28], and also manifest themselves in condensed matter physics, such as in studies of the quantum Hall effect [29] and chiral ferromagnets [30].

1.3 Solitons in 3-d: Skyrmions

The Skyrme model [12, 13] in (3+1)-dimensions is written in terms of an $SU(2)$-valued field $U(x)$ and is given by the Lagrangian density

$$\mathcal{L} = \frac{1}{2}\mathrm{Tr}\left(R_\mu R^\mu\right) + \frac{1}{16}\mathrm{Tr}\left([R_\mu, R_\nu][R^\mu, R^\nu]\right) , \tag{1.3.1}$$

where $R_\mu = (\partial_\mu U)U^{-1}$. As before, finite energy configurations require the matrix U to tend to a constant matrix at spatial infinity, which we can take to be the identity matrix: $U \to 1_2$ as $|\boldsymbol{x}| \to \infty$. This compactifies space to $\mathbb{R}^3 \cup \{\infty\} \cong S^3$ and so we have a map $U : SU(2) \cong S^3 \to S^3$. Such maps have homotopy group $\pi_3(S^3) = \mathbb{Z}$ and there is an associated integer winding number

$$B = \frac{1}{24\pi^2}\int \varepsilon_{ijk}\mathrm{Tr}(R_i R_j R_k)\, d^3\boldsymbol{x}\,, \tag{1.3.2}$$

which provides the appropriate topological charge. The static energy of solutions within this model is given by

$$E = \int\left\{-\frac{1}{2}\mathrm{Tr}(R_i R_i) - \frac{1}{16}\mathrm{Tr}([R_i, R_j][R_i, R_j])\right\} d^3\boldsymbol{x}\,, \tag{1.3.3}$$

and there is an associated Bogomolny bound $E \geq 12\pi^2|B|$. The solitons of this model are called Skyrmions.

The Skyrme model has been suggested as a candidate low-energy effective field theory description of QCD in the large N_c limit, where N_c is the number of quark colours [31, 32, 33], with the Skyrme field taking values in $SU(N_f)$ for N_f quark flavours (here $N_f = 2$). The model is interpreted as a nonlinear theory of pions, and baryons arise as the Skyrmions of the system, with the baryon number being identified with the topological charge. This interpretation can be made more explicit by writing the field U as

$$U(x) = \sigma(x)1_2 + i\boldsymbol{\pi}(x)\cdot\boldsymbol{\tau}\,, \tag{1.3.4}$$

where $\boldsymbol{\tau}$ are the Pauli matrices, $\boldsymbol{\pi}(x)$ are the pion fields and $\sigma(x)$ is a scalar field determined by the constraint $\sigma^2 + \boldsymbol{\pi}\cdot\boldsymbol{\pi} = 1$ arising from $\det(U) = 1$.

The Skyrme model (with the addition of a pion mass term) has had many successes in

describing baryons qualitatively, managing to successfully predict the stability of the alpha particle [34] as well as the quantum numbers of excited states of light nuclei [35]. However, the Skyrme model does not accurately reproduce the physically observed binding energies of nuclei, typically predicting them to be an order of magnitude larger than observed [36, 37]. There have been many attempts to modify the Skyrme model in order to reduce the binding energies predicted [38, 39, 40, 41, 42], each with varying levels of success.

1.4 Solitons in 4-d: Yang-Mills instantons

The final class of solitons we will look at in this introduction are the Yang-Mills instantons [43] defined in 4-dimensional Euclidean spacetime. The fourth spatial dimension can be interpreted as a Wick rotation of the Minkowski time coordinate, from which we derive the name "instanton": they are localised around an "instant" of Euclidean time.

The model is formulated as an $SU(2)$ gauge theory with $\mathfrak{su}(2)$-valued gauge potential A_I and associated field strength tensor $F_{IJ} = \partial_I A_J - \partial_J A_I + [A_I, A_J]$, where upper case Latin letters $I, J, \ldots$ denote the four spatial indices $1, 2, 3, 4$. The Yang-Mills action is given by

$$S = -\frac{1}{2}\int \mathrm{Tr}(F_{IJ}F_{IJ})\, d^4x\,, \tag{1.4.1}$$

and the topological data is captured by the second Chern number

$$c_2 = N = -\frac{1}{16\pi^2}\int \mathrm{Tr}(F_{IJ} \star F_{IJ})\, d^4x \in \mathbb{Z}\,, \tag{1.4.2}$$

where we have defined the dual field strength

$$\star F_{IJ} = \frac{1}{2}\varepsilon_{IJKL}F_{KL}\,. \tag{1.4.3}$$

The inequality $-\mathrm{Tr}((F_{IJ} \pm \star F_{IJ})(F_{IJ} \pm \star F_{IJ})) \geq 0$ along with the fact that $\mathrm{Tr}(F_{IJ}F_{IJ}) = \mathrm{Tr}(\star F_{IJ} \star F_{IJ})$ yields the Bogomolny bound

$$S \geq 8\pi^2|N|\,, \tag{1.4.4}$$

and the bound is saturated by (anti-)self-dual fields satisfying

$$F_{IJ} = \pm \star F_{IJ} \,. \tag{1.4.5}$$

Under spatial rescalings we find that the action remains invariant; for this reason the $O(3)$ sigma lumps from Section 1.2 are sometimes considered to be a natural low-dimensional analogue of Yang-Mills instantons.

Many sophisticated techniques have been developed to study Yang-Mills instantons, most notably the ADHM construction [44] which generates N-instanton configurations from quaternionic matrices satisfying nonlinear algebraic constraints.

Yang-Mills instantons also have connections with lower-dimensional solitons, normally through dimensional reduction. One pertinent example relates Yang-Mills instantons with Skyrmions. In 1989, Atiyah and Manton showed that good approximations to static Skyrmion solutions could be obtained by computing the holonomy of a Yang-Mills instanton in $\mathbb{R}^4$, formally writing the static Skyrme field as a time-ordered exponential of the time-component of the Yang-Mills gauge field [45]. In fact, as explained in [46], Yang-Mills instanton holonomies give exact solutions to a related BPS Skyrme model. It is therefore possible to re-write the usual Yang-Mills instanton in terms of Skyrmion fields coupled to an infinite tower of vector mesons. The Skyrme fields and vector mesons were obtained by performing an eigenfunction expansion of the Yang-Mills gauge field in one direction, with the resulting model being called BPS because the solutions saturate the relevant Bogomolny bound (since the corresponding instantons also saturate the bound). The result of Atiyah and Manton can then be seen to be a first-order approximation to this procedure.

The construction described above bears some resemblance to the AdS/CFT correspondence, proposed by Maldacena [47]. This principle suggests a duality between string theories in anti-de Sitter spacetimes and conformal field theories on the boundaries of such spaces. Using this idea, many theories of so-called holographic QCD have been studied (for a review of modern string/gauge theory correspondence ideas in QCD see [48]).

1.5 The Sakai-Sugimoto model of holographic QCD

The leading theory of holographic QCD is the Sakai-Sugimoto model [1, 2]. The model has a five-dimensional effective description as a Yang-Mills-Chern-Simons theory in an AdS-like bulk, whose instantons correspond to Skyrmions (and therefore baryons) on the boundary. There is an identification between baryon number and instanton charge, so the study of baryons is equivalent to the study of Yang-Mills-Chern-Simons solitons in a curved space. The earlier results by Atiyah and Manton, subsequently explained by Sutcliffe, can then be seen as a flat-space analogue of the (effective) Sakai-Sugimoto model. Throughout this thesis, this effective model will also be referred to as the Sakai-Sugimoto model.

There has been interest in the connection between string theory and solitons for some time. Superstring theories admit objects called Dp-branes which extend in p spatial dimensions, and whose low-energy effective couplings are described by the Dirac-Born-Infeld (DBI) action [49]. The presence of Dp-branes is vital in superstring theory for spontaneously breaking some of the supersymmetries: in fact, Dp-branes break exactly half of the supersymmetries of superstring theory and are called BPS states [22]. A connection with soliton theory arises when we consider coincident D4-branes. In this case the DBI action takes the form of a Chern-Simons term, which can be re-expressed in terms of the second Chern number. This we recognise as the topological charge of Yang-Mills instantons (1.4.2), and in this way the study of Yang-Mills instantons is related to the study of BPS states in superstring theory.

In this thesis we will study the Sakai-Sugimoto model at zero temperature. The model consists of N_c colour $D4$-branes wrapped on an S^1, with antiperiodic boundary conditions. The background metric is given by

$$ds^2 = \left(\frac{U}{R}\right)^{3/2}\left(\eta_{\mu\nu}dx^\mu dx^\nu + f(U)d\tau^2\right) + \left(\frac{R}{U}\right)^{3/2}\left(\frac{dU^2}{f(U)} + U^2 d\Omega_4^2\right), \tag{1.5.1}$$

$$f(U) = 1 - \left(\frac{U_{KK}}{U}\right)^3, \tag{1.5.2}$$

where U_{KK} and R are constant parameters, the latter being related to the string length and string coupling. The $D4$-branes extend in the x^μ and τ directions. The $d\Omega_4^2$ is the line element of a unit S^4, and the holographic coordinate U is bounded below by the

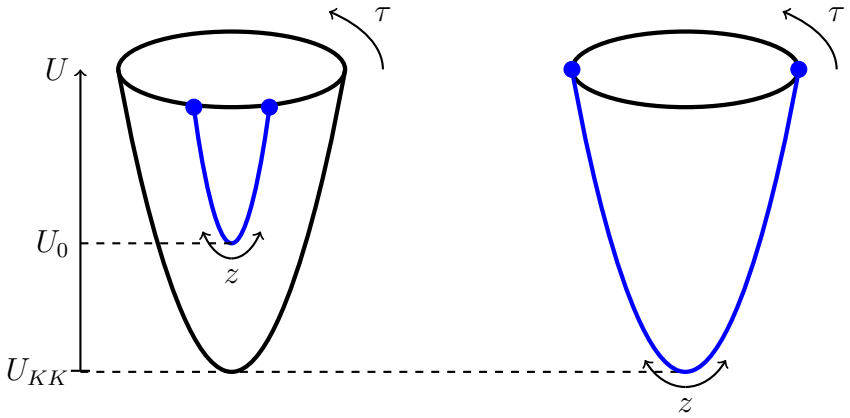

Figure 1.1: A sketch of the background geometry in the Sakai-Sugimoto model. There is a holographic radial direction U with horizon U_{KK}, and the τ direction must be periodic to avoid a conical singularity at the horizon. At $U = U_{KK}$ the radius of the τ-circle shrinks to zero, so the geometry is cigar-shaped. The blue curve represents a probe $D8/\overline{D8}$-brane pair. The coordinate z is a coordinate along the $D8/\overline{D8}$-brane pair with $z = 0$ at the point where they merge, corresponding to $U = U_0$. The left image shows the $D8/\overline{D8}$-brane in general, and the right image shows the $D8/\overline{D8}$-brane for antipodal separation.

condition $U \geq U_{KK}$. In order to avoid a conical singularity at $U = U_{KK}$, the coordinate τ must be periodic $\left(\text{with period } \frac{4\pi}{3}\sqrt{R^3/U_{KK}}\right)$, which is a crucial ingredient of the model. Importantly, the radius of this τ-circle shrinks as U decreases, vanishing at the horizon $U = U_{KK}$. This results in a cigar-shaped geometry (see Fig 1.1). In the low-energy limit this metric reproduces pure 4-dimensional Yang-Mills theory.

To add quark degrees of freedom we embed N_f flavour $D8/\overline{D8}$-branes, which extend in all but the compactified τ direction. We assume $N_f \ll N_c$ (i.e. we work in the large N_c limit) and treat the $D8/\overline{D8}$-branes as probes. Since the holographic coordinate U is bounded below, the $D8/\overline{D8}$-brane pairs are forced to merge at some critical point $U = U_0$. This is one of the chief successes of the Sakai-Sugimoto model: this merging breaks the $U(N_f)_L \times U(N_f)_R$ chiral symmetry of the $D8$-branes to a single $U(N_f)$ symmetry group, and this is interpreted as a holographic realisation of spontaneous chiral symmetry breaking.

We shall now restrict to $N_f = 2$ and the case $U_0 = U_{KK}$, which corresponds to the $D8/\overline{D8}$-branes having antipodal separation on the τ-circle (see right image of Fig 1.1). The low-energy effective theory can then be formulated in a curved "AdS-like"

spacetime given by the metric

$$ds^2 = H(z)dx_\mu dx^\mu + \frac{1}{H(z)}dz^2\,. \tag{1.5.3}$$

The coordinate z is related to the holographic direction U, with $z = 0$ corresponding to the point $U = U_0$ where the $D8/\overline{D8}$-branes merge. The warp factor $H(z)$ is given by

$$H(z) = \left(1 + \frac{z^2}{L^2}\right)^{2/3}\,, \tag{1.5.4}$$

and the length scale L can be set equal to 1 by a choice of units.

We say the spacetime is "AdS-like" since it possesses a conformal boundary and finite negative scalar curvature everywhere. The conformal boundary can explicitly be seen by transforming to conformal coordinates

$$ds^2 = H(z(u))\left(dx_\mu dx^\mu + du^2\right)\,, \tag{1.5.5}$$

where the new coordinate u solves $du/dz = 1/H(z)$. For large z we see the asymptotic behaviour of u is $u \sim c_1 + c_2/z^{1/3}$ i.e. $u \to c_1$ as $z \to \infty$. We can also explicitly calculate the Ricci curvature of the spacetime as

$$R = -\frac{16\,(3 + 4z^2)}{9\,(1 + z^2)^{4/3}}\,, \tag{1.5.6}$$

and we see that the result is finite and negative everywhere.

The DBI action of the $D8$-branes, after Kaluza-Klein reduction on the unit S^4, can be expressed in terms of a five-dimensional $U(2)$ gauge field $\mathcal{A}_\Gamma$ and field strength tensor $\mathcal{F}_{\Gamma\Delta} = \partial_\Gamma \mathcal{A}_\Delta - \partial_\Delta \mathcal{A}_\Gamma + i[\mathcal{A}_\Gamma, \mathcal{A}_\Delta]$, where we note that we are using conventions such that the gauge fields are hermitian. Upper case Greek letters $\Gamma, \Delta, \ldots$ denote all five spacetime indices in the low-energy description.

The effective action is given by

$$S = -\frac{1}{2}\int \sqrt{-\mathrm{g}}\left\{\mathrm{Tr}\left(\mathcal{F}_{\Gamma\Delta}\mathcal{F}^{\Gamma\Delta}\right)\right\}\, d^4x dz - \frac{\pi}{9\lambda}\int \omega_5(\mathcal{A}_\Gamma)\, d^4x dz\,, \tag{1.5.7}$$

where λ is the 't Hooft coupling. The first term is simply that of a Yang-Mills theory, and the second term is the five-dimensional Chern-Simons term. Here we see the two key elements of the Sakai-Sugimoto model: the first term gives us the standard

Yang-Mills action (in curved space), and the second term is the five-dimensional Chern-Simons term.

We can decompose the fields into $SU(2)$ and abelian parts (the latter denoted with a hat) as $\mathcal{A}_\Gamma = A_\Gamma + \frac{1}{2}\hat{A}_\Gamma$ and $\mathcal{F}_{\Gamma\Delta} = F_{\Gamma\Delta} + \frac{1}{2}\hat{F}_{\Gamma\Delta}$. This allows us to write the action up to total derivatives as:

$$\begin{aligned} S = -\frac{1}{2}\int H^{3/2}\left\{\frac{1}{2}\hat{F}_{\mu\nu}\hat{F}^{\mu\nu} + \hat{F}_{\mu z}\hat{F}^{\mu z} + \mathrm{Tr}\left(F_{\mu\nu}F^{\mu\nu}\right) + 2\mathrm{Tr}\left(F_{\mu z}F^{\mu z}\right)\right\} d^4x dz \\ + \frac{1}{\Lambda}\int \varepsilon^{\Gamma\Delta\Sigma\Xi\Upsilon}\left\{\hat{A}_\Gamma \mathrm{Tr}\left(F_{\Delta\Sigma}F_{\Xi\Upsilon}\right) + \frac{1}{6}\hat{A}_\Gamma\hat{F}_{\Delta\Sigma}\hat{F}_{\Xi\Upsilon}\right\} d^4x dz\,, \end{aligned} \tag{1.5.8}$$

where we have introduced the rescaled 't Hooft coupling $\Lambda = 8\lambda/27\pi$.

The appropriate static ansatz for soliton solutions in this model is

$$A_0 = \hat{A}_I = 0\,, \quad A_I = A_I(x_J)\,, \quad \hat{A}_0 = \hat{A}_0(x_J)\,, \tag{1.5.9}$$

so that the abelian gauge potential sources an electric field $\hat{F}_{I0} = \partial_I \hat{A}_0$. The static energy can then be written as:

$$\begin{aligned} E = \frac{1}{2}\int\Bigg\{ &-\frac{1}{H^{1/2}}\left(\partial_i\hat{A}_0\right)^2 - H^{3/2}\left(\partial_z\hat{A}_0\right)^2 \\ &+ \frac{1}{H^{1/2}}\mathrm{Tr}\left(F_{ij}F_{ij}\right) + 2H^{3/2}\mathrm{Tr}\left(F_{iz}F_{iz}\right) \\ &+ \frac{8}{\Lambda}\hat{A}_0\varepsilon_{ijk}\mathrm{Tr}\left(F_{iz}F_{jk}\right)\Bigg\} d^3\boldsymbol{x}dz\,. \end{aligned} \tag{1.5.10}$$

By integrating by parts and using the equation of motion for $\hat{A}_0$ we can show that

$$E \geq 8\pi^2|N|\,, \tag{1.5.11}$$

where

$$\begin{aligned} N &= -\frac{1}{32\pi^2}\int \varepsilon^{IJKL}\mathrm{Tr}\left(F_{IJ}F_{KL}\right)\, d^3\boldsymbol{x}dz \\ &= \frac{1}{8\pi^2}\int \varepsilon_{ijk}\mathrm{Tr}\left(F_{iz}F_{jk}\right)\, d^3\boldsymbol{x}dz \end{aligned} \tag{1.5.12}$$

is the instanton number of the configuration.

We see that the Chern-Simons term takes the form of a coupling between an abelian $U(1)$ field $\hat{A}_0$ and the instanton number density of the configuration (the integrand of (1.5.12)).

Solitons and multi-solitons are guaranteed in this model by considering scaling behaviours and long-range soliton interactions. Single solitons of finite size are guaranteed by considering the energy (1.5.10) applied to a flat-space Yang-Mills instanton of finite size, as analysed in [50]. Here it was shown that the metric factors induce the soliton size to shrink, but that this is stabilised by the Chern-Simons term (the final term in (1.5.10)). Multi-solitons in the model are guaranteed by considering the interaction potential between two solitons, calculated in [51] using a linear approximation to the soliton tails. Here it was found that the first line of (1.5.10) induces a monopole interaction leading to short-range repulsion, while the second line of (1.5.10) induces a dipole interaction leading to long-range attraction.

Due to the large dimensionality of the Sakai-Sugimoto model, studying bulk soliton solutions either analytically or numerically is difficult. Progress has been made by observing that, in the limit where the bulk soliton size becomes small compared to the curvature of the spacetime, the single Sakai-Sugimoto soliton can be well approximated by a flat space, self-dual Yang-Mills instanton with a small size [52, 53]. This approximation was verified by numerical field theory calculations [50], where symmetry arguments could be applied to reduce the full four-dimensional computation to a two-dimensional problem. Unfortunately, such symmetries cannot be exploited when analysing multi-soliton solutions, and full four-dimensional computations are beyond current computational capabilities.

1.6 Cold, dense QCD: salt and popcorn

The QCD phase diagram – describing the states quarks and gluons occupy as a function of temperature and chemical potential – is a complicated thing to study (see [54] for a review). Detailed analysis has only been possible for very high temperatures and chemical potentials (due to the strongly coupled nature of the theory), and numerical progress (primarily by lattice methods) has been restricted to zero chemical potential due to the "sign problem".

Figure 1.2 shows a sketch of the main features currently understood to exist in the phase diagram of QCD. In the bottom-left corner of the diagram (low T and low μ) quarks

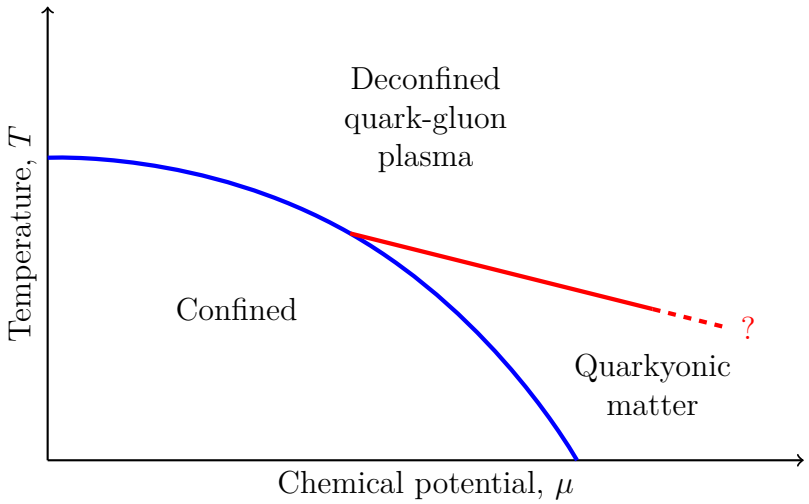

Figure 1.2: A sketch of the key features of the QCD phase diagram, as a function of temperature T and chemical potential μ. Pictured are the low-T, low-μ confined phase; the high-T quark-gluon plasma; and the proposed low-T, intermediate-μ quarkyonic phase.

and gluons are confined, forcing them to form colour-neutral states (primarily pions). Chiral symmetry in this state is spontaneously broken. From here, as temperature increases a phase transition is expected to occur in which quarks and gluons deconfine and chiral symmetry is restored. In this state, known as the quark-gluon plasma, quarks and gluons are asymptotically free. Moving from the bottom-left of the diagram along the chemical potential axis, a transition to nuclear matter is expected in which quarks condense into baryons. Beyond this, a number of exotic high-density behaviours have been suggested, including the formation of colour-superconductor states [55].

A new phase of the QCD phase diagram was proposed in [56], called quarkyonic matter. This state is predicted for low temperatures and intermediate chemical potentials, and would be relevant in the physics of neutron stars. In this phase the quarks exist in a confined state, forming a Fermi sea with a baryonic Fermi surface. Whether chiral symmetry in this state is broken or restored is currently unknown.

The Sakai-Sugimoto model already captures some of the above features of the QCD phase diagram. We have already seen how the geometry at zero temperature gives rise to a confined geometry with broken chiral symmetry. As temperature increases a competing geometry becomes energetically favourable: the AdS black hole. This geometry is cylindrical and obtained by swapping the roles of the compactified τ-

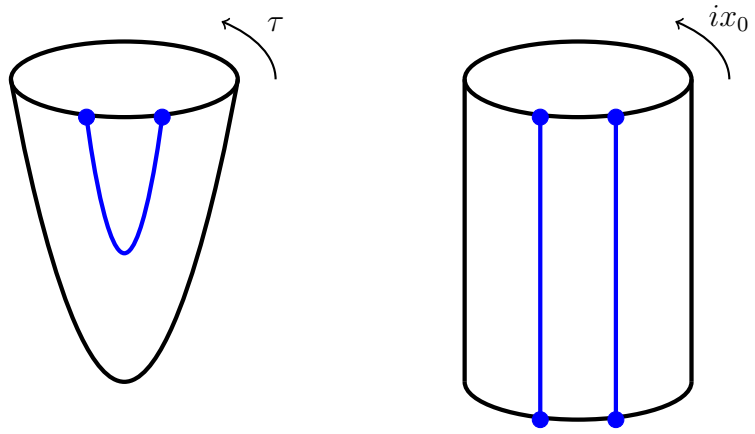

Figure 1.3: A sketch of the cigar-shaped Sakai-Sugimoto geometry at low temperatures (left), forcing spontaneous chiral symmetry breaking, and the cylindrical black hole geometry at high temperatures (right) in which chiral symmetry can be restored.

circle with the thermal circle (see Figure 1.3). The cylindrical geometry is interpreted as a deconfined geometry, and allows for $D8$-brane pairs to have endpoints on the horizon, leading to chiral symmetry restoration. Furthermore, recent advances in the application of holographic techniques [57, 58] have led to the suggestion that the cold, dense quarkyonic state may manifest as the formation of a four-dimensional structure in the holographic bulk. The details of how the bulk Sakai-Sugimoto solitons explore the holographic direction, however, are unknown.

There are two competing theories of how this happens in the Sakai-Sugimoto model. The first is the dyon salt model [3] in which the appropriate crystal is a salt-like arrangement of dyons, transforming in the high density limit into a cubic crystal of half-instantons. This is dual to the well-known Skyrme crystal [59, 60]. The dyon salt phenomenon is analogous to the splitting of periodic Yang-Mills instantons (calorons) into monopole constituents at high densities [61].

An alternate proposal is the baryonic popcorn model [4, 5] which states that, with increasing density, a series of phase transitions will occur where a three-dimensional soliton crystal develops extra layers in the holographic direction. Such transitions have been dubbed popcorn transitions. Unfortunately analytical or numerical investigation of these phenomena has proved difficult.

1.7 Outline

This thesis will attempt to gain insight into the features of the Sakai-Sugimoto model and its high-density phase transitions by studying various low-dimensional analogues and approximations.

In Chapter 2 we investigate a low-dimensional toy model based on $O(3)$ sigma instantons. We stabilise the model with the introduction of a vector meson term. Solitons, multi-solitons and finite-density soliton chains are numerically computed, and analogues of baryonic popcorn and dyon salt are both found. The baryonic popcorn configuration is found to be energetically favourable.

Chapter 3 provides an investigation of baby Skyrmions in pure AdS spacetime. Full numerical calculations are performed and a point-particle model is developed. Analogues of baryonic popcorn transitions are found, in which the solutions form concentric rings and develop extra layers.

In Chapter 4 we apply a homogeneous ansatz to a holographic baby Skyrme model [62] to approximate high-density configurations. A set of popcorn transitions are numerically computed, although such configurations are forced to lie in a dyon salt regime. The approximation is found to qualitatively match with full numerical results.

Finally, Chapter 5 applies two different homogeneous ansätze to the full Sakai-Sugimoto model, reducing the model to an effective one-dimensional kink theory. Analogues of both dyon salt and baryonic popcorn are discovered. A new, energetically favourable high-density phase is also found in the form of a soliton bag.

Chapter 2

A low-dimensional analogue of holographic QCD with vector mesons

2.1 Introduction

To try to gain some further insight into the behaviour of the Sakai-Sugimoto solitons, a low-dimensional analogue of the model was recently studied [62]. Since instantons of $O(3)$ sigma models in two space dimensions are well known natural analogues of Yang-Mills instantons in four space dimensions, an $O(3)$ sigma model was studied, coupled to a baby Skyrme term in order to stabilise the solitons against the shrinking due to the curvature of space (a role played by the Chern-Simons term in the full Sakai-Sugimoto model). The advantage of the low-dimensional theory is that numerical computations become more viable, and both isolated soliton solutions and finite-density configurations were found. It was found that the dyon salt phase was not energetically favourable, and that beyond a critical density the system undergoes a first-order popcorn transition (albeit one qualitatively different to that predicted in [4, 5]) in which a single chain of solitons splits suddenly into two aligned chains separated in the holographic direction. At even higher densities another popcorn transition was found where the double-chain splits into a triple-chain, and it was conjectured that this procedure would continue so that at higher densities the

configuration begins to resemble a portion of a two-dimensional crystal. It was also shown that these chain solutions could be well approximated by periodic chains of flat-space instantons.

However, an alternative low-dimensional analogue of the Sakai-Sugimoto model can be obtained by replacing the baby Skyrme term with a vector meson term in which a new vector field couples to the topological current of the $O(3)$ sigma fields. This would be a closer analogue to the full Sakai-Sugimoto model with the vector field playing the role of the $U(1)$ gauge field that couples to the topological current through the Chern-Simons term (the final term in (1.5.10)). Such a model was studied in flat space in [63], and found to be closely related to the baby Skyrme model. In this chapter we will study the effect of replacing the baby Skyrme term with a vector meson term in a curved background, and see how the isolated solitons and popcorn transitions of finite-density configurations are affected. In addition, since full numerical field simulations are viable in two dimensions, we will use the low-dimensional vector meson model as a testing ground to check the validity of some common approximations used when studying the full Sakai-Sugimoto model.

This chapter is based on my own work published in [6].

2.2 The holographic baby Skyrme and vector meson models

We consider a $(D+2)$-dimensional spacetime with a warped metric

$$ds^2 = H(z)(-dt^2 + dx_1^2 + ... + dx_D^2) + \frac{1}{H(z)}dz^2 \tag{2.2.1}$$

with

$$H(z) = \left(1 + \frac{z^2}{L^2}\right)^p . \tag{2.2.2}$$

The warp factor, $H(z)$ depends only on the holographic coordinate z, and L determines some curvature length scale which we will set to unity. We will choose the constant p shortly. The effective metric of the Sakai-Sugimoto model is recovered by choosing

$D = 3$ and $p = \frac{2}{3}$, which ensures that the spacetime has a conformal boundary as $z \to \infty$, and that the scalar curvature is negative and finite everywhere.

Following [62], we investigate a low-dimensional toy model of the Sakai-Sugimoto model with $D = 1$. We choose the constant p to ensure that the scalar curvature of the metric is finite and negative. The appropriate Ricci scalar is given by

$$R = -2p\left(1+z^2\right)^{p-2}\left(2+(5p-2)z^2\right) \tag{2.2.3}$$

and so finite, negative scalar curvature everywhere demands $\frac{2}{5} \leq p \leq 1$. Furthermore, we can obtain another restriction on p by demanding that the flat-space instanton approximation to the soliton solutions in this model have finite energy. This adds the further restriction $p < \frac{2}{3}$, which we will justify in Section 2.3 when we introduce the flat-space ansatz for radial soliton fields. It is therefore convenient to make the choice $p = \frac{1}{2}$.

In [62] solitons in the baby Skyrme model in this spacetime were studied. The action for this baby Skyrme (BS) model is

$$S_{BS} = \int \left(-\frac{1}{2}\partial_\mu \boldsymbol{\phi}\cdot\partial^\mu\boldsymbol{\phi} - \frac{\kappa^2}{4}(\partial_\mu\boldsymbol{\phi}\times\partial_\nu\boldsymbol{\phi})\cdot(\partial^\mu\boldsymbol{\phi}\times\partial^\nu\boldsymbol{\phi})\right)\sqrt{H}\,dxdzdt \tag{2.2.4}$$

where the first term is that of the $O(3)$ sigma model, and the second term is the baby Skyrme term with constant coefficient κ^2. Greek indices run over the bulk spactime coordinates t, x and z. The field $\boldsymbol{\phi} = (\phi_1, \phi_2, \phi_3)$ is a three component unit vector. We will refer to $\boldsymbol{\phi}$ as the pion field since the baby Skyrme model can be seen as a 2-dimensional analogue of the Skyrme model where the corresponding $\boldsymbol{\phi}$ field plays the role of pions. The associated static energy of this model is

$$E_{BS} = \frac{1}{2}\int\left(\frac{1}{\sqrt{H}}|\partial_x\boldsymbol{\phi}|^2 + H\sqrt{H}|\partial_z\boldsymbol{\phi}|^2 + \kappa^2\sqrt{H}|\partial_x\boldsymbol{\phi}\times\partial_z\boldsymbol{\phi}|^2\right)dxdz\,. \tag{2.2.5}$$

Here we will instead investigate solitons of an $O(3)$ sigma model coupled to a massive vector meson. The action for this vector meson (VM) model is given by

$$S_{VM} = \int\Bigg(-\frac{1}{2}\partial_\mu\boldsymbol{\phi}\cdot\partial^\mu\boldsymbol{\phi} - \frac{1}{4}(\partial_\mu\omega_\nu - \partial_\nu\omega_\mu)(\partial^\mu\omega^\nu - \partial^\nu\omega^\mu) - \frac{1}{2}M^2\omega_\mu\omega^\mu + g\omega_\mu B^\mu\Bigg)\sqrt{H}\,dxdzdt \tag{2.2.6}$$

where the pion field $\boldsymbol{\phi} = (\phi_1, \phi_2, \phi_3)$ is again a three component unit vector and ω_μ is a spacetime vector field with mass M. The fourth term, parametrised by the constant g, is a coupling between the ω_μ field and the topological current

$$B^\mu = -\frac{1}{8\pi\sqrt{H}}\varepsilon^{\mu\alpha\beta}\boldsymbol{\phi}\cdot(\partial_\alpha\boldsymbol{\phi}\times\partial_\beta\boldsymbol{\phi})\,. \tag{2.2.7}$$

We argue that this model is a low-dimensional analogue of the Sakai-Sugimoto model as follows. The full five-dimensional model is written in terms of a $U(2)$ gauge field which can be decomposed into an abelian $U(1)$ and an $SU(2)$ field. Written in this way, the Chern-Simons term is a coupling between the $U(1)$ field and the topological current associated with the $SU(2)$ field (see the final term of (1.5.10)). Noting that both pure $SU(2)$ theory in $(4+1)$ dimensions and the $O(3)$ sigma model in $(2+1)$ dimensions are both scale invariant, we can take $\boldsymbol{\phi}$ and ω_μ to be the low-dimensional analogues of the $SU(2)$ and $U(1)$ fields respectively. With this correspondence we see that the fourth term in (2.2.6) is a low-dimensional analogue of the Chern-Simons term.

In this chapter we will be concerned with static soliton solutions in this model. Looking at (2.2.7) it is easy to see that for static solutions the spatial components of the topological current vanish ($B^x = B^z = 0$). These currents provide a source for ω_μ, so we see that $\omega_x = \omega_z = 0$ for static solutions. For notational convenience we will write $\omega \equiv \omega_0$ for the remainder of this chapter. We will refer to ω as the vector meson field.

The associated static energy of this model is

$$E_{VM} = E_{\boldsymbol{\phi}} + E_\omega \tag{2.2.8}$$

with

$$E_{\boldsymbol{\phi}} = \frac{1}{2}\int\left\{\frac{1}{\sqrt{H}}|\partial_x\boldsymbol{\phi}|^2 + H\sqrt{H}|\partial_z\boldsymbol{\phi}|^2\right\}dxdz \tag{2.2.9}$$

$$E_\omega = \frac{1}{2}\int\left\{-\frac{1}{H\sqrt{H}}(\partial_x\omega)^2 - \sqrt{H}(\partial_z\omega)^2 - \frac{M^2\omega^2}{\sqrt{H}} + \frac{g\omega}{2\pi}\boldsymbol{\phi}\cdot(\partial_x\boldsymbol{\phi}\times\partial_z\boldsymbol{\phi})\right\}dxdz\,. \tag{2.2.10}$$

For finite energy we then require $\boldsymbol{\phi}\to(0,0,1)$ and $\omega\to 0$ as $x^2+z^2\to\infty$. This allows us to compactify space from $\mathbb{R}^2$ to S^2, meaning the pion field is now a map $\boldsymbol{\phi}: S^2\to S^2$

with an associated winding number and topological charge

$$B = \int B^0 \sqrt{H}\, dxdz = -\frac{1}{4\pi} \int \boldsymbol{\phi} \cdot (\partial_x \boldsymbol{\phi} \times \partial_z \boldsymbol{\phi})\, dxdz\,, \tag{2.2.11}$$

which defines the instanton number of the planar $O(3)$ sigma model. This topological charge we identify with the baryon number of the configuration.

By calculating the variation of the action (2.2.6) with respect to the vector meson field we obtain the Euler-Lagrange equation

$$\left(\frac{1}{H\sqrt{H}}\partial_{xx} + \sqrt{H}\partial_{zz} + \frac{1}{2}\frac{H'}{\sqrt{H}}\partial_z - \frac{1}{\sqrt{H}}M^2\right)\omega + \frac{g}{4\pi}\boldsymbol{\phi} \cdot (\partial_x \boldsymbol{\phi} \times \partial_z \boldsymbol{\phi}) = 0\,. \tag{2.2.12}$$

Multiplying this equation by ω and integrating by parts in (2.2.10) allows us to write

$$E_\omega = \frac{1}{2} \int \frac{g}{4\pi}\omega \boldsymbol{\phi} \cdot (\partial_x \boldsymbol{\phi} \times \partial_z \boldsymbol{\phi})\, dxdz \tag{2.2.13}$$

$$= \frac{1}{2} \int \left(\frac{1}{H\sqrt{H}}(\partial_x \omega)^2 + \sqrt{H}(\partial_z \omega)^2 + \frac{M^2\omega^2}{\sqrt{H}}\right) dxdz\,. \tag{2.2.14}$$

We then see that $E_\omega \geq 0$ whenever the equation of motion for ω is satisfied and this, together with the inequality

$$\left|\frac{1}{\sqrt{H}}\partial_x \boldsymbol{\phi} \pm \sqrt{H}\boldsymbol{\phi} \times \partial_z \boldsymbol{\phi}\right|^2 \geq 0\,, \tag{2.2.15}$$

yields the Bogomolny bound $E_{VM} \geq 4\pi|B|$. Note that we require ω to satisfy its equation of motion in order to obtain the Bogomolny bound, which is unusual in soliton theory. Without this requirement the energy (2.2.10) is, in fact, unbounded below which could in principle lead to problems when applying gradient flow algorithms later to numerically find soliton solutions. However, we have found that these problems can be avoided by careful choices of initial conditions and gradient flow parameters.

By approximating the solution to (2.2.12) using a leading-order derivative expansion, we can see how the BS and VM models are related [63]. Neglecting derivatives of ω in (2.2.12) yields the approximation

$$\omega \approx \frac{g\sqrt{H}}{4\pi M^2}\boldsymbol{\phi} \cdot (\partial_x \boldsymbol{\phi} \times \partial_z \boldsymbol{\phi}) \tag{2.2.16}$$

which can be substituted into (2.2.13) to obtain

$$E_\omega = \frac{1}{2} \int \frac{g^2\sqrt{H}}{16\pi^2 M^2}|\partial_x \boldsymbol{\phi} \times \partial_z \boldsymbol{\phi}|^2\, dxdz \tag{2.2.17}$$

$$\Rightarrow \quad E_{VM} = \frac{1}{2}\int \left(\frac{1}{\sqrt{H}}|\partial_x \boldsymbol{\phi}|^2 + H\sqrt{H}|\partial_z \boldsymbol{\phi}|^2 + \frac{g^2\sqrt{H}}{16\pi^2 M^2}|\partial_x \boldsymbol{\phi} \times \partial_z \boldsymbol{\phi}|^2 \right) dxdz\,. \quad (2.2.18)$$

This is precisely the static energy of the BS model (2.2.5) upon identifying

$$\kappa = \frac{g}{4\pi M}\,. \quad (2.2.19)$$

Note that the approximation used above becomes more accurate as M and g increase i.e. as the vector meson field becomes infinitely massive and its interaction becomes point-like. We recover the exact BS model in the limit

$$M, g \to \infty\,, \qquad \kappa = \frac{g}{4\pi M} = \text{constant}\,. \quad (2.2.20)$$

We will justify this approximation and discuss its validity in the following section.

2.3 Solitons in the vector meson model

In flat space ($H = 1$) and in the absence of a vector meson ($\omega_\mu \equiv 0$) the Bogomolny bound (2.2.15) is saturated by the scale-invariant instanton solutions of the $O(3)$ sigma model. Using Riemann sphere coordinates $W = (\phi_1 + i\phi_2)/(1 - \phi_3)$, obtained by stereographic projection of the pion field $\boldsymbol{\phi}$, and recalling the discussion in Section 1.2, the radially symmetric sigma-model instanton with topological charge B centred at the origin can be written as $W = (\zeta/\mu)^B$ where μ is a positive real constant which determines the arbitrary scale of the instanton. The associated pion field for this solution is given by

$$\boldsymbol{\phi} = (\sin f \cos(B\theta), \sin f \sin(B\theta), \cos f) \quad (2.3.1)$$

where (r, θ) are polar coordinates in the (x, z)-plane and $f(r)$ is the radial profile function

$$f(r) = \cos^{-1}\left(\frac{r^{2B} - \mu^{2B}}{r^{2B} + \mu^{2B}} \right)\,. \quad (2.3.2)$$

Now we can justify the restriction $p < 2/3$ imposed on the spacetime metric from demanding this radial solution to have finite energy. For large r the profile function

behaves as

$$f(r) \sim \frac{2\mu^B}{r^B}\,, \tag{2.3.3}$$

and so we see the solution with $B = 1$ has the slowest decay, and therefore will provide the greatest restriction on p. Substituting this into (2.2.9), the leading-order contribution to the energy at large r is given by

$$\begin{aligned} E_{\boldsymbol{\phi}} &= \frac{1}{2}\int \left\{ H\sqrt{H}|\partial_z \boldsymbol{\phi}|^2 + \cdots \right\} dxdz \\ &= \int \left\{ 2\mu^2 \sin^{3p}\theta\, r^{3p-4} + \cdots \right\} rdrd\theta \\ &= \int \left\{ 2\mu^2 C r^{3(p-1)} + \cdots \right\} dr \end{aligned} \tag{2.3.4}$$

where C is a constant arising from the angular integral. To ensure this leads to a finite energy we therefore require $3(p-1) < -1 \Rightarrow p < 2/3$, as stated before.

In the Sakai-Sugimoto model the 't Hooft coupling is taken to be large, which results in a small size for the Sakai-Sugimoto soliton compared to the length scale set by the curvature of spacetime. The analogous regime in the BS model is to take κ small and positive, and it was shown that in this regime the soliton can be well approximated by a sigma model instanton. These instantons have an arbitrary size in flat space, but a preferred size can be obtained by considering the leading-order contributions to the energy from the spacetime curvature and the baby Skyrme term interaction. Here we shall search for some parameter regime in (g, M)-space in the VM model analogous to this situation, and demonstrate that this regime is consistent with the approximations discussed above, and with the established relation between the VM and BS models.

Taking a flat-space ($H = 1$) radial ansatz for the vector meson field, and a flat-space sigma instanton ansatz (2.3.1) for the pion field, we first find a parameter regime in which the approximation (2.2.16) is valid. With these assumptions, the equation of motion (2.2.12) for ω becomes

$$\frac{1}{r}\partial_r(r\partial_r\omega) = M^2\omega + \frac{gB^2\mu^{2B}}{\pi}\frac{r^{2B-2}}{(r^{2B}+\mu^{2B})^2} \tag{2.3.5}$$

where B is the topological charge of the solution and μ is the size of the sigma instanton.

Assuming that $|\frac{1}{r}\partial_r(r\partial_r\omega)| \ll |M^2\omega|$ yields the approximation

$$\omega \approx \frac{-gB^2\mu^{2B}}{M^2\pi}\frac{r^{2B-2}}{(r^{2B}+\mu^{2B})^2}\,. \tag{2.3.6}$$

We then find

$$\left|M^2\omega\right| = \frac{gB^2\mu^{2B}}{\pi}\frac{r^{2B-2}}{(r^{2B}+\mu^{2B})^2}\,, \tag{2.3.7}$$

$$\left|\frac{1}{r}\partial_r(r\partial_r\omega)\right| = \frac{4gB^2\mu^{2B}}{M^2\pi}\frac{r^{2B-4}}{(r^{2B}+\mu^{2B})^4}\Gamma\,, \tag{2.3.8}$$

where $\Gamma = \left|(B+1)^2r^{4B} - 2(2B^2-1)\mu^{2B}r^{2B} + (B-1)^2\mu^{4B}\right|$. Therefore the inequality above is consistent if

$$\frac{4}{M^2(r^{2B}+\mu^{2B})^2}\left|(B+1)^2r^{4B-2} - 2(2B^2-1)\mu^{2B}r^{2B-2} + (B-1)^2\frac{\mu^{4B}}{r^2}\right| \ll 1\,, \tag{2.3.9}$$

For $B = 1$ the approximation (2.3.6) has a local minimum at the origin, and evaluating the above expression there yields the condition

$$M \gg \frac{2\sqrt{2}}{\mu}\,. \tag{2.3.10}$$

For other topological charges we can find a similar condition by evaluating the above expression at the extrema of the radial ansatz. We have therefore found that if we seek a regime in which the soliton size is small compared to the curvature scale, and in which derivatives of ω are small, we require a large mass for the vector meson field.

We will now insert this approximation into the curved space static energy and look at the terms coming from the first-order expansion of the warp factor, $H(z)$. We shall also re-insert the explicit dependence of H on p (as in (2.2.2)) so that we can clearly see which terms arise from the curvature of spacetime and which terms arise from interactions between the pion and vector meson fields.

Expanding in the curvature, we have

$$E_{\boldsymbol{\phi}} = \frac{1}{2}\int\left(|\partial_x\boldsymbol{\phi}|^2 + |\partial_z\boldsymbol{\phi}|^2\right)dxdz + \frac{p}{2}\int\left(-|\partial_x\boldsymbol{\phi}|^2 + 3|\partial_z\boldsymbol{\phi}|^2\right)z^2\,dxdz + \cdots \tag{2.3.11}$$

The first term in this expansion is the usual flat space sigma instanton energy, which has the well-known value of $4\pi B$. The second term is some contribution arising from the curvature of spacetime and, after changing to polar coordinates and making the

change of variable $y = (r/\mu)^2$, its leading-order contribution can be calculated as

$$E_{\boldsymbol{\phi}} = 4\pi B + p\pi B^2\mu^2 \int_0^\infty \frac{y^B}{(y^B+1)^2}\, dy + \cdots \tag{2.3.12}$$

We see that the influence of the curvature term, therefore, is to reduce the size of the instanton.

Using a similar expansion, the leading-order contribution from the vector meson part of the energy can be calculated as

$$E_\omega = \frac{g^2 B^4}{2\pi M^2\mu^2} \int_0^\infty \frac{y^{2(B-1)}}{(y^B+1)^4}\, dy + \cdots \tag{2.3.13}$$

In contrast to the curvature term, we see that the interaction with the vector meson field resists the shrinking of the instanton.

For $B = 2$ we can evaluate these integrals explicitly and obtain the leading-order correction to the energy as

$$E_{VM} = 8\pi + p\pi^2\mu^2 + \frac{g^2}{4M^2\mu^2} + \cdots \tag{2.3.14}$$

which is minimised when

$$\mu = \sqrt{\frac{g}{2\pi M\sqrt{p}}}\,. \tag{2.3.15}$$

We see that, as claimed, the radial flat-space approximations are valid for large g and large M, and in this regime the instanton solutions in the VM model closely resemble those in the BS model. In fact, substituting the expression for κ in (2.2.19) we find the preferred instanton size is $\mu = \sqrt{2\kappa}/p^{1/4}$, which is in exact agreement with the analysis performed in [62] for the BS model.

A similar calculation can be performed for all $B \geq 2$ to show that the preferred instanton size is proportional to $\sqrt{g/M}$ in the regime of large g and large M. However, the integral expressions in (2.3.12) and (2.3.13) do not converge for $B = 1$. A similar problem was encountered in [62] when studying the BS model, which arises since the quadratic approximation for $H(z)$ does not capture the slow decay behaviour of the $B = 1$ solution accurately enough. In analogy with this previous paper, we can insert the instanton ansatz of size μ into the expression for the energy (2.2.8) and minimise this numerically to find μ as a function of g and M. The result

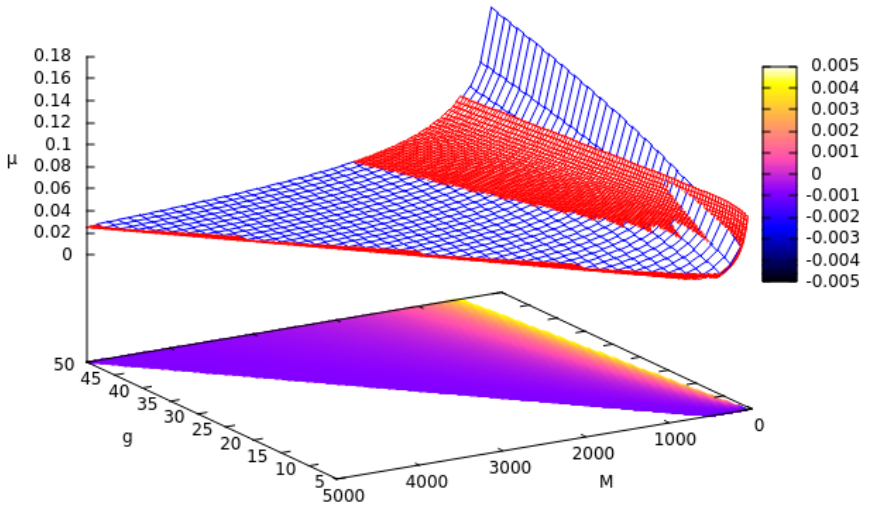

Figure 2.1: A plot of the soliton size μ against the model parameters g and $M \in [10g, 100g]$ for the $B = 1$ soliton within the instanton approximation. The red surface gives the numerical data, and the blue surface is a numerical fit to the data of the form $\mu = c\sqrt{g/(4\pi M)}$ with constant $c = 0.92$. The plot at the base gives the difference between these two surfaces, and is seen to be small.

for $p = \frac{1}{2}$ is displayed in Figure 2.1 for $g \in [5, 50]$ and $M \in [10g, 100g]$ (roughly corresponding to $\kappa \in [0.01, 0.001]$ after the identification (2.2.19)), where the red surface represents the numerical results and the blue surface is a fit to the data of the form $c\sqrt{g/(4\pi M)}$ with constant $c = 0.92$. The computation suggests that, in this regime, the size of the $B = 1$ soliton still has an approximate size $\mathcal{O}(\sqrt{g/M})$, in agreement with the analytic calculation for the $B = 2$ above.

In this two-dimensional model it is possible to obtain full numerical static solutions to the nonlinear field equations. All of the computations performed here are with $p = \frac{1}{2}$ and with the ratio $g/M = 0.1$ kept constant, so that in the large g, large M limit we expect solutions to look like those of the BS model with parameter $\kappa = g/(4\pi M) \approx 0.01$. In this limit the size of the soliton should be small compared to the curvature scale set by the metric. Numerical computations have been performed by minimising the energy (2.2.8) using second-order accurate finite difference approximations for spatial derivatives on a lattice with spacings $\Delta x = 0.005$, $\Delta z = 0.005$ and 2000×2000 numerical grid points. The energy minimisation

algorithm is a modified gradient flow mechanism (see Appendix A).

The results of our field theory computations for the $B = 1$ soliton are shown in Figure 2.2. The left image shows the ϕ_3 component of the pion field, as a pictorial representation of the soliton, for parameter values $M = 50$ and $g = 5$. The right image shows the corresponding vector meson field ω. The left image is almost indistinguishable from the numerical calculation of the $B = 1$ soliton in the BS model with parameter value $\kappa = 0.1/(4\pi) \approx 0.008$. This is confirmed by looking at the energies of each solution: the energy of the $B = 1$ VM soliton with $M = 50$ is given as $E = 4\pi \times 1.0107$, while the corresponding BS soliton has energy $E = 4\pi \times 1.0115$. Numerical computations for smaller M and g show that, as the parameter values decrease, the size of the VM soliton appears to decrease.

The numerical results for charge $B = 2$ are shown in Figure 2.3. For large parameter values we again find that the solitons of the VM and BS model are almost indistinguishable: an energy comparison yields $E = 8\pi \times 1.0072$ for the VM model soliton with $M = 50$, and $E = 8\pi \times 1.0075$ for the corresponding BS soliton. In these cases the $B = 2$ soliton resembles two $B = 1$ solitons separated by a small amount in the non-holographic direction. However, as we approach the region in which the approximation (2.3.10) breaks down (i.e. as M becomes small) we find qualitatively different behaviour, in which the $B = 1$ components of the $B = 2$ soliton begin to separate. For $M < 20$ the apparent separation between these components increases dramatically, as shown in the final image in Figure 2.3. We also see that as the parameters in the model decrease, the ω fields become more sharply localised around their centres. This is consistent with the analysis above where we found small derivatives in ω implied a large value of M.

Solitons with higher topological charge have also been numerically computed (see Figure 2.4), and are found to resemble chains of solitons separated in the non-holographic direction. This is to be expected due to the presence of the curvature in the holographic direction.

In [4] a zigzag arrangement of holographic baryons was predicted in finite density configurations in the Sakai-Sugimoto model, and in [62] it was argued that, for the low-dimensional BS analogue of the Sakai-Sugimoto model, a zigzag arrangement could

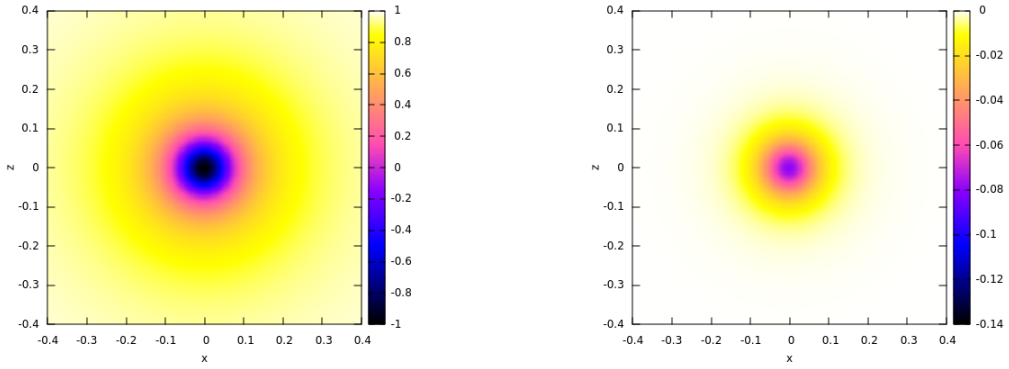

Figure 2.2: Plots of the numerically calculated $B = 1$ soliton fields for the $M = 50$ VM model. The third component of the pion field ϕ_3 is shown in the left column and the vector meson field ω is shown in the right column.

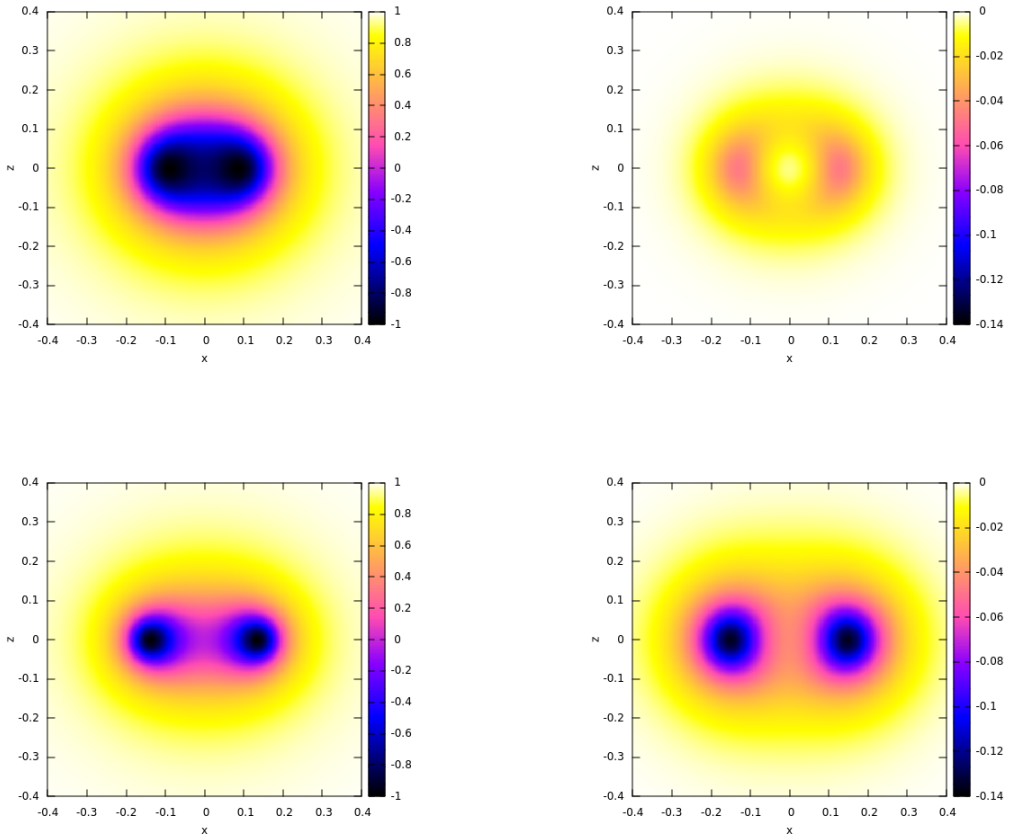

Figure 2.3: Plots of the numerically calculated $B = 2$ soliton fields for the $M = 50$ (top) and $M = 15$ (bottom) VM model. The third component of the pion field ϕ_3 is shown in the left column and the vector meson field ω is shown in the right column.

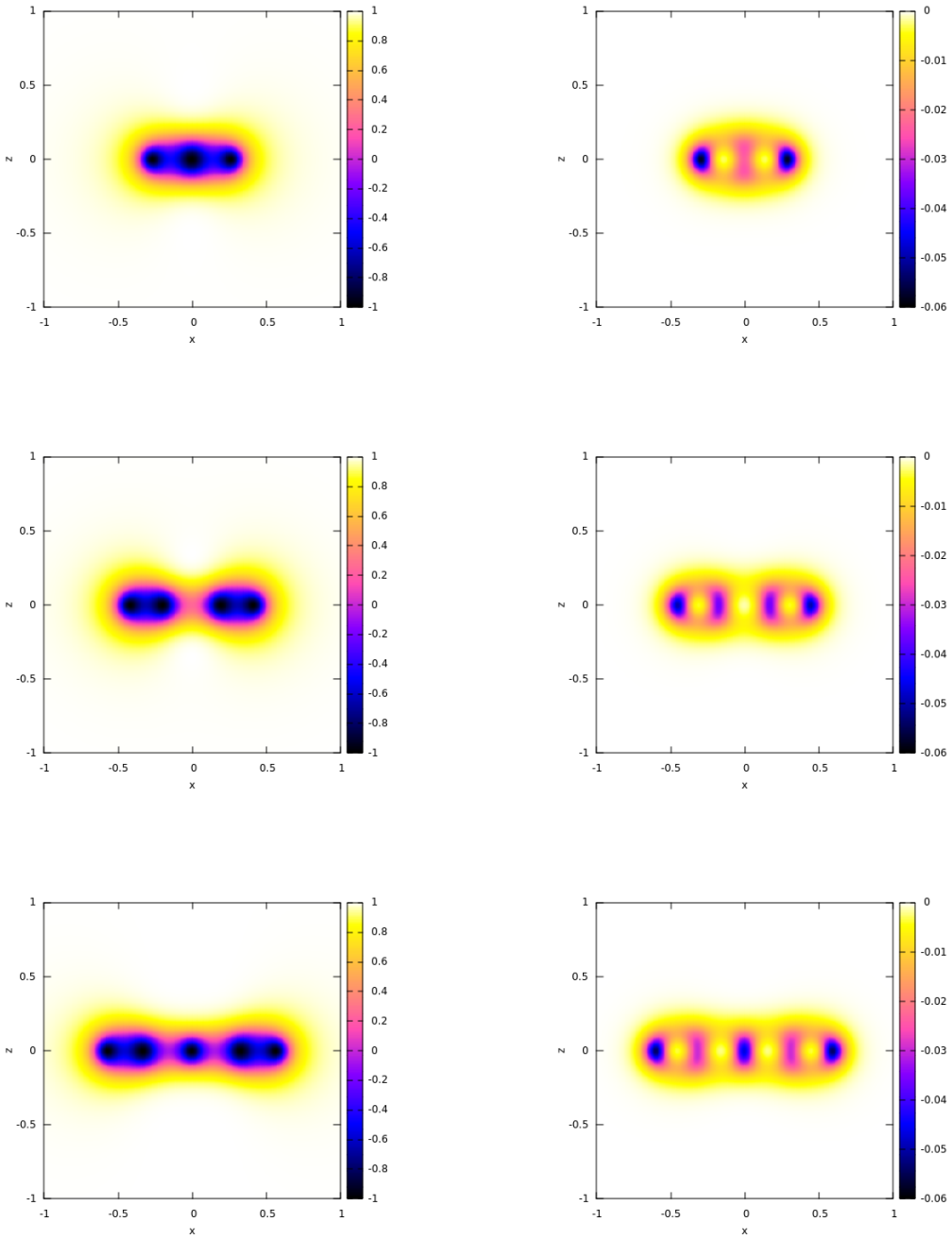

Figure 2.4: Plots of the numerically calculated soliton fields for $M = 50$ in the VM model with topological charges $B = 3$ (top), $B = 4$ (middle) and $B = 5$ (bottom). The third component of the pion field ϕ_3 is shown in the left column and the vector meson field ω is shown in the right column.

only be found if the preferred separation between pairs of solitons was much greater than the size of a single soliton. We have seen that, at low parameter values, the $B = 1$ VM solitons decrease in size and the $B = 2$ solitons resemble more widely separated $B = 1$ solitons, so it would be interesting to explore finite density chains of solitons in the VM model for small values of g and M. However, at these parameter values numerical solutions become more difficult to obtain (due to large derivatives of the ω field), so we will instead study a regime in which the parameters are "small, but not too small".

2.4 Finite density chains: new phases of popcorn

As explained in [62], analytical and numerical solutions of solitons at finite density in the Sakai-Sugimoto model are currently unavailable. Despite various levels of approximation being applied, even the relevant flat-space instanton approximations are not known explicitly after imposing periodic boundary conditions in multiple directions. However, the low-dimensional analogue we have been studying so far gives us the advantage of being able to numerically compute soliton solutions, and we shall compare our field theory simulations to the numerical and analytical results in [62]. In particular, we will find the appropriate popcorn phase transition in the VM model, and compare it both to the BS model, and to predictions made in [4] and [5] about finite-density baryons in the full Sakai-Sugimoto model.

In order to numerically compute solitons at finite density we restrict our numerical grid in the non-holographic direction to the range $-L \leq x \leq L$ and impose suitable boundary conditions for the fields at $x = \pm L$. In the following simulations we will always place periodic boundary conditions on ϕ_3 and ω, but may place periodic or anti-periodic boundary conditions on ϕ_1 and ϕ_2. There is still an integer topological charge, B, defined by integrating the $\mu = 0$ component of (2.2.7) in the range $(x, z) \in [-L, L] \times (-\infty, \infty)$, and this allows us to define a finite baryon density $\rho = B/2L$.

Initial conditions for numerical simulations are constructed as follows. First, by writing the flat-space instanton of charge $B = 1$ using Riemann sphere coordinates, we can

superpose a number of instanton solutions together using the product ansatz:

$$(W_1(\zeta), W_2(\zeta)) \to W(\zeta) = \frac{W_1 W_2}{W_1 + W_2}\,. \tag{2.4.1}$$

This has the property that W vanishes wherever W_1 or W_2 vanishes, and that far away from W_2 the solution looks like $W \approx W_1$ (and vice-versa). Therefore this product ansatz gives us a field configuration with the correct topological properties as a superposition of solitons at the positions of W_1 and W_2. Superposing a large number of such solitons with positions in the range $x \in [-nL, nL]$ for some $n \in \mathbb{Z}$ using the flat-space instanton ansatz from (2.3.1) and (2.3.2) can then give us an approximation to a periodic chain of solitons in the range $x \in [-L, L]$. An initial condition for the ω field can then be generated using (2.2.16). It should be noted that with this construction each soliton in the chain can be given an independent phase shift χ corresponding to a shift $\theta \to \theta + \chi$ in the ansatz (2.3.1).

Inspired by the results found in [62], we will begin our investigation by searching for two specific forms of finite-density chains by imposing certain symmetries, before going on to find the global energy minima for periodic solutions in the VM model.

The first chain to consider is a straight, single chain of solitons. Flat-space instantons of equal size separated in the non-holographic direction can be shown to be in the most attractive channel when they are exactly out of phase [28] (i.e. when the solitons have a relative phase shift of π), so we numerically seek these solutions by placing a single $B = 1$ ansatz on our numerical grid and imposing anti-periodic boundary conditions on ϕ_1 and ϕ_2. The datapoints in Figure 2.5 marked with a + represent the energy per soliton for numerical solutions of this type.

Secondly, we consider a two-layer square chain by placing a pair of solitons (with a relative phase shift of π) separated in the holographic direction, with anti-periodic boundary conditions imposed on ϕ_1 and ϕ_2 at $x = \pm L$. Symmetry constraints can force the resultant energy minima to form a regular square configuration of solitons (as observed in the BS model in [62]), although it can also allow configurations that resemble zig-zags or single chains of 2-solitons. The data points in Figure 2.5 marked with a $\times$ represent the energy per soliton for numerical solutions of this type.

Finally we consider initial conditions with four solitons placed in our grid in a line in the

non-holographic direction, with periodic boundary conditions on ϕ_1 and ϕ_2. By itself there would be a reflection symmetry $z \to -z$ which could force solutions to resemble those of the straight chains above, so we perturb the fourth soliton in the chain by a small amount in the holographic direction to break the symmetry. The symmetries of the grid here allow the potential for the initial conditions to relax to configurations resembling either the straight chains or the square chains, while also providing an opportunity to relax to other configurations with less symmetry. Figure 2.6 shows ϕ_3 and ω for different densities with $M = 50$, and the data points in Figure 2.5 marked with a $\square$ represent the energy per soliton for the numerical solutions. We see that at low and high densities respectively we can recreate the straight and square configurations described above, lending confidence that those are indeed the energy minima at these densities.

More interestingly we find that there exist configurations of solitons in the VM model that were not found in [62]. For densities $\rho \in [6.3, 7.6]$ (i.e. around the transition from the chain to the square solutions) we first observe a second-order transition from a chain to a period-4 wave. This is followed by a first-order transition to a wiggle, which then undergoes a second-order transition to the two-layered square configuration. This is in contrast with the results anticipated in [4] and [5], the former predicting a first-order popcorn transition from a chain to a two-layered zig-zag, and the latter suggesting a second-order transition from a chain to a period-3 wave followed by a first-order transition to the square configuration. Imposing period-3 boundary conditions in this low-dimensional model yielded solutions that were not energetically favourable to the period-4 waves, suggesting that the anticipated period-3 waves are not global energy minima. While the numerical investigations performed here are not definitive, the evidence suggests that popcorn transitions in these models may be more subtle than previously anticipated.

The results in both studies are, nonetheless, similar, and the differences could be due to the lower dimensionality of the VM model studied here: in [5] chain solutions were generated in the 4-dimensional space by imposing artificial curvature in the other spatial directions, whereas in the 2-dimensional VM model studied here there are no extra spatial dimensions.

Numerical field calculations for finite-density solitons were also performed for $M = 20$ and $g = 2$. These parameter values are very close to limits of the bounds implied by (2.3.10) and (2.3.15). Qualitatively similar results were obtained to the solutions with parameter values $M = 50$ and $g = 5$, although investigation of smaller parameter values beyond those bounds proved numerically difficult due to the presence of large derivatives in the ω field.

The numerical differences in energy between the wave and wiggle configurations compared to the chain and square configurations are incredibly close, differing by roughly $O(10^{-5})$. In light of this, it was instructive to return to the BS model and see if these configurations did, in fact, occur but were missed due to this similarity. After investigation it was found that the BS model does, indeed, exhibit these configurations around the transition from the chain to the square.

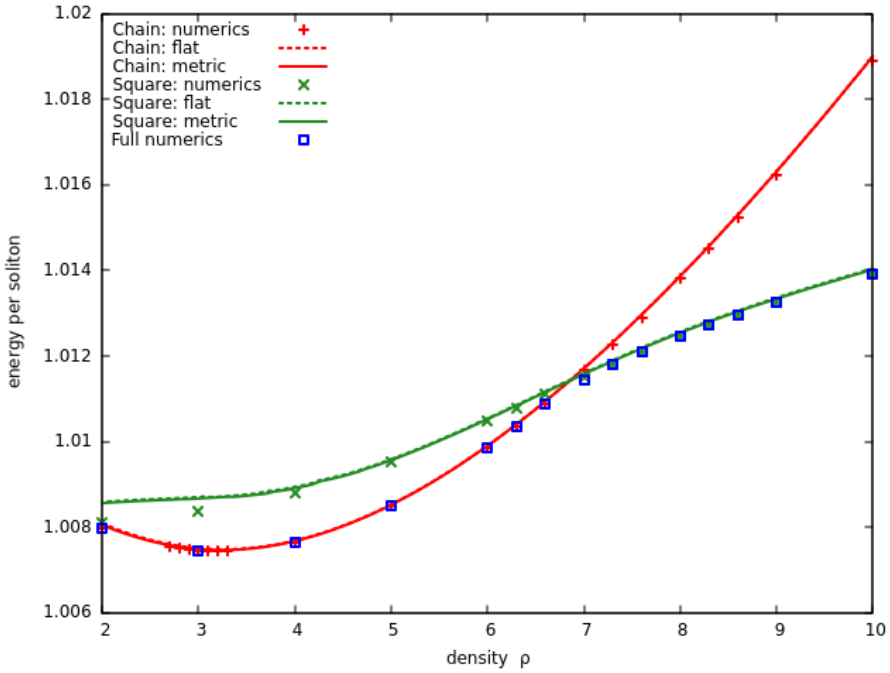

Figure 2.5: A plot of $E/(4\pi B)$ against density ρ for the forced chain and square configurations, as well as the energy minimising solutions, for $M = 50$. The data points represent the results of numerical simulations, whereas the curves represent the results of applying various semi-analytical approximations. The dotted lines are the results from approximating spacetime as flat, and the solid curves are the results from performing a first-order expansion of the metric factor $H(z)$.

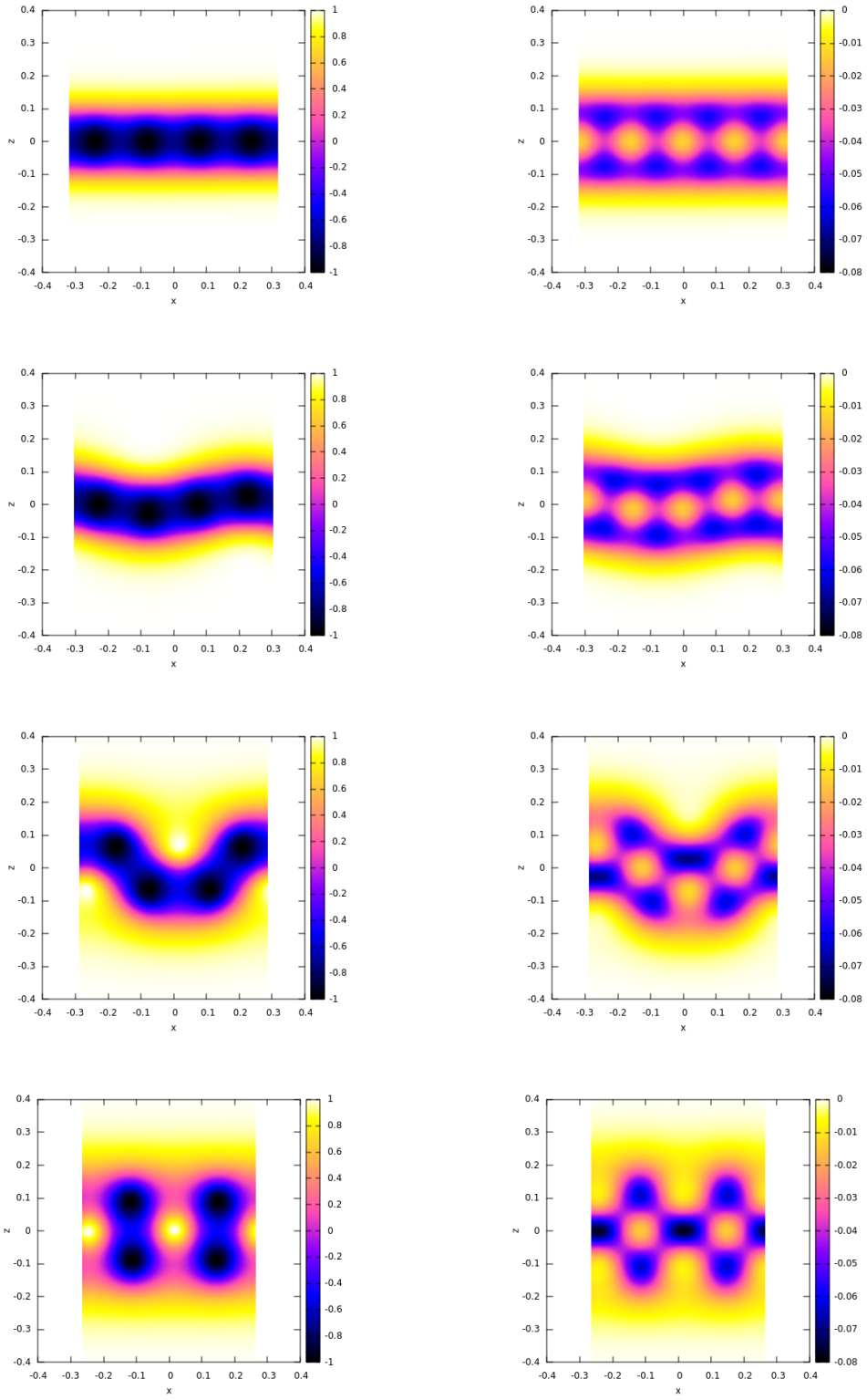

Figure 2.6: The left column shows plots of ϕ_3 for the energy minima of the VM model finite density chains with $M = 50$ for densities $\rho = 6.3$ (chain), 6.6 (wave), 7.0 (wiggle) and 7.6 (square), with density increasing from top to bottom. The right column shows the associated ω fields.

2.5 Semi-analytical methods of baryonic popcorn

Another advantage of the VM model over the BS model is that the ω field provides a low-dimensional analogue of the $U(1)$ gauge field in the full Sakai-Sugimoto model. This means we can use the VM model to test the validity of certain assumptions that are often made to simplify calculations in the full model. In [5] a number of assumptions regarding the fields in the Sakai-Sugimoto model are made in order to make analytical progress. These assumptions all rely on the solitons of the model being much smaller than the length scale set by the spacetime curvature, in which case it is argued that we can approximate spacetime as flat, and the fields by their flat-space counterparts. The $SU(2)$ gauge field is approximated by a flat-space self-dual Yang-Mills instanton, allowing techniques using ADHM constructions to be used to generate solutions. The $U(1)$ gauge field is approximated by constraining it to satisfy its flat-space equations of motion. In addition, the metric factors due to the curvature of spacetime are expanded as a leading-order Taylor series.

Since we have been able to obtain full numerical solutions in our low-dimensional model, we can apply analogues of these approximations to test their validity in the VM model. Focusing on the forced chain and square configurations allows us to obtain analytical approximations for the pion fields, and perform numerical minimisations to obtain the corresponding ω fields.

For the chain configurations we can write a flat-space instanton solution (in Riemann sphere coordinates) as

$$W(\zeta) = \frac{\sin(\pi\rho\zeta)}{\mu\pi\rho}\,. \tag{2.5.1}$$

This has zeroes whenever $x = n/\rho$, $n \in \mathbb{Z}$ and obeys the symmetry relation $W(\zeta + \rho^{-1}) = -W(\zeta)$, so describes a chain of instantons at density ρ where neighbouring instantons are exactly out of phase with each other. To obtain the square configurations we can simply take a product ansatz of the form (2.4.1) with the choice

$$W_1 = \frac{\sin(\pi\rho(\zeta - i\delta)/2)}{\mu\pi\rho}\,, \qquad W_2 = \frac{-\sin(\pi\rho(\zeta + i\delta)/2)}{\mu\pi\rho} \tag{2.5.2}$$

to obtain a a pair of chains separated by a distance δ in the holographic direction.

Requiring that the ω field satisfies its flat-space equation of motion is equivalent to setting $H(z) = 1$ in (2.2.12):

$$(\nabla^2 - M^2)\omega = -\frac{g}{4\pi}\boldsymbol{\phi} \cdot (\partial_x \boldsymbol{\phi} \times \partial_z \boldsymbol{\phi}) \,. \tag{2.5.3}$$

Combining this equation with the instanton approximation above allows us to perform numerical minimisation of the energy (2.2.8) over the parameters μ and/or δ for a large number of densities, where at each value of $\{\rho, \mu, \delta\}$ we solve (2.5.3) numerically using a successive over-relaxation method with red-black ordering. The minimisation in parameter space was performed with a golden section search method (in the case of 1 parameter) and a Nelder-Mead algorithm (in the case of 2 parameters). The results of these investigations are shown by the curves in Figure 2.5. As can clearly be seen, the energies associated with these approximations are very close to the full numerical values, lending confidence to the credibility of these assumptions. In addition, the effect of Taylor-expanding the metric factor $H(z)$ to leading order in the energy density was also investigated. The curves produced are also shown in Figure 2.5, although it is difficult to see them since they essentially overlap with the flat-space approximation. This suggests that Taylor-expanding the metric is also a reasonable assumption in this regime of the model.

2.6 Conclusions

In this chapter we have investigated an alternative low-dimensional analogue of the Sakai-Sugimoto model to describe holographic baryons, namely an $O(3)$ sigma model stabilised by vector mesons in a warped spacetime. We have found solitons, multi-solitons and finite density solitons in this model and compared them to solitons in the baby Skyrme model and to instanton approximations, and found all three to be similar given certain parameter constraints. We have also shown that solitons in the vector meson model can differ qualitatively when these parameters are allowed to violate such constraints.

In addition, we have used the vector meson model to investigate the low-dimensional

analogue of the baryonic popcorn phenomenon, and found a set of new phase transitions (although such phase transitions are present in the baby Skyrme model, but were previously overlooked). We have used the vector meson model to test common approximations for the low-dimensional analogue of the $U(1)$ gauge field of the Sakai-Sugimoto model, and found that approximating the pion and vector meson fields by flat-space solutions and using a leading-order expansion of the metric are both good approximations.

When analysing the instanton approximations for finite-density solitons, only a very restricted set of instanton configurations were considered. It might be of interest to explore this area more fully to investigate the baryonic popcorn phase transition, by numerically minimising the energy of solutions where more instanton moduli (i.e. their positions and phases) are also allowed to vary. It may also be of interest to apply the various approximations tested here to high-density lattices of solitons in the full Sakai-Sugimoto model. Finally, although it is computationally much more difficult, it would be interesting to see how the phenomena observed in the vector meson model change for very small parameter values, since in this regime the model is no longer well-approximated by the baby Skyrme model.

Chapter 3

Baby Skyrmions in anti-de Sitter spacetime

3.1 Introduction

As described in Section 1.3, the Skyrme model is a nonlinear theory in (3 + 1) dimensions, admitting soliton solutions called Skyrmions. It has been derived as a low-energy effective field theory description of QCD and has recently been used to study holographic models such as the Sakai-Sugimoto model (see Section 1.4). A key feature of these holographic models is that the bulk spacetime is AdS-like, possessing a conformal boundary and a finite, negative scalar curvature.

Solitons in pure anti de-Sitter spacetimes are also of interest. It has been shown that Skyrmions with massless pions in hyperbolic space are closely related to Skyrmions with massive pions in Euclidean space [64, 65]. Since constant time slices of AdS spacetimes are hyperbolic we may expect similar results in pure AdS. In addition, monopoles and monopole walls have been studied in AdS [66, 67], motivated as a magnetic version of holographic superconductors.

The baby Skyrme model (see Section 1.2) is a natural low-dimensional analogue of the Skyrme model, and in the previous chapter baby Skyrmions were studied in the context of toy models of holographic QCD. In these toy models a series of so-called popcorn transitions were observed in which finite-density chains of solitons split into multiple layers with increasing density.

In this chapter we will investigate the baby Skyrme model in a pure AdS background and study the resulting soliton and multi-soliton solutions. The low dimensionality of the model makes full numerical field computations viable, and we find that the curvature of the spacetime allows us to find soliton solutions even without a pion mass term. Multi-solitons beyond topological charge $B = 3$ are found to take the form of ring-like structures, with popcorn-like phase transitions to multi-layered rings occurring as the topological charge increases. Inspired by methods used to study aloof (loosely bound) baby Skyrmions [68] we will derive a point-particle approximation to study these phase transitions for higher topological charges.

This chapter is based on collaborative work published in [7].

3.2 AdS spacetime in $(2+1)$ dimensions

AdS is the maximally symmetric spacetime with Minkowskian signature and constant negative curvature, and in this chapter we will be interested in the $(2+1)$-dimensional case. The metric, given in so-called sausage coordinates, can be written

$$ds^2 = -\left(\frac{1+r^2}{1-r^2}\right)^2 dt^2 + \frac{4L^2}{(1-r^2)^2}\left(dx^2+dy^2\right) . \tag{3.2.1}$$

Here, L is the AdS radius (related to the cosmological constant Λ via $\Lambda = -1/L^2$) and $r = \sqrt{x^2+y^2} \in [0,1)$ is a radial coordinate. These coordinates are useful numerically as they are global coordinates over a finite range. Later we will use that the geodesic distance between two points $\boldsymbol{x}$ and $\boldsymbol{y}$ in this spacetime is given by

$$d(\boldsymbol{x},\boldsymbol{y}) = L\cosh^{-1}\left(1+\frac{2|\boldsymbol{x}-\boldsymbol{y}|^2}{(1-|\boldsymbol{x}|^2)(1-|\boldsymbol{y}|^2)}\right) . \tag{3.2.2}$$

The following global coordinates give another useful way of writing the AdS metric:

$$ds^2 = -\cosh^2\frac{\rho}{L}\,dt^2 + d\rho^2 + L^2\sinh^2\frac{\rho}{L}\,d\theta^2 , \tag{3.2.3}$$

where $\rho \geq 0$. These coordinates are useful since the radial coordinate ρ coincides with the geodesic distance from the origin in this model. The global and sausage coordinates are related by $r = \tanh\frac{\rho}{2L}$.

Since constant time slices of AdS are hyperbolic space, it will be useful to define a hyperbolic translation in sausage coordinates. A translation sending the origin to some point $\boldsymbol{a}$ is given by

$$\boldsymbol{x} \mapsto \frac{(1-|\boldsymbol{a}|^2)\boldsymbol{x} + (1+2\boldsymbol{x}\cdot\boldsymbol{a}+|\boldsymbol{x}|^2)\boldsymbol{a}}{1+2\boldsymbol{x}\cdot\boldsymbol{a}+|\boldsymbol{a}|^2|\boldsymbol{x}|^2}\,. \tag{3.2.4}$$

It should be noted that this is an isometry of only the constant time slices of the spacetime, rather than the full spacetime, since the time component of the metric is dependent on the radial coordinate r.

As a final note, the Ricci scalar curvature of AdS can be calculated as $R = -6/L^2$. In the limit $L \to \infty$ this curvature vanishes and we recover flat space.

3.3 The AdS baby Skyrme model

We will be interested in studying soliton solutions of the baby Skyrme model, given by the action

$$S_{BS} = -\frac{1}{2}\int\Big\{\partial_\mu\boldsymbol{\phi}\cdot\partial^\mu\boldsymbol{\phi} + \frac{\kappa^2}{2}(\partial_\mu\boldsymbol{\phi}\times\partial_\nu\boldsymbol{\phi})\cdot(\partial^\mu\boldsymbol{\phi}\times\partial^\nu\boldsymbol{\phi}) + 2m^2(1-\boldsymbol{\phi}\cdot\boldsymbol{n})\Big\}\sqrt{-\det g}\,dxdydt\,. \tag{3.3.1}$$

The field $\boldsymbol{\phi} = (\phi_1, \phi_2, \phi_3)$ is a three component unit vector. The first term is that of the $O(3)$ sigma model, and the second term is the baby Skyrme term with constant coefficient κ^2. The third term is a potential term containing the pion mass parameter m (named in analogy with the pion mass term in the full Skyrme model), and a constant unit vector $\boldsymbol{n}$. Greek indices run over spacetime coordinates t, x and y, and later we will use Latin indices to run over the purely spatial coordinates. The symmetry of the action is $O(3)$ for $m = 0$ and $O(2)$ for $m \neq 0$.

The associated static energy of this model is

$$E_{BS} = \frac{1}{2}\int\frac{1+r^2}{1-r^2}\Big\{|\partial_x\boldsymbol{\phi}|^2 + |\partial_y\boldsymbol{\phi}|^2 + \frac{\kappa^2(1-r^2)^2}{4L^2}|\partial_x\boldsymbol{\phi}\times\partial_y\boldsymbol{\phi}|^2 + \frac{8L^2m^2}{(1-r^2)^2}(1-\boldsymbol{\phi}\cdot\boldsymbol{n})\Big\}\,dxdy\,, \tag{3.3.2}$$

from which we can see the effect of our choice of time coordinate. Without the factor $\sqrt{-g_{00}} = (1+r^2)/(1-r^2)$, the hyperbolic translations (3.2.4) would be isometries of

the static energy, and solutions translated from the origin would have equal energies. The metric factor $\sqrt{-g_{00}}$ can then be seen to energetically penalise solutions that lie away from the spatial origin $r = 0$, since $\sqrt{-g_{00}} \geq 1$.

The equations of motion for this model are then

$$\begin{aligned} \partial_i \boldsymbol{j}_i &\equiv \partial_i \left\{ \frac{1+r^2}{1-r^2} \left(\boldsymbol{\phi} \times \partial_i \boldsymbol{\phi} + \frac{\kappa^2 (1-r^2)^2}{4L^2} \partial_j \boldsymbol{\phi} (\boldsymbol{\phi} \cdot \partial_i \boldsymbol{\phi} \times \partial_j \boldsymbol{\phi}) \right) \right\} \\ &= m^2 \sqrt{-\det g}\, \boldsymbol{n} \times \boldsymbol{\phi} \,. \end{aligned} \tag{3.3.3}$$

For finite energy we then require $\boldsymbol{\phi} \to \boldsymbol{n}$ as $r \to 1$. Without loss of generality we can choose $\boldsymbol{n} = (0, 0, 1)$, and in the massless ($m = 0$) case this choice of boundary value breaks the $O(3)$ symmetry of the model to $O(2)$. We can identify points on the boundary $r = 1$ and treat the pion fields as maps $\boldsymbol{\phi} : S^2 \to S^2$, giving rise to an associated winding number and topological charge

$$B = -\frac{1}{4\pi} \int \boldsymbol{\phi} \cdot (\partial_x \boldsymbol{\phi} \times \partial_y \boldsymbol{\phi})\, dxdy \tag{3.3.4}$$

which we identify with the baryon number of the configuration. By noting the inequalities

$$|\partial_x \boldsymbol{\phi} \pm \boldsymbol{\phi} \times \partial_y \boldsymbol{\phi}|^2 \geq 0 \,, \quad \frac{1+r^2}{1-r^2} \geq 1 \,, \tag{3.3.5}$$

we obtain the Bogomolny bound $E_{BS} \geq 4\pi |B|$.

3.4 Radial baby Skyrmions in AdS

We begin by discussing some properties of radially symmetric solitons in our model, working in global coordinates (3.2.3). Due to the principle of symmetric criticality [69] and the symmetries of both AdS and the action, we would expect static $B = 1$ solitons in our model to posses radial symmetry and be centred at the origin $\rho = 0$. Static, radially symmetric configurations with topological charge B are given by the hedgehog ansatz

$$\boldsymbol{\phi} = (\sin f(\rho) \cos\left(B(\theta - \psi)\right), \sin f(\rho) \sin\left(B(\theta - \psi)\right), \cos f(\rho)) \tag{3.4.1}$$

where $f(\rho)$ is some profile function satisfying $f(0) = \pi$, $f(\infty) = 0$. We set the constant internal phase ψ to zero due to symmetry, although internal phase differences will become important when we consider multi-solitons. Substituting into (3.3.2) and performing the coordinate transformation yields the static energy

$$E_{rad} = \frac{L\pi}{2}\int_0^\infty \sinh\frac{2\rho}{L}\left\{f'^2 + \frac{B^2\sin^2 f}{L^2\sinh^2\frac{\rho}{L}}(1+\kappa^2 f'^2) + 2m^2(1-\cos f)\right\}d\rho \tag{3.4.2}$$

and equation of motion

$$\begin{aligned}\partial_\rho\left\{\sinh\frac{2\rho}{L}\left(L^2 + \frac{B^2\kappa^2\sin^2 f}{\sinh^2\frac{\rho}{L}}\right)f'\right\} \\ = \sinh\frac{2\rho}{L}\sin f\left(\frac{B^2\cos f}{\sinh^2\frac{\rho}{L}}(1+\kappa^2 f'^2) + m^2L^2\right).\end{aligned} \tag{3.4.3}$$

We can numerically find the profile functions $f(\rho)$ for different values of B by minimising (3.4.2) using a modified gradient flow method. Figure 3.1 displays the numerical results for topological charges $1 \leq B \leq 3$ and parameter values $\kappa = 0.1$, $L = 1$, where we have used fourth-order accurate approximations for derivatives on a grid with 2001 points. As a comparison we can also perform full-field numerical minimisations on (3.3.2) and extract the profile function associated with radially symmetric fields. By using a hedgehog ansatz as an initial condition and performing a gradient flow mechanism with fourth-order accurate derivatives on a grid with 501×501 gridpoints we find radial energy minima for charges $1 \leq B \leq 3$ that are identical to the numerical solutions to (3.4.3).

In other baby Skyrme models it has been found that radial solitons can be well-approximated by flat-space instantons of the $O(3)$ sigma model [62]. This approximation has enabled an investigation of how the soliton sizes μ scale with the baby Skyrme parameter κ. Unfortunately $O(3)$ sigma instantons in AdS do not have a convenient closed form expression, due to the presence of the non-constant time component of the metric, preventing us from analytically exploring this relationship. We can nevertheless perform a numerical investigation; since the profile function interpolates between π and 0 we can define the size of the soliton as the value μ that satisfies $f(\mu) = \pi/2$.

Using this definition it is straightforward to numerically find how μ scales with κ and

L for different values of B, as can be seen in Figure 3.2. In the massless case we find the leading-order dependence is $\mu \sim \sqrt{\kappa L}$ for small κ/L; looking at (3.4.2) we see that nonlinear effects will dominate when κ/L is large. Comparing this to the scaling of baby Skyrmions with mass parameter $m > 0$ in flat space, $\mu \sim \sqrt{\kappa/m}$, we can see that the curvature of AdS space can be interpreted as adding an effective pion mass.

Finally, we can calculate the leading-order decay of the soliton tails near the boundary of our space. Assuming a radial ansatz, and using the fact that $f(\rho) \to 0$ as $\rho \to \infty$, we can linearise the equations of motion to obtain

$$L^2 \sinh \frac{2\rho}{L} f'' + 2L \cosh \frac{2\rho}{L} f' - \sinh \frac{2\rho}{L} \left(\frac{B^2}{\sinh^2 \frac{\rho}{L}} + m^2 L^2 \right) f = 0 \,. \tag{3.4.4}$$

In the limit $\rho \to \infty$ we can obtain the asymptotic tail decay as

$$f(\rho) \sim e^{-\left(1+\sqrt{1+m^2L^2}\right)\rho/L} \,, \tag{3.4.5}$$

independently of κ or B. This relation also holds in the special case $m = 0$. It is interesting to note that, unlike baby Skyrme models in flat space, the addition of a mass term is not required for the soliton tail to decay exponentially. This is in contrast with baby Skyrmions in flat space which have large-radius asymptotic tail decays

$$f(r) \sim \begin{cases} r^{-B}, & \text{if } m = 0 \\ \frac{1}{\sqrt{r}} e^{-mr}, & \text{if } m \neq 0 \,. \end{cases} \tag{3.4.6}$$

In fact, these flat-space tail decays can be obtained from the linearised asymptotic equations of motion by carefully taking the limit $L \to \infty$, as expected.

3.5 Multi-solitons in AdS

As we shall see, for topological charges $B > 3$, radial baby Skyrmions in AdS no longer provide global minima for the energy functional (3.3.2). Analytic investigation of higher charge solitons is difficult, but we are able to perform full numerical minimisations to seek out local and global energy minima. The numerical results in this section were obtained by performing a modified gradient flow method on the energy (3.3.2) with parameter values $\kappa = 0.1$, $L = 1$, $m = 0$ on a grid with 501×501 gridpoints in

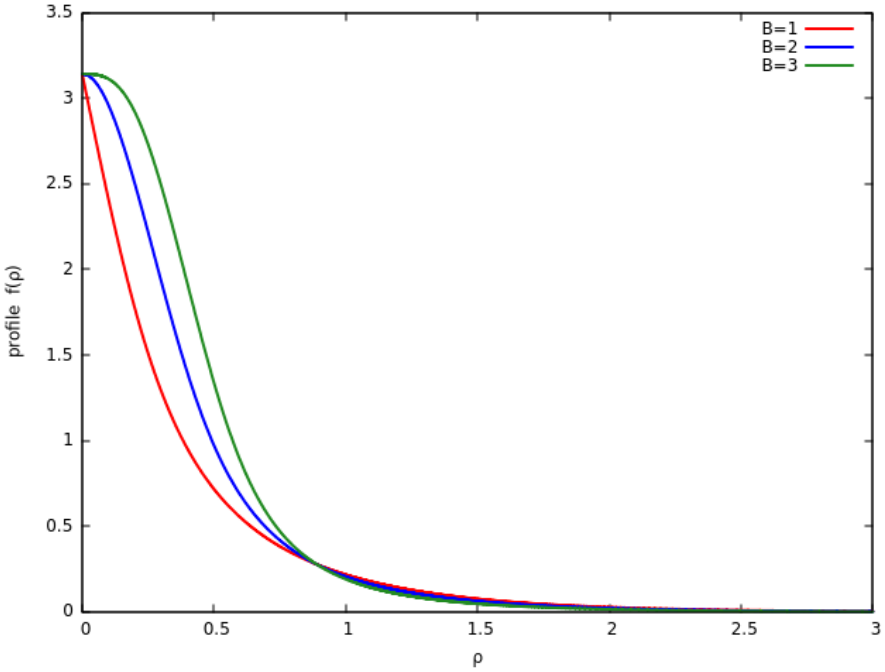

Figure 3.1: Numerically computed radial AdS baby Skyrmion profile functions as a function of geodesic distance ρ for topological charges $1 \leq B \leq 3$, with $\kappa = 0.1$ and $L = 1$.

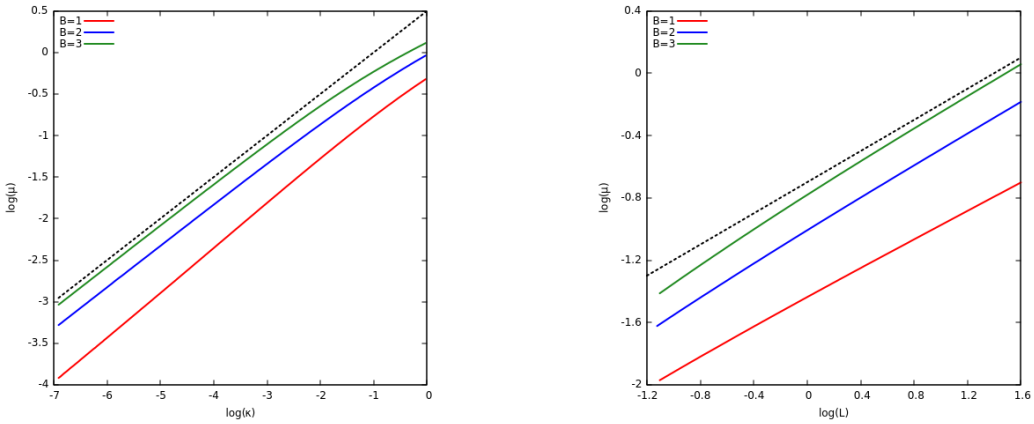

Figure 3.2: Log-log plots demonstrating how the soliton size μ varies with the baby Skyrme parameter κ (left, with fixed $L = 1$) and the AdS radius L (right, with fixed $\kappa = 0.1$) for radial AdS baby Skyrmions with $1 \leq B \leq 3$. The dashed lines have gradient 0.5, showing that the sizes scale approximately as $\mu \sim \sqrt{\kappa L}$ for small κ/L.

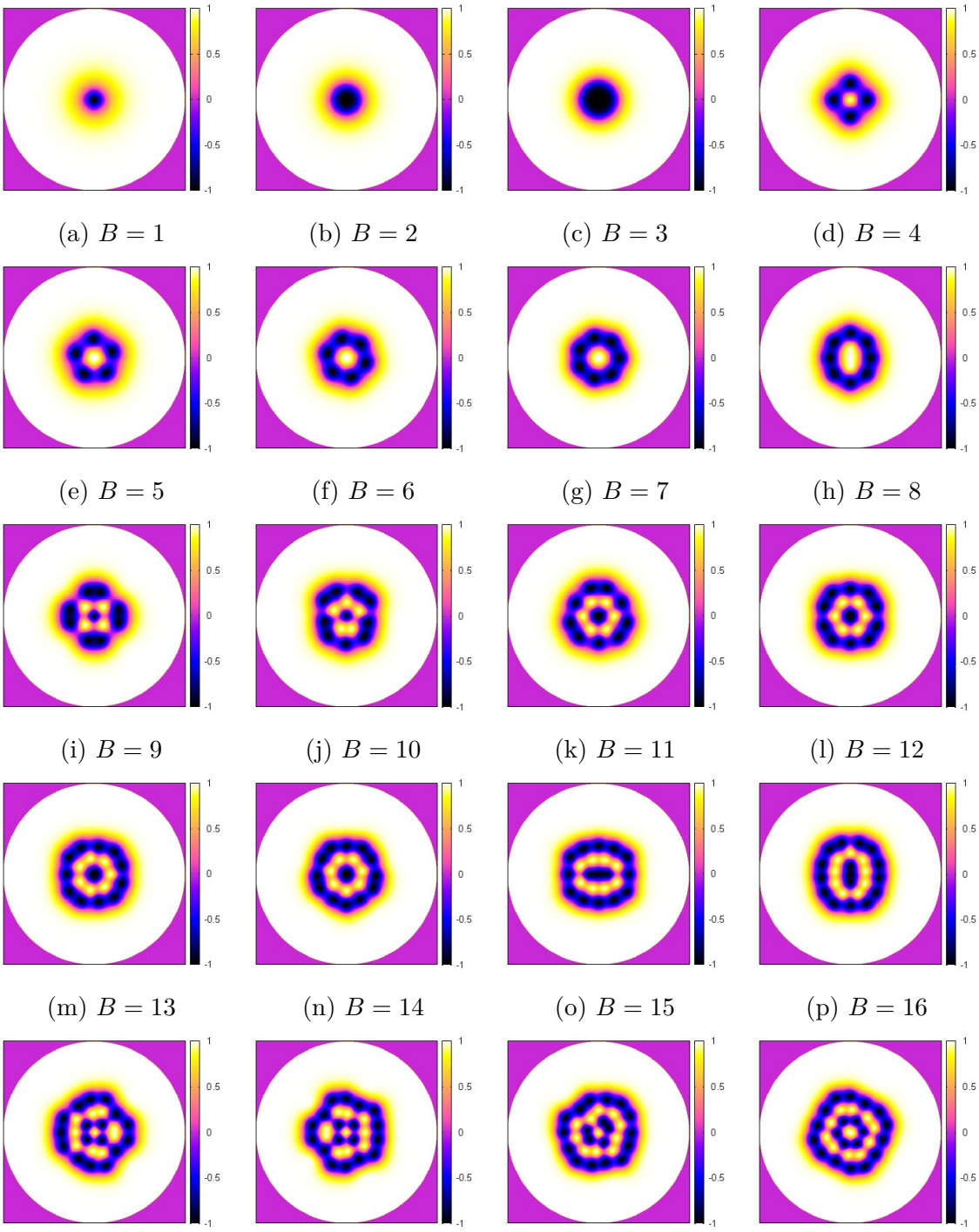

(a) $B = 1$ (b) $B = 2$ (c) $B = 3$ (d) $B = 4$

(e) $B = 5$ (f) $B = 6$ (g) $B = 7$ (h) $B = 8$

(i) $B = 9$ (j) $B = 10$ (k) $B = 11$ (l) $B = 12$

(m) $B = 13$ (n) $B = 14$ (o) $B = 15$ (p) $B = 16$

(q) $B = 17$ (r) $B = 18$ (s) $B = 19$ (t) $B = 20$

Figure 3.3: Plots of the numerically calculated AdS baby Skyrmions for topological charges $1 \leq B \leq 20$ for $\kappa = 0.1$, $L = 1$ and $m = 0$. We plot ϕ_3 in sausage coordinates as a visual representation of the solitons.

sausage coordinates. Derivatives were calculated using fourth-order finite difference approximations. In addition, the numerical results were verified by applying a fourth-order Runge-Kutta method to the full dynamical equations of motion.

In order to find local energy minima we investigated a range of different initial conditions for our minimisation algorithms. Initial conditions were primarily generated using the product ansatz (2.4.1) combined with the hyperbolic translations (3.2.4), allowing us to generate configurations that resemble collections of radial baby Skyrmions placed in different positions on our grid. We also used perturbed radial fields as initial conditions.

Figure 3.3 shows colour contour plots of ϕ_3 for numerically found global energy minima for topological charges $1 \leq B \leq 20$, with energies given in Table 3.1 and Figure 3.4.

For the pion mass term used in this section, radial solutions are preferred up to charge $B = 3$, in contrast to baby Skyrmions in flat space which only have radial energy minima for $B \leq 2$.

For $4 \leq B \leq 7$ the baby Skyrmions form regular polygons, with soliton positions at the vertices. The relative phase differences between neighbouring soliton positions is π or $\pi \pm \pi/B$ for even or odd charges respectively.

At charge $B = 8$ the ring structure deforms due to the centralising force induced by the AdS metric. For $B \geq 9$ the solutions form multi-layered concentric rings, and the central layers for $9 \leq B \leq 16$ resemble (normally slightly deformed) radial solutions. These deformations appear to match the symmetries of the outer rings. We denote multi-layered ring structures as $\{n_1, n_2, n_3, \dots\}$, where n_i denotes the topological charge in the ith ring, counting out from the origin.

The transition from a single ring to a multi-ring structure with increasing baryon number is reminiscent of the popcorn transition observed in low-dimensional analogues of the Sakai-Sugimoto model of holographic QCD [62, 6], in which finite density chains of solitons pop out into a holographic direction at some critical density. In light of this, it would be interesting to see if the AdS baby Skyrme model studied here possesses further popcorn-like transitions beyond $B = 20$.

This is a potentially difficult task to accomplish numerically. As higher charge solutions are investigated the number of local energy minima increases drastically. This requires

charge B	$E/4\pi B$	form	charge B	$E/4\pi B$	form
1	1.2548	{1}	11	1.5368	{2, 9}
2	1.2312	{2}	12	1.5554	{2, 10}
3	1.2878	{3}	13	1.5788	{2, 11}
4	1.3384	{4}	14	1.6017	{2, 12}
5	1.3725	{5}	15	1.6250	{3, 12}
6	1.3886	{6}	16	1.6481	{3, 13}
7	1.4263	{7}	17	1.6714	{4, 13}
8	1.4541	{8}	18	1.6914	{4, 14}
9	1.4888	{1, 8}	19	1.7107	{5, 14}
10	1.5157	{1, 9}	20	1.7276	{6, 14}

Table 3.1: Energies per charge (in units of 4π) and forms for AdS baby Skyrmions with topological charge $1 \leq B \leq 20$.

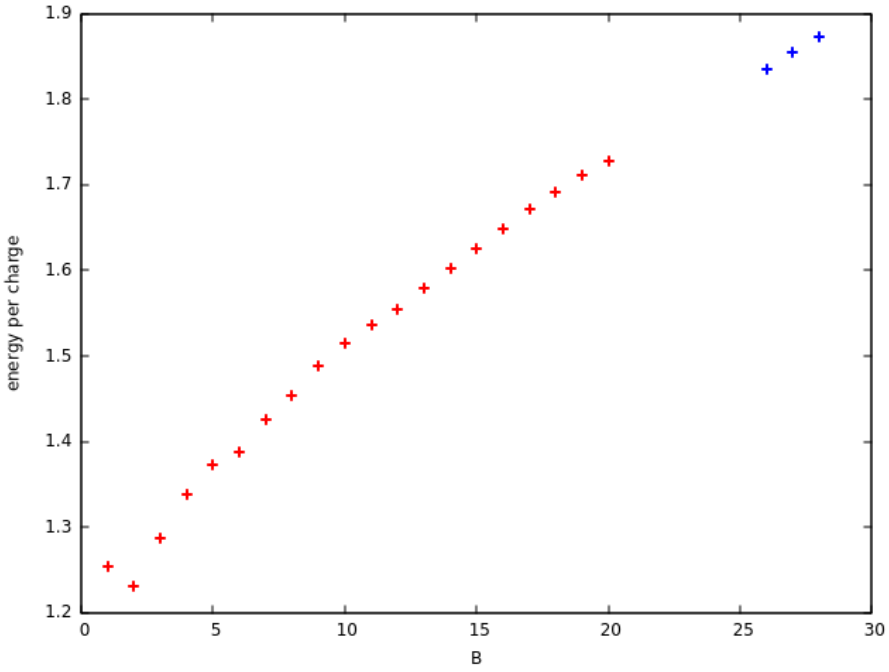

Figure 3.4: Energies per charge $E/(4\pi B)$ for AdS baby Skyrmions with topological charge $1 \leq B \leq 20$ (red). Also shown are the energies per charge for $26 \leq B \leq 28$ (blue).

a very large number of initial conditions to be tested in order to gain confidence that a global energy minimum has indeed been found.

In the following sections we will formulate an approximation to our system in which the solitons are modelled by point particles in a gravitational potential with an inter-soliton interaction. We will use this model to predict the baryon numbers at which further popcorn transitions occur, and use the predictions as a guide to finding further global minima in the full model.

3.6 AdS baby Skyrmions as point particles

The numerical results from the previous section are reminiscent of the results of circle packings within a circle [70]: finding the minimal area circle within which you can pack B congruent circles. Solutions tend to be arranged as rings of points separated by at least the diameter of the circles ($\sim 2\mu$ for our baby Skyrmions). However, using this as an approximation to the AdS baby Skyrme model presents some problems. Firstly, the popcorn transitions occur too early, the first two around $B = 7$ and $B = 19$. Secondly, the configurations do not always remain "popped": for example the $B = 7$ packing is of the form $\{1, 6\}$ whereas the $B = 8$ and $B = 9$ packings are single rings. This is likely due to both the malleable and overlapping nature of the baby Skyrmions, and the forces between them. However it does suggest that a point-particle approximation could be able to qualitatively predict the form of solutions, if a better representation of the soliton interactions can be found.

In order to derive a better point-particle approximation it will be necessary to obtain numerical approximations to the effective gravitational potential and inter-soliton interaction. We will make use of the hyperbolic translations (3.2.4), and assume that the energies of radial fields translated in this way can approximate the energies of constituent parts of multi-soliton configurations located at different points on our grid. It should be clarified that such fields are not solutions to the equations of motion since the hyperbolic translations are not isometries of AdS.

3.6.1 The gravitational potential

We begin by deriving an approximate gravitational potential from the metric (3.2.1). The geodesic equations associated with this metric are given by

$$\begin{aligned} t'' &= -\frac{8}{1-r^4}(xx'+yy')t' \,, \\ x'' &= -\frac{x(1+r^2)}{L^2(1-r^2)}(t')^2 + \frac{2x}{1-r^2}(y')^2 - \frac{4x}{1-r^2}x'y' \,, \\ y'' &= -\frac{y(1+r^2)}{L^2(1-r^2)}(t')^2 + \frac{2y}{1-r^2}(x')^2 - \frac{4y}{1-r^2}x'y' \,, \end{aligned} \tag{3.6.1}$$

where primes denote differentiation with respect to proper time. In the non-relativistic limit x', $y' \ll t'$ we can write

$$\ddot{x} = \frac{x''}{(t')^2} - \frac{x't''}{(t')^3} \approx \frac{x''}{(t')^2} \approx -\frac{x(1+r^2)}{L^2(1-r^2)} \equiv -\frac{x}{r}\partial_r\Phi \,, \tag{3.6.2}$$

where we have implicitly defined the gravitational potential $\Phi(r)$. Integrating along with the condition $\Phi(0) = 0$ gives

$$\Phi(r) = \int_0^r \frac{R(1+R^2)}{L^2(1-R^2)}\,dR = -\frac{1}{2L^2}(r^2 + 2\log(1-r^2)) \,. \tag{3.6.3}$$

To fit this potential to the AdS baby Skyrme model we are required to multiply it by some constant factor α. We obtain a numerical approximation for the gravitational potential by evaluating the energies of translated $B = 1$ radial fields and subtracting off the energy of the true $B = 1$ solution. We then fit α to this data by performing a least-squares fit. We fit only within the radius $r = 0.6$ because full numerical local minima, even for high charges, do not lie much beyond this radius, and the hyperbolic translated $B = 1$ fields become less accurate as approximations when closer to the edge of the disc. In addition, we investigated different radii to fit our data to, and found that choosing values larger than 0.6 resulted in point-particle approximations that did not successfully estimate the full numerical results.

Figure 3.5 shows the analytic potential for $\alpha = 64.3$ compared to the numerical approximations with $\kappa = 0.1$, $L = 1$. The curves are in close agreement for radii in the range $r \in [0, 0.6]$, but diverge as r increases further, as expected.

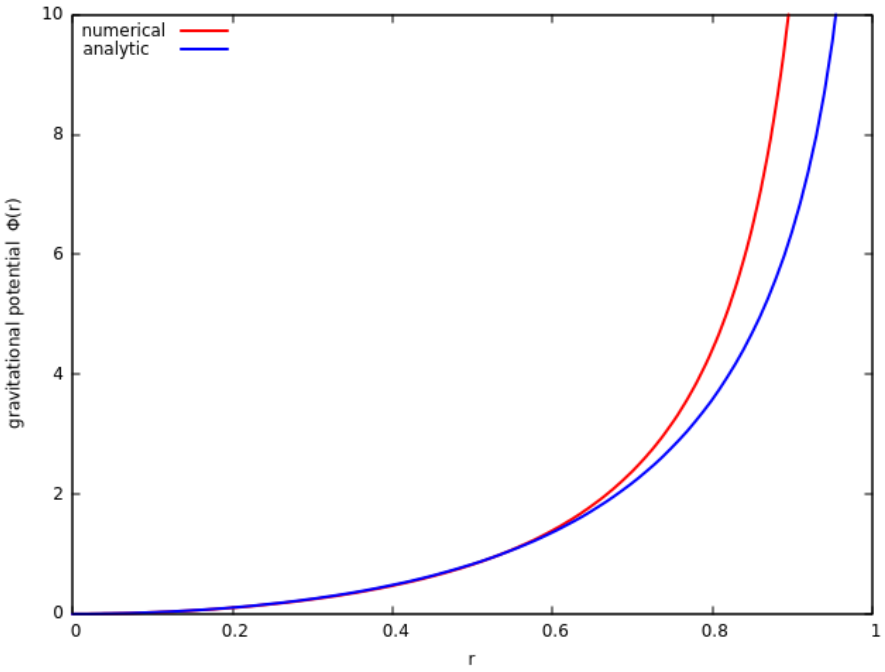

Figure 3.5: Numerical and analytical approximations for the gravitational potential induced by the AdS metric, as a function of the AdS disc radius r. The analytic approximation is $\Phi(r) = -\alpha(r^2+2\log(1-r^2))/2L^2$ with $\alpha = 64.3$ and $L = 1$. Energies are given in units of 4π.

3.6.2 The inter-soliton interaction

We can obtain a numerical approximation for the inter-soliton interaction in a similar way: we can numerically calculate the energy of a product ansatz of two translated $B = 1$ solitons, subtract off the potential energies associated with each component soliton (according to the numerical approximation above) and the energy of two $B = 1$ solutions, and plot the resulting energy as a function of the geodesic separation of the positions of the solitons.

These static approximations are shown as red curves in Figure 3.7, where the upper curve represents the inter-soliton energy of a pair of solitons in phase, and the lower curve represents solitons out of phase. Relative phase differences are calculated with respect to the geodesics that the particles lie on (see Fig 3.6), so that a pair of soliton fields with internal phases ψ_a and ψ_b have a relative phase difference $\chi = \chi(\psi_a, \psi_b)$. In keeping with results found in flat space [28], we find that pairs of solitons at large separations are in the maximally repulsive channel when they are in phase ($\chi = 0$), and in the maximally attractive channel when they are out of phase ($\chi = \pi$).

With this numerical data as a guide we can fit the out-of-phase interaction using a Morse potential of the form

$$U_\pi(\rho) = D\left(e^{2a(1-\rho/\rho_e)} - 2e^{a(1-\rho/\rho_e)}\right), \tag{3.6.4}$$

where ρ is the geodesic separation between the solitons, D is the depth of the potential at its minimum, ρ_e is the separation at which the potential is minimised, and a is a parameter controlling the width of the potential. These parameters can be fit by performing a least-squares fit with the numerical data. Since the product ansatz is only valid for well-separated solitons, we fit the data in the region where the separation between the solitons is greater than twice the size of a single soliton. This yields parameter values $D = 0.76$, $\rho_e = 0.73$ and $a = 1.13$.

In order to introduce a dependence of the potential on the relative phase difference of the two solitons, χ, we assume that the solitons are at their most attractive when they are out of phase, and their most repulsive when they are in phase i.e.

$$U_\chi(\rho) = D\left(e^{2a(1-\rho/\rho_e)} + 2\cos(\chi)e^{a(1-\rho/\rho_e)}\right). \tag{3.6.5}$$

Plots of U_0 and U_π are given by the upper and lower blue curves in Figure 3.7 respectively.

3.7 Baby Skyrmion rings and shells

We now seek energy minima of the point-particle approximation above for various values of B. For a configuration of B solitons with disc coordinates $\boldsymbol{x}_a$ and internal phases ψ_a (where $1 \leq a \leq B$) we seek to minimise the energy

$$E_B = \sum_{a=1}^{B}\left(\Phi(r_a) + \sum_{b>a} U_{\chi(\psi_a,\psi_b)}(d(\boldsymbol{x}_a,\boldsymbol{x}_b))\right), \tag{3.7.1}$$

where $r_a \equiv |\boldsymbol{x}_a|$, $\Phi(r)$ and $U_\chi(\rho)$ are the potentials given above and $d(\boldsymbol{x}_a,\boldsymbol{x}_b)$ is the geodesic distance (3.2.2) between points $\boldsymbol{x}_a$ and $\boldsymbol{x}_b$.

We minimise the point-particle energy using a multi-start stochastic hill-climbing method, where a randomly generated initial condition is allowed to relax iteratively.

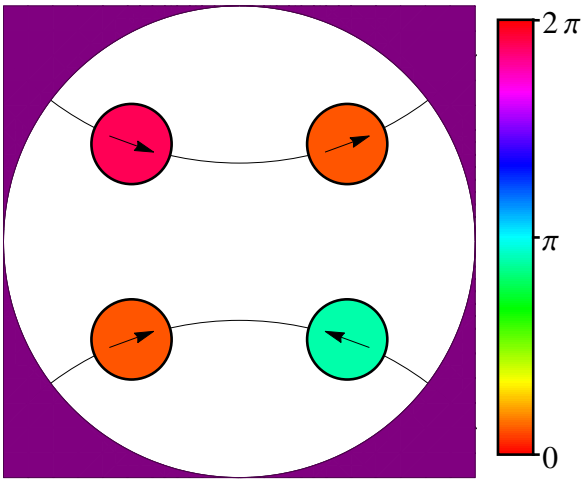

Figure 3.6: Diagram illustrating the geodesics connecting pairs of particles on the disc, with the top pair being in phase (the maximally repulsive channel) and the bottom pair being out of phase (the maximally attractive channel). Particles are coloured according to their internal phase, using the bar on the right.

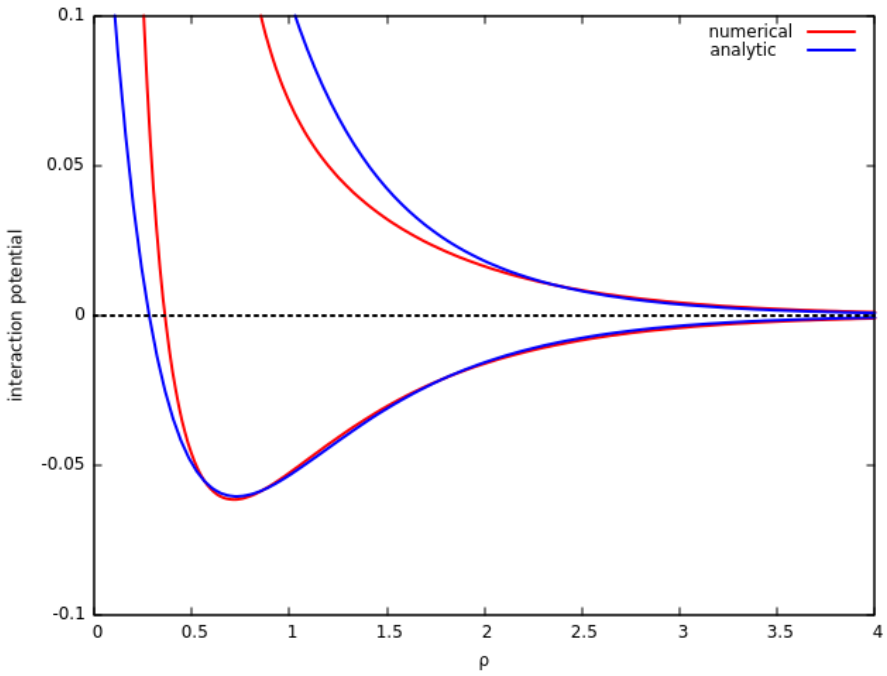

Figure 3.7: Numerical and analytic approximations for the inter-soliton interaction as a function of the geodesic separation ρ. The upper curves are the results for baby Skyrmions in phase, and the lower curves are for baby Skyrmions out of phase. The blue curves are given by the analytic Morse potential (3.6.5) with $D = 0.76$, $\rho_e = 0.73$ and $a = 1.13$. Energies are given in units of 4π.

For each topological charge we used randomly generated initial conditions, and the minimum energy configurations found are presented in Fig 3.8. Solutions were verified using a finite temperature annealing method. Particles are coloured according to their phases (see Fig 3.6).

We find that the point-particle approximation we have derived also favours configurations that form concentric ring-like structures. Furthermore, the qualitative forms of the energy minima predicted by the point-particle approximation are very close to the forms of the full numerical solutions found in Fig 3.3, although the results of the point-particle approximation are much more symmetric. This is to be expected since solitons in the full model have a finite size, and so can overlap and interact in more complicated ways.

For charges $B \leq 7$ the approximation accurately predicts not only the ring structure of the configurations, but also the alignment of internal phases. For even and odd charges the particles have internal phase differences of π and $\pi \pm \pi/B$ respectively, as observed in the full model. At $B = 8$ the approximation gives the correct distribution of phases, although it does not reproduce the deformed ring structure.

Furthermore, the point-particle approximation correctly captures the first popcorn transition at $B = 9$, and closely estimates the qualitative forms of the ring structures for all $B \leq 20$. The point-particle minima disagree with the full numerical results at charges $B = 11$, 13, 15, 16, 19 and 20. This may be due to the point-particle approximation not taking into consideration the radial forms of the $B = 2$ and 3 solitons, or may be a result of assuming the solitons can be approximated by particles with zero size. However, even when the exact forms do not agree, the difference is only by the position of a single particle.

These results suggest that the point-particle approximation may be a useful tool in qualitatively estimating the forms taken by AdS baby Skyrmions for higher charges. Performing further numerical minimisations of (3.7.1) allows us to predict a second popcorn transition at charge $B = 27$. In fact, by using the predicted forms as a guide for choosing initial conditions, full numerical energy minimisations reveal the popcorn transition to three layers around charge $B = 27$, 28, although it is difficult to say exactly when the transition occurs due to the presence of two local minima with

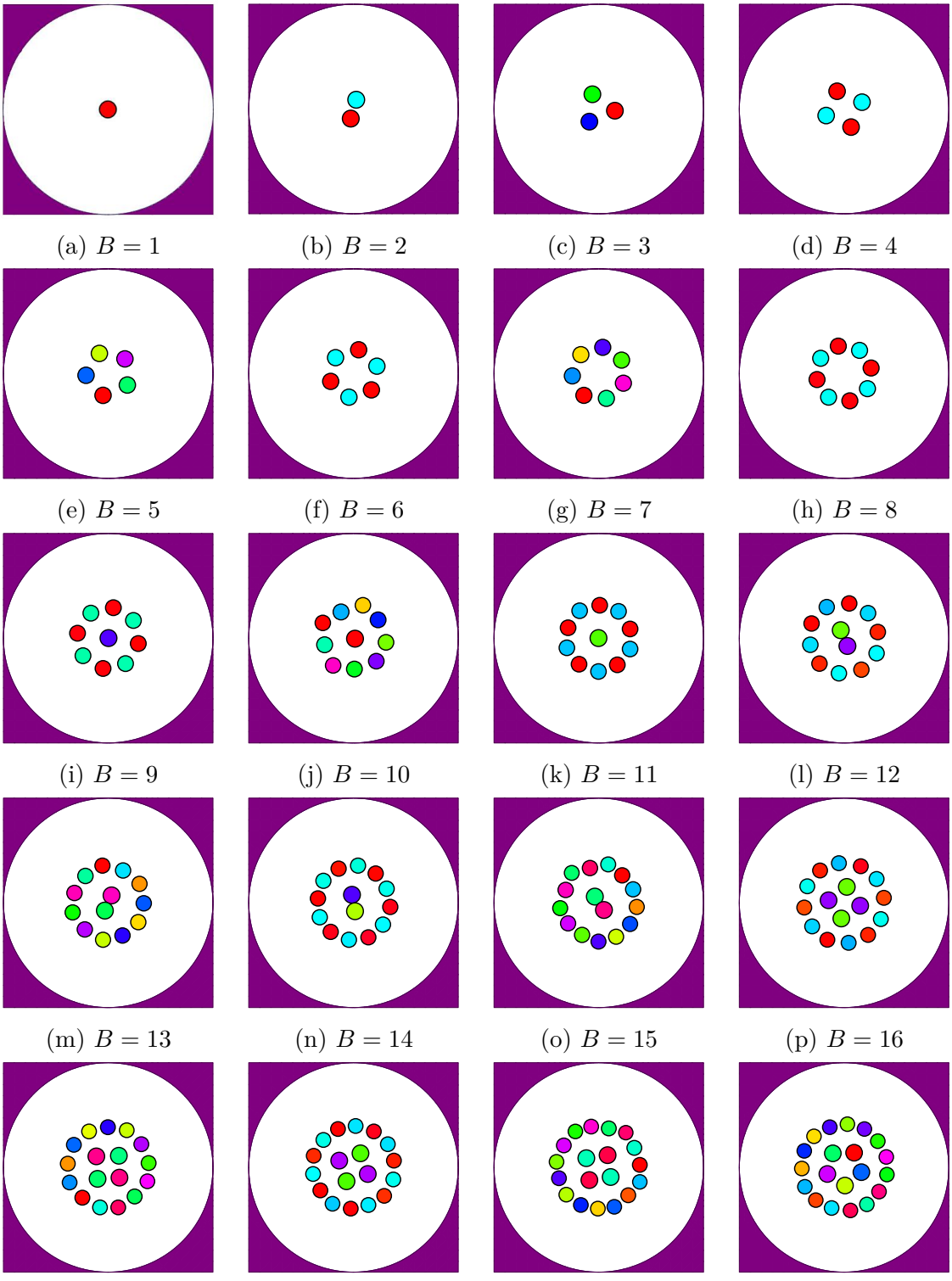

(a) $B = 1$ (b) $B = 2$ (c) $B = 3$ (d) $B = 4$

(e) $B = 5$ (f) $B = 6$ (g) $B = 7$ (h) $B = 8$

(i) $B = 9$ (j) $B = 10$ (k) $B = 11$ (l) $B = 12$

(m) $B = 13$ (n) $B = 14$ (o) $B = 15$ (p) $B = 16$

(q) $B = 17$ (r) $B = 18$ (s) $B = 19$ (t) $B = 20$

Figure 3.8: Minimal energy configurations for the point-particle approximation for topological charges $1 \leq B \leq 20$. Particles are coloured according to their internal phases (see Fig 3.6).

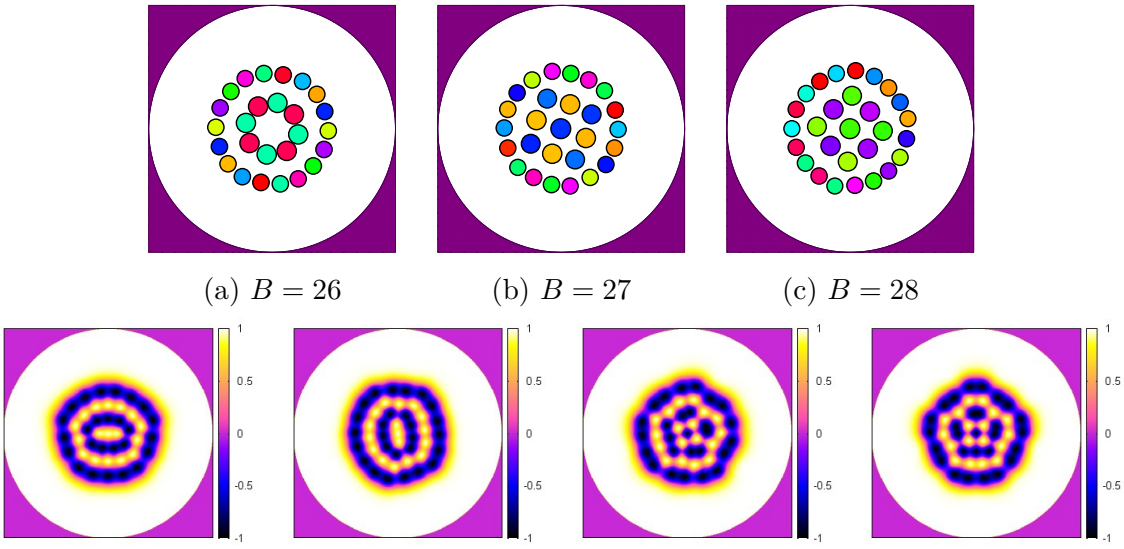

(a) $B = 26$ (b) $B = 27$ (c) $B = 28$

(d) $B = 26$ (e) $B = 27$ (f) $B = 27*$ (g) $B = 28$

Figure 3.9: The top row shows minimal energy configurations for the point-particle approximation for topological charges $26 \leq B \leq 28$. A popcorn transition to a three-layer solution is clearly seen at $B = 27$. This is confirmed by full numerical field calculations (below) which demonstrate a popcorn transition around $B = 27$, 28. At $B = 27$ two local minima with the same energy (to five significant figures) were found, indicated by the asterisk.

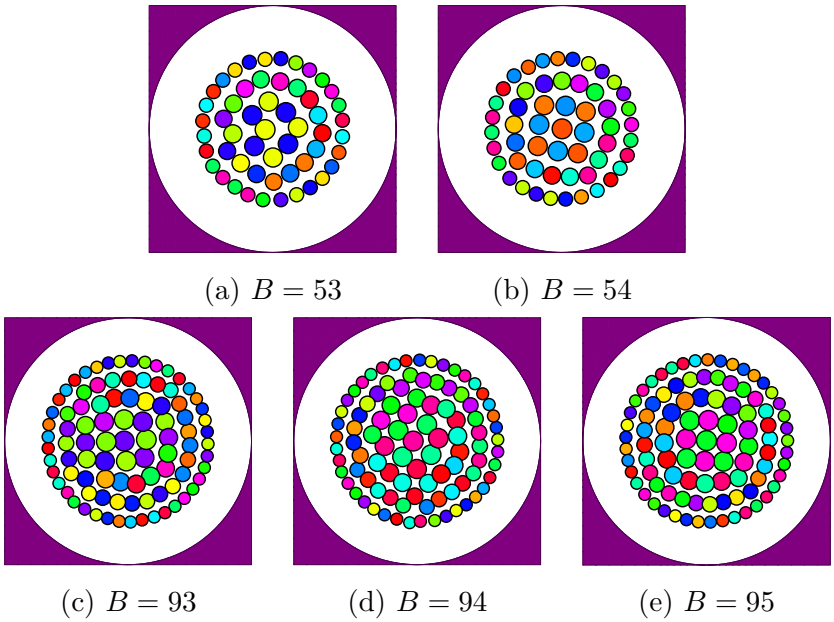

(a) $B = 53$ (b) $B = 54$

(c) $B = 93$ (d) $B = 94$ (e) $B = 95$

Figure 3.10: Minimal energy configurations of the point-particle approximation demonstrating popcorn transitions to four and five layers at charges $B = 54$ and $B = 95$ respectively. The lower charges pictured show how the inner-most ring of each configuration becomes deformed just before a pop.

charge B	$E/4\pi B$	form
26	1.8357	{9, 17}
27	1.8546	{9, 18}
27*	1.8546	{1, 9, 17}
28	1.8723	{1, 9, 18}

Table 3.2: Energies per soliton (in units of 4π) and forms for AdS baby Skyrmions with topological charge $26 \leq B \leq 28$. Two local minima of the same energy (to five significant figures) were found at $B = 27$, as indicated by the asterisk.

similar energies (shown in Fig 3.9, with energies given in Table 3.2).

The point-particle approximation predicts a third and fourth popcorn transition at charges $B = 54$ and $B = 95$ (see Fig 3.10). Since these charges are very large it would be difficult to perform an extensive search for the global minima in the full numerical model, even with the guidance provided by the point-particle approximation. However, the previous success of the model would indicate that the true popcorn transitions would, indeed, be near these points.

Finally, investigation of the results predicted by the point-particle approximation for still higher charges may be able to provide clues as to the lattice structure preferred by the baby Skyrmions in the infinite charge limit. The energy minimum for charge $B = 200$ and $B = 250$ can be seen in Fig 3.11. While clear rings can still be observed in the outermost layers, the centre of the configuration is heavily deformed and may indicate an emerging lattice structure.

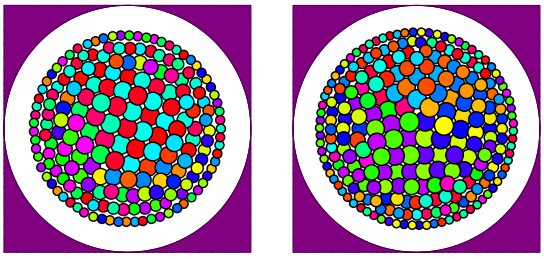

(a) $B = 200$ (b) $B = 250$

Figure 3.11: The minimal energy configuration of the point-particle approximation at charges $B = 200$ and 250. The ring structure near the origin is no longer clear, and may indicate the emergence of a lattice structure.

3.8 Conclusions

We have investigated the static solitons and multi-solitons of the massless baby Skyrme model in a $(2+1)$-dimensional anti de-Sitter spacetime. We have found that the spacetime curvature acts by adding an effective mass to the model which allows us to find static solutions to the equations of motion without a mass term. Solitons for topological charges $1 \leq B \leq 3$ were found to have a radially symmetric form, while higher-charge multi-solitons were found to form concentric ring-like solutions.

As B increases, a series of transitions occur where the minimal energy solutions take the form of concentric rings with increasing numbers of layers, a phenomenon reminiscent of the baryonic popcorn transitions studied recently in the context of dense holographic QCD. In order to investigate these transitions further a point-particle approximation was derived which was able to qualitatively estimate the forms of minimal energy solutions for a wide range of topological charges, as well as accurately predict the charges at which further popcorn transitions occur.

The point-particle approximation derived may indicate an emerging lattice structure for baby Skyrmions in AdS in the limit $B \to \infty$. The minimum energy configuration found for $B = 200$ and $B = 250$ displayed clear rings towards the edge of the space, although near the origin the structure appeared significantly less ring-like, and seemed suggestive of an emergent lattice formation. Further investigation into this area would be required to make any further claims.

The $O(3)$ sigma model stabilised by a baby Skyrme term has previously been studied in an AdS-like spacetime as a low-dimensional toy model of holographic QCD [62], specifically the Sakai-Sugimoto model. It has been argued that a better low-dimensional analogue of this model would involve stabilising an $O(3)$ sigma model using a vector meson term, and such a model has been studied in a parameter regime where the two toy models are similar [6], although investigation of a more interesting parameter regime proved difficult. It would therefore be interesting to study the vector meson model in pure AdS to see if a parameter regime could be found to give qualitatively different results to the baby Skyrme model.

Finally, the natural extension to this chapter is to study the full $(3+1)$-dimensional

Skyrme model in AdS. We have demonstrated that a multi-ring like structure exists in two dimensions for AdS baby Skyrmions and this property may translate to the higher dimensional model. This could manifest as spherical multi-shells with polyhedral symmetry groups and hence be approximated by multi-shell rational maps, and it would be interesting to study AdS Skyrmions to see if such configurations give lower energy solutions.

Chapter 4

Salty popcorn in a homogeneous low-dimensional toy model of holographic QCD

4.1 Introduction

In Chapter 2 we explored the idea of using low-dimensional toy models as analogues of the Sakai-Sugimoto model, especially in the context of high-density phenomena. However, studying the true Sakai-Sugimoto model is much more difficult than these toy models due to the increased analytical and numerical complexity of the problem. One way to circumvent this would be to make a spatially homogeneous approximation, motivated by expected results in a high-density regime, effectively reducing the dimensionality of the system.

One might worry that such an approximation might give rise to qualitatively different results. To test for this, we here develop a homogeneous ansatz in the low-dimensional toy model studied in [62]. We will find an ansatz of spatially dependent fields that gives rise to energy and baryon number densities that are homogeneous in the non-holographic direction. We find an ansatz that can only give solutions in the dyon salt phase, and find baryonic popcorn transitions within this sector, which we refer to as "salty popcorn". We analyse the behaviour of the model in the limiting cases of high

baryon number density and flat space, and find counter-intuitive scaling results. We also find that the homogeneous ansatz provides a good approximation to true solutions in the low-dimensional model by comparing the homogeneous solutions to full numerical calculations.

This chapter is based on my own work published in [8].

4.2 A homogeneous baby Skyrme model

The low-dimensional toy model of holographic QCD studied in [62] is written in terms of a three-component unit vector $\boldsymbol{\phi}(x,z)$ with spacetime metric (2.2.1) and energy and baryon number as given in (2.2.5) and (2.2.7). Our homogeneous ansatz will be to write:

$$\boldsymbol{\phi}(x,z) = \begin{cases} (\sin f(z)\cos(\pi\rho x), -\sin f(z)\sin(\pi\rho x), \cos f(z)) \ , & z \geq 0 \\ (\sin f(z)\cos(\pi\rho x), +\sin f(z)\sin(\pi\rho x), \cos f(z)) \ , & z \leq 0 \end{cases} \tag{4.2.1}$$

where $f(z)$ is some profile function dependent on the holographic coordinate and ρ is the baryon number density in the x-direction. The sign flip in the second component over $z = 0$ is to ensure the configuration has nonzero topological charge, and is related to the internal phases of the constituent solitons in the non-homogeneous model. The corresponding energy and soliton number (per unit length in the x-direction) are then

$$E = \int_0^\infty \left\{ \frac{\pi^2\rho^2}{H}\sin^2 f + H\,(f')^2 + \kappa^2\pi^2\rho^2\,(f')^2\sin^2 f \right\} \sqrt{H}\,dz\,, \tag{4.2.2}$$

$$\tilde{\rho} = -\frac{\rho}{2}\int_0^\infty f'\sin f\,dz\,. \tag{4.2.3}$$

We impose boundary conditions $f(0) = \pi$ and $f(\pm\infty) = 0$, which then imply the pion field satisfies $\boldsymbol{\phi}(x,0) = (0,0,-1)$ and $\boldsymbol{\phi}(x,\pm\infty) = (0,0,1)$. Since these field values in the baby Skyrme model correspond to the centre of a soliton and the vacuum respectively, we interpret our ansatz as a homogeneous line of soliton material located at $z = 0$. We interpret the soliton number per unit length $\tilde{\rho}$ as the baryon number density (in fact, with the boundary conditions on $f(z)$ we can identify $\tilde{\rho} \equiv \rho$).

We should note that this ansatz corresponds to the dyonic salt configuration, which is an analogue of the splitting of high-density calorons into monopole constituents with

half the topological charge. Here, the baryon number density is proportional to $\sin f$, and so vanishes at $z = 0$ and $z = \pm\infty$. The baryon number density must therefore be localised around two points away from the origin, rather than be localised around $z = 0$, which is characteristic of the splitting behaviour of the dyonic salt. This already leads to problems with the homogeneous ansatz, in that we cannot use it to predict whether a baryonic popcorn phase is preferred over a dyon salt phase at high densities. In fact, it can be shown that any field ansatz in the toy model periodic in x with boundary conditions $\boldsymbol{\phi}(x, 0) = (0, 0, -1)$ and $\boldsymbol{\phi}(x, \infty) = (0, 0, 1)$ must correspond to a salty ansatz (see Appendix B).

It is now a straightforward exercise to numerically compute the profile functions that minimise this energy using gradient flow methods. The equation of motion for the profile function is given by

$$\left(1 + \frac{\kappa^2\pi^2\rho^2}{H}\sin^2 f\right) f'' + \frac{z}{2H^2}\left(3 + \frac{\kappa^2\pi^2\rho^2}{H}\sin^2 f\right) f' - \frac{\pi^2\rho^2}{2H^2}\left(1 - H\kappa^2(f')^2\right)\sin 2f = 0\,, \tag{4.2.4}$$

although in practice it is convenient to transform the holographic direction onto the finite region $u \in [-\frac{\pi}{2}, \frac{\pi}{2}]$ via $z = \tan u$. Numerical solutions were obtained using a gradient flow algorithm on a grid of 1000 points, and the corresponding profile functions and soliton number densities for $\kappa = 0.01$ can be seen in Figure 4.1. By plotting the energy per soliton number as a function of the baryon number density ρ, as in Figure 4.2, we also see that the optimum density for the homogeneous single-layer is $\rho = 5.5$. This is roughly twice the optimal density in the holographic baby Skyrme model [62].

We observe that the width of the homogeneous layer decreases with increasing ρ, which is in agreement with the full numerical results in [62]. This, however, seems counter-intuitive as one would expect the width of the layer to increase with increasing ρ. This would allow the solitonic material to explore the holographic direction, which has been proposed as a holographic description of the quarkyonic phase [56] and chiral symmetry restoration [57].

To understand this effect we can look at limiting cases within the model. In the high-density, flat-space limit ($\rho \to \infty$, $H = 1$) the equation of motion for the profile function

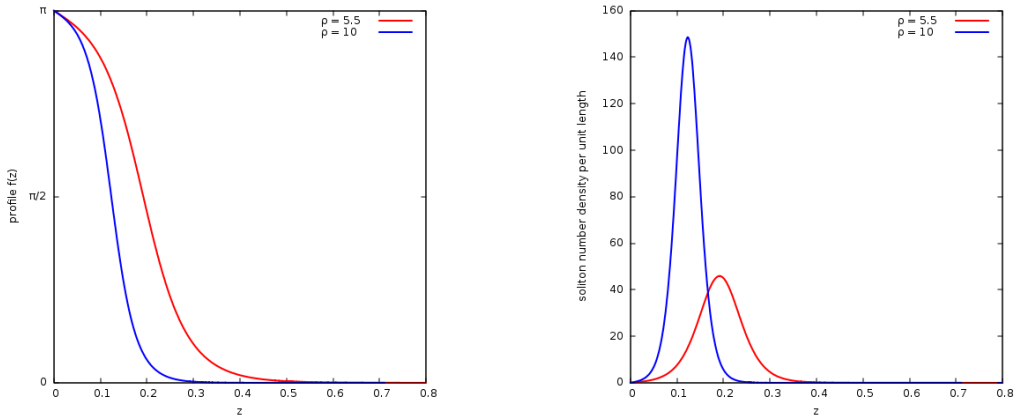

Figure 4.1: Plots of the numerically calculated single-layer profile functions (left) and soliton number densities (right) with $\kappa = 0.01$ in the homogeneous baby Skyrme model for baryon number densities $\rho = 5.5$ (red) and $\rho = 10$ (blue).

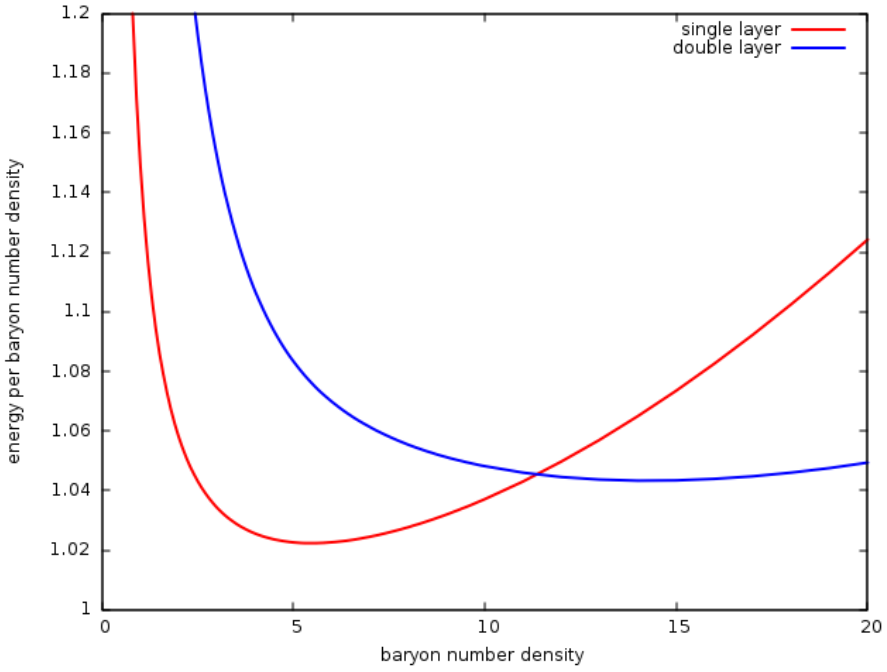

Figure 4.2: Energy per baryon number density (in units of 4π) as a function of baryon number density ρ for the single-layer (red) and double-layer (blue) configurations in the homogeneous baby Skyrme model with $\kappa = 0.01$.

reduces to

$$\kappa^2 \sin f f'' - (1 - \kappa^2 (f')^2) \cos f = 0 \,, \tag{4.2.5}$$

which has a compact solution

$$f(z) = \begin{cases} \pi - z/A \,, & 0 \leq z \leq A\pi \\ 0 & \text{otherwise} \end{cases} \tag{4.2.6}$$

when $A = \kappa$. Note here we have restricted to $z \geq 0$ and we extend to $z < 0$ by symmetry. We can now substitute an ansatz of the form (4.2.6) into the energy (4.2.2) and take the flat-space limit to obtain

$$E = \int_0^{A\pi} \left\{ \frac{1}{A^2} + \pi^2 \rho^2 \sin^2 \left(\pi - \frac{z}{A} \right) \left(1 + \frac{\kappa^2}{A^2} \right) \right\} dz \,, \tag{4.2.7}$$

$$= \frac{\pi}{2} \left(\pi^2 \rho^2 A + \frac{2 + \pi^2 \rho^2 \kappa^2}{A} \right) , \tag{4.2.8}$$

which is minimised by

$$A = \frac{\sqrt{2 + \pi^2 \rho^2 \kappa^2}}{\pi \rho} \,. \tag{4.2.9}$$

We note that $A \to \kappa$ as $\rho \to \infty$, which justifies the use of the compact ansatz. We also note that A decreases as ρ increases, explaining why the soliton size shrinks with increasing baryon number density.

To determine the region of validity of the compact ansatz we must determine when the flat-space approximation is applicable. The flat-space approximation should be valid when the size of the soliton is small compared to the curvature scale. In other words, we require the region on which the profile function is nonzero to be in $z \in [0, \varepsilon]$, where $\varepsilon \ll 1$. In the high-density limit this yields $\kappa\pi \ll 1$, which gives

$$\kappa \ll \frac{1}{\pi} \sim 0.3 \,. \tag{4.2.10}$$

We see then that a value of $\kappa = 0.01$ is within this regime. Figure 4.3 shows the profile function and associated soliton number density for $\rho = 100$ and 1000, and we see that the solution does indeed approach a compact form.

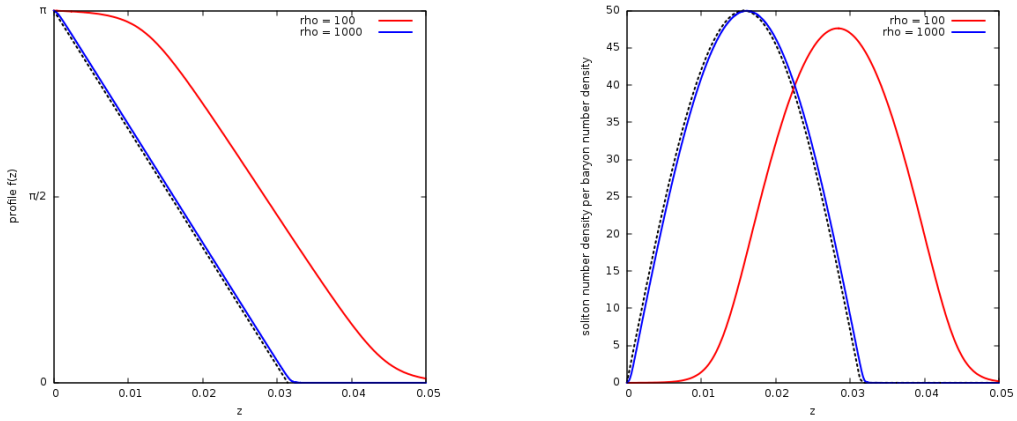

Figure 4.3: Plots of the numerically calculated single-layer profile functions (left) and soliton number densities (normalised by the baryon number density) (right) with $\kappa = 0.01$ in the homogeneous baby Skyrme model for very high baryon number densities $\rho = 100$ (red) and $\rho = 1000$ (blue). The black dotted lines show the associated high density compact solutions.

4.3 Baryonic popcorn in the homogeneous model

In order to investigate the presence of baryonic popcorn in this salty homogeneous model we must first generalise our single-layer ansatz to a multi-layer ansatz. One straightforward way to do this for a double-layer configuration, with layers localised around $z = \pm z_0$, is to patch together two single-layer solutions in a continuous manner:

$$\boldsymbol{\phi}(x,z) = \begin{cases} (\sin f(z)\cos(\pi\rho_1 x), -\sin f(z)\sin(\pi\rho_1 x), \cos f(z)) \ , & z_0 \leq z \\ (\sin f(z)\cos(\pi\rho_2 x), +\sin f(z)\sin(\pi\rho_2 x), \cos f(z)) \ , & 0 \leq z \leq z_0 \\ (\sin f(z)\cos(\pi\rho_2 x), -\sin f(z)\sin(\pi\rho_2 x), \cos f(z)) \ , & -z_0 \leq z \leq 0 \\ (\sin f(z)\cos(\pi\rho_1 x), +\sin f(z)\sin(\pi\rho_1 x), \cos f(z)) \ , & z \leq -z_0 \end{cases} \tag{4.3.1}$$

and requiring $f(0) = f(\pm\infty) = 0$ and $f(\pm z_0) = \pi$. We have introduced parameters ρ_1 and $\rho_2 \equiv \rho - \rho_1$ to allow topological charge to distribute itself between the components of the layers, and imposed symmetry in $z \to -z$ (up to the sign flip in the second component). Again, the repeated sign flips in the second components of the field are required to ensure nonzero topological charge. There is an additional sign flip in the first and second components of the pion field (equivalent to $f(z) \to -f(z)$) between $z > 0$ and $z < 0$, to ensure that the two layers are out of phase with each other, to

match results found in [62], although this has no overall effect on the calculations.

We should also note that, as in the single-layer case, the layers in this ansatz correspond to two layers of dyonic salt: the vanishing of the soliton number density at $z = \pm z_0$ implies that the soliton layers have already split into constituent half-layers. Again, this is a drawback since we cannot determine whether the dyon salt or the popcorn phase is preferred at high densities. Since we have found an analogue of the baryonic popcorn phase within a dyon salt ansatz, we refer to this phase as "salty popcorn".

With this salty popcorn ansatz we can now numerically solve for the profile function and density fraction ρ_1 at constant $\rho = \rho_1 + \rho_2$ and z_0 piecewise in each region using a gradient flow algorithm. We then minimise with respect to z_0 by performing a golden section search on these solutions. The resulting profile functions and soliton number densities are displayed in Figure 4.4.

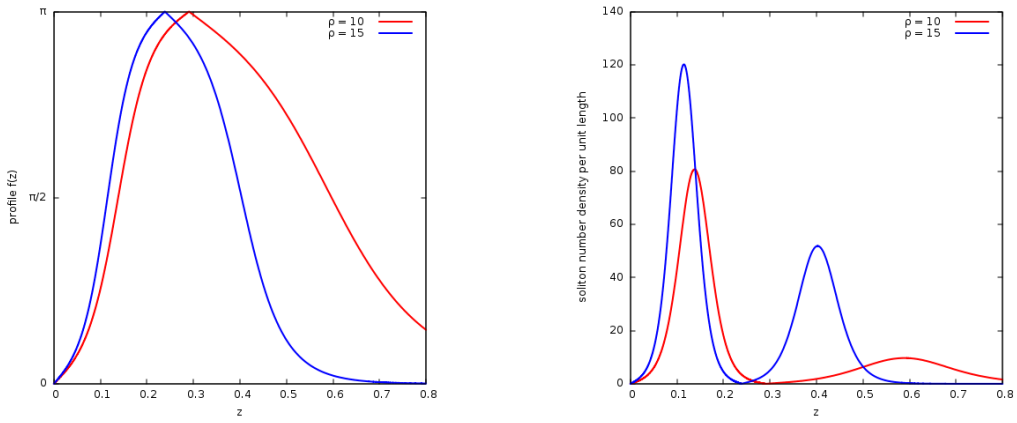

Figure 4.4: Plots of the numerically calculated double-layer profile functions (left) and soliton number densities (right) with $\kappa = 0.01$ in the homogeneous baby Skyrme model for baryon number densities $\rho = 10$ (red) and $\rho = 15$ (blue).

Again, we observe that the widths of the layers decrease with increasing ρ. In addition, we find that both the separation between the layers and the relative proportion of topological charge in the inner layer both decrease with increasing baryon number density ρ. We also notice that the solutions within the homogeneous ansatz become less smooth as ρ increases: this could be worrying as we would expect the ansatz to become more accurate (and hence more smooth) with increasing baryon number density. This can, once again, be explained by considering a compact solution in the high density, flat-space limit. Restricting to $z \geq 0$ (and extending to $z < 0$ using

symmetry), the ansatz

$$f(z) = \begin{cases} \pi z/z_0\,, & 0 \le z \le z_0 \\ \pi(A-z)/(A-z_0)\,, & z_0 \le z \le A \\ 0 & \text{otherwise} \end{cases} \tag{4.3.2}$$

again satisfies the equations of motion in the high density limit so long as $z_0 \to \pi\kappa$ and $(A - z_0) \to \pi\kappa$ as $\rho_1, \rho_2 \to \infty$. Substituting this ansatz into the energy (4.2.2) and taking the flat-space limit yields

$$\begin{aligned} E &= \int_0^{z_0} \left\{ \frac{\pi^2}{z_0^2} + \pi^2\rho_1^2 \sin^2\left(\frac{\pi z}{z_0}\right)\left(1 + \frac{\kappa^2\pi^2\rho_1^2}{z_0^2}\right)\right\} dz \\ &\quad + \int_{z_0}^{A} \left\{ \frac{\pi^2}{(A-z_0)^2} + \pi^2\rho_2^2 \sin^2\left(\frac{\pi(A-z)}{A-z_0}\right)\left(1 + \frac{\kappa^2\pi^2\rho_2^2}{(A-z_0)^2}\right)\right\} dz \\ &= \frac{\pi^2}{2}\left(\rho_1^2 z_0 + \frac{2+\kappa^2\pi^2\rho_1^2}{z_0} - \rho_2^2(A-z_0) - \frac{2+\kappa^2\pi^2\rho_2^2}{A-z_0}\right). \end{aligned} \tag{4.3.3}$$

Minimising with respect to z_0, A and ρ_1 yields

$$\rho_1 = \rho_2 = \rho/2\,, \tag{4.3.4}$$

$$z_0 = \frac{\sqrt{8+\kappa^2\pi^2\rho^2}}{\rho}\,, \tag{4.3.5}$$

$$A = 2z_0\,. \tag{4.3.6}$$

We note that $z_0 \to \pi\kappa$ and $(A - z_0) \to \pi\kappa$ as $\rho \to \infty$, justifying the use of the compact ansatz. We also see that we require $A = 2z_0 \to 2\pi\kappa \ll 1$ for the flat-space ansatz to be valid, yielding $\kappa \ll 1/(2\pi) \sim 0.16$.

We find that the high density limit of the double-layer solution takes the form of two equal sized layers with baryon number density distributed equally among them. This limiting behaviour can be confirmed by numerically solving (4.2.4) for the double-layer case for very high densities. Figure 4.5 shows the profile functions and soliton number densities for such solutions with $\kappa = 0.01$ and baryon number densities $\rho = 200$ and $\rho = 2000$. The existence of the compact solution also explains the breakdown of smoothness of the ansatz at higher densities, since the compact limit does not yield a smooth solution.

Finally, we do observe a popcorn transition in this homogeneous model. By comparing

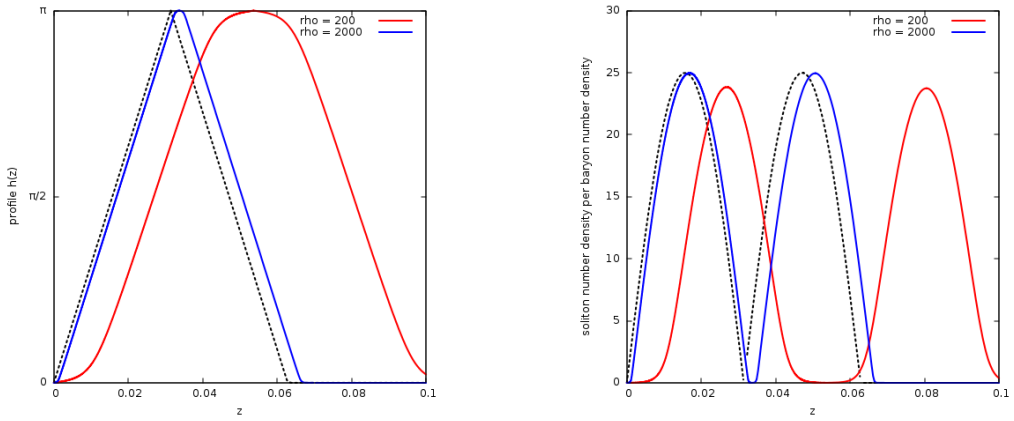

Figure 4.5: Plots of the numerically calculated double-layer profile functions (left) and soliton number densities (normalised by the baryon number density) (right) with $\kappa = 0.01$ in the homogeneous baby Skyrme model for very high baryon number densities $\rho = 200$ (red) and $\rho = 2000$ (blue). The black dotted lines show the associated high density compact solutions.

the energy per baryon number density of the single- and double-layer configurations in Figure 4.2 we can clearly see a transition point around $\rho = 11.4$ beyond which the double-layer configurations become energetically favourable compared to the single-layer configurations. This, again, is roughly twice the density at which the first popcorn transition is observed in the non-homogeneous baby Skyrme model. We can also see that such a popcorn transition must occur by looking at the high density compact solutions: we have

$$E_{\text{single}} = \pi^2 \rho \sqrt{2 + \pi^2 \kappa^2 \rho^2}\,, \tag{4.3.7}$$

$$E_{\text{double}} = \frac{\pi^2 \rho}{2} \sqrt{8 + \pi^2 \kappa^2 \rho^2}\,, \tag{4.3.8}$$

and so we see that $E_{\text{double}} \to E_{\text{single}}/2$ as $\rho \to \infty$.

4.4 Comparison with full numerical solutions

The advantage of the two-dimensional toy model is that we can actually compare the predictions made by the homogeneous ansatz to numerical solutions obtained in the full model. In [62] full numerical periodic solutions in the holographic baby Skyrme model were found for a range of baryon densities, with boundary conditions used to specify different numbers of layers. An analogue of the dyon salt phase was found, manifest by

single-layer solutions becoming more homogeneous with increasing density. In addition, double- and triple-layer configurations were found to be energetically favourable beyond some critical densities, demonstrating popcorn transitions. Crucially, these popcorn transitions occurred at densities well below the analogues of the dyon salt. It was conjectured that further popcorn transitions beyond three layers would also occur.

Figure 4.6 shows the pion field ϕ_3 for both the homogeneous ansatz and the full numerical solution for single-layer configurations at densities $\rho = 5$ and $\rho = 10$, and Figure 4.7 shows the same information for double-layer configurations at densities $\rho = 10$ and $\rho = 50$. In each case, numerical computations were performed on a grid containing one unit of topological charge per layer and periodic boundary conditions on ϕ_3. Anti-periodic boundary conditions on ϕ_1 and ϕ_2 were imposed to ensure solutions took the form of either a single chain or a regular square chain respectively (as in the multi-layer computations in Chapter 2). The plots themselves show more units of topological charge, for the sake of clarity.

In both cases we find the qualitative appearances of the solutions to be very similar for higher densities. We also calculate the energies of the different solutions (displayed in Table 4.1) and find them to also be in close agreement at higher densities.

We also notice that, for the double-layer configurations, the homogeneous ansatz predicts the layers to be more widely separated, even for higher densities. This could be because the homogeneous ansatz does not allow the separate layers to interact, as the ansatz forces the fields to take the vacuum value on the line $z = 0$. In the full numerical solutions the separate layers are out of phase with each other, causing an attraction between them, and the homogeneous ansatz cannot capture this feature. Whether this difference can be resolved or not is still an open problem.

4.5 Multi-layer solutions and popcorn transitions

We can use our flat-space compact approximations to shows the existence of further popcorn transitions in this model beyond two layers. For simplicity we will consider an N-layer solution for N odd, although this can be easily generalised for N even. Restricting to $z \geq 0$ we construct a multi-layer ansatz with soliton layers localised

density ρ	single-layer $E/(4\pi\rho)$		double-layer $E/(4\pi\rho)$	
	homogeneous	numerical	homogeneous	numerical
5	1.023	1.012	1.088	1.013
10	1.037	1.034	1.048	1.021
50	1.608	1.608	1.189	1.187

Table 4.1: Energies per baryon number density (in units of 4π) for single- and double-layer solutions, both within the homogeneous ansatz and from full numerical computations.

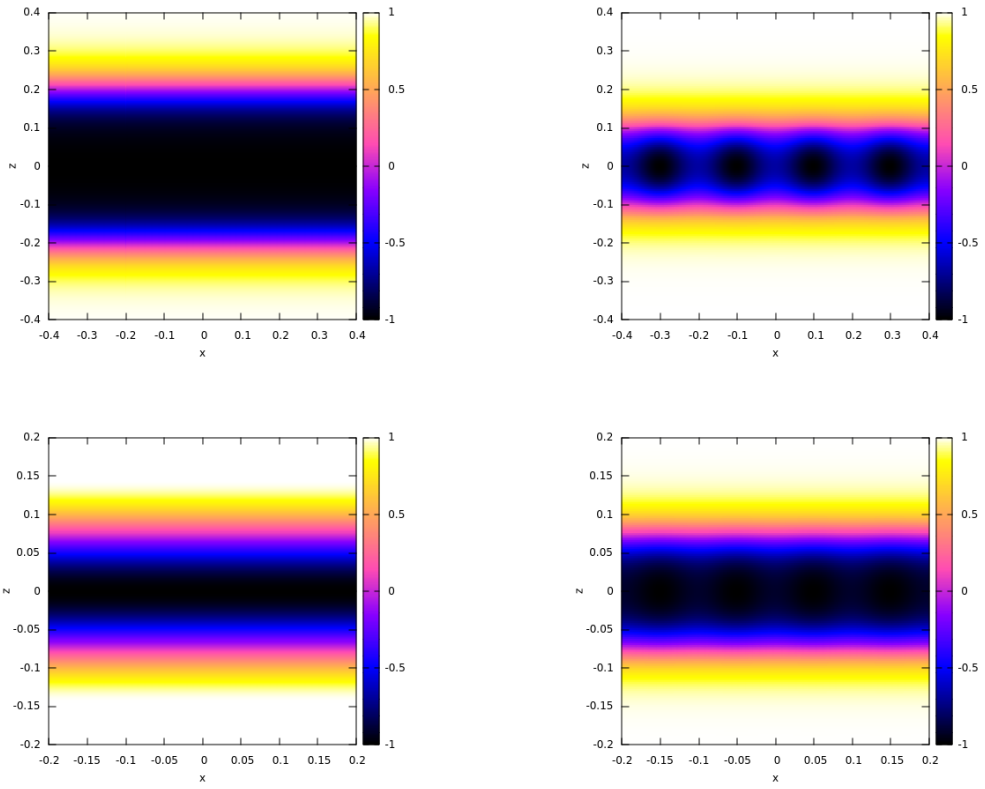

Figure 4.6: The third component of the pion field ϕ_3 for the single-layer configurations within the homogeneous ansatz (left) and from full numerical computations (right). Each plot shows four units of topological charge. The solutions are calculated at densities $\rho = 5$ (top) and $\rho = 10$ (bottom). We see that the homogeneous approximation is reasonable for moderately high densities.

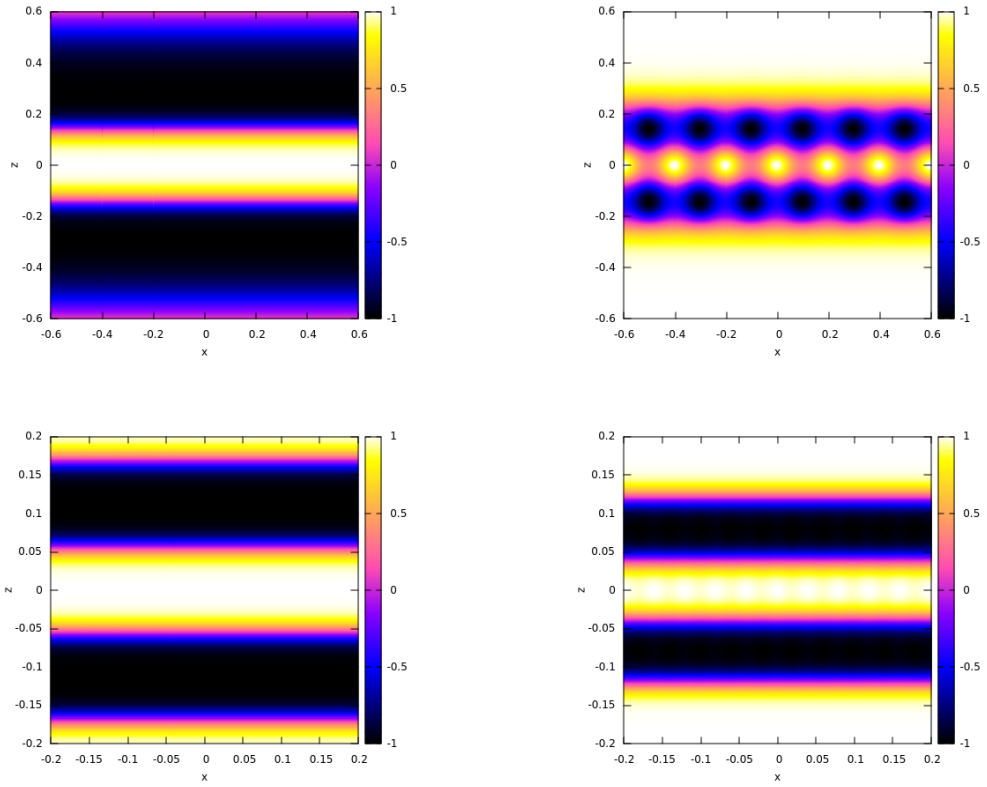

Figure 4.7: The third component of the pion field ϕ_3 for the double-layer configurations within the homogeneous ansatz (left) and from full numerical computations (right). The solutions are calculated at densities $\rho = 10$ (top, 12 units of topological charge displayed) and $\rho = 50$ (bottom, 20 units of topological charge displayed). We see that the homogeneous approximation is reasonable for moderately high densities.

around the positions $z \in \{z_0 = 0, z_1, \ldots, z_{(N-1)/2}\}$ by piecewise gluing together compact solutions of the form above. Explicitly we write

$$f(z) = \begin{cases} \pi(A_n - z)/(A_n - z_n)\,, & z_n \leq z \leq A_n \\ \pi(z - A_n)/(z_{n+1} - A_n)\,, & A_n \leq z \leq z_{n+1} \\ 0 & \text{otherwise} \end{cases}, \tag{4.5.1}$$

where $0 \leq n \leq (N-1)/2$ and $z_n < A_n < z_{n+1}$. This ensures $f(z_n) = \pi$ and $f(A_n) = 0$. This ansatz can then be substituted into the energy (4.2.2), which can be integrated in the flat-space limit to obtain

$$E = \sum_{k=0}^{N-1} E_k\,, \tag{4.5.2}$$

where we denote the partial energies as

$$E_{2k} = \frac{\pi^2}{2}\left((A_k - z_k)\rho_{2k}^2 + \frac{2 + \kappa^2\pi^2\rho_{2k}^2}{A_k - z_k}\right), \qquad 0 \leq k \leq (N-1)/2 \tag{4.5.3}$$

$$E_{2k+1} = \frac{\pi^2}{2}\left((z_{k+1} - A_k)\rho_{2k+1}^2 + \frac{2 + \kappa^2\pi^2\rho_{2k+1}^2}{z_{k+1} - A_k}\right), \qquad 0 \leq k \leq (N-3)/2 \tag{4.5.4}$$

and ρ_k are the partial baryon number densities satisfying $\rho = \sum_{k=0}^{N-1} \rho_k$.

We can now minimise with respect to z_n and A_n to obtain

$$A_k - z_k = \frac{\sqrt{2 + \kappa^2\pi^2\rho_{2k}^2}}{\rho_{2k}}\,, \qquad 0 \leq k \leq (N-1)/2 \tag{4.5.5}$$

$$z_{k+1} - A_k = \frac{\sqrt{2 + \kappa^2\pi^2\rho_{2k+1}^2}}{\rho_{2k+1}}\,, \qquad 0 \leq k \leq (N-3)/2 \tag{4.5.6}$$

$$E_k = \pi^2\rho_k\sqrt{2 + \kappa^2\pi^2\rho_k^2}\,, \qquad 0 \leq k \leq N-1 \tag{4.5.7}$$

Further minimising with respect to ρ_k yields $\rho_k = \rho/N$ and we find that, within this ansatz, the baryon number density of each layer component is equal. This then gives us

$$A_k - z_k = z_{k+1} - A_k = \frac{\sqrt{2N^2 + \kappa^2\pi^2\rho^2}}{\rho}\,, \tag{4.5.8}$$

$$E = \sum_{k=0}^{N-1} E_k = \frac{\pi^2\rho}{N}\sqrt{2N^2 + \kappa^2\pi^2\rho^2}\,, \tag{4.5.9}$$

and we see that the widths of each layer component are also all equal, tending to $\kappa\pi$ as

$\rho \to \infty$. As above, this implies that this ansatz solves the flat-space equation of motion in the high density limit. The flat-space approximation is valid when $N\kappa\pi \ll 1$, which for our value of $\kappa = 0.01$ gives $N \ll 1/(0.01\pi) \sim 32$. We can also see that, as long as the flat-space approximation is valid, the N-layer solution will always be preferable in the high density limit: we have $E_{\text{N-layer}} \to E_{\text{single}}/N$ as $\rho \to \infty$.

The analysis above is only valid when the flat-space approximation is legitimate; beyond this regime the effect of curved space would need to be taken into account. This is difficult both numerically and analytically due to the large number of extra parameters we have introduced. We can, however, construct an ansatz for three layers subject to further approximations, and deduce the existence of further popcorn transitions.

Using simpler notation than the multi-layer analysis above, we construct a three-layer ansatz by introducing parameters $z_1 > z_0$ and imposing $f(0) = f(\pm z_1) = \pi$ and $f(\pm z_0) = f(\pm\infty) = 0$ (with appropriate sign flips in the second components of the associated $\boldsymbol{\phi}$ fields). Numerically minimising with respect to all of these parameters, in addition to the partial baryon number densities in each layer component, is challenging. Instead, we assume the baryon number density is equally spread across the configuration (by setting all the partial baryon number densities equal to $\rho/3$) and then minimise with respect to z_1 for a range of fixed z_0. By doing this we can clearly see that for high densities, there will be a three-layer solution that is energetically preferable when compared to the double-layer (see Figure 4.8). When combining this result with the above analysis it would seem reasonable to conjecture further popcorn transitions will occur to four or more layers as density increases even further, as conjectured in the non-homogeneous holographic baby Skyrme model [62]. One would, however, expect the curvature of spacetime to become more relevant as the number of layers increases, and the effect of this on the number of popcorn transitions is currently unknown.

4.6 Conclusions

We have successfully employed a homogeneous ansatz which has reproduced some of the qualitative behaviour of the full holographic baby Skyrme model. We find a series

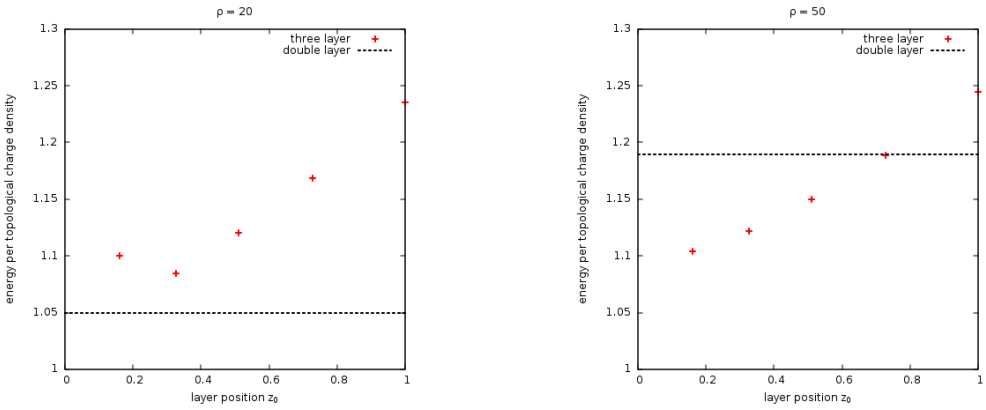

Figure 4.8: Energy per baryon number density (in units of 4π) as a function of layer position z_0 for $\rho = 20$ (left) and $\rho = 50$ (right) in the homogeneous baby Skyrme model with $\kappa = 0.01$. The black dotted lines show the corresponding double-layer energies at these densities, and the energies of the three-layer configurations are given by red +'s.

of single-layer configurations, with an optimal density and a popcorn transition (albeit a salty one) to a double-layer configuration at roughly twice the true numerically calculated densities. We also find evidence for a second popcorn transition in this model, qualitatively matching the full numerical results previously studied. These successes demonstrate that a homogeneous ansatz can be a useful tool for studying cold, dense QCD. In fact, in Chapter 5 we shall employ homogeneous ansätze in the five-dimensional Sakai-Sugimoto model, and discover a new alternative to the previously mentioned dyon salt and baryonic popcorn configurations for high baryon density.

Unfortunately the ansatz falls short in that it can only generate solutions that are already in the dyon salt phase. This prevents making any comparisons between the energy of this phase with the energy of the baryonic popcorn phase. In fact, we have shown that imposing any homogeneity in this toy model via periodic fields will always have this problem. When we develop the homogeneous ansätze for the five-dimensional Sakai-Sugimoto model in Chapter 5 we shall find one ansatz that also shares a similar problem to this. However, the properties of the higher-dimensional model will enable us to find a different ansatz that is much more satisfying, and gives rise to interesting new results. This different ansatz will then reveal key differences between the five-dimensional model and the low-dimensional toy models.

Chapter 5

Homogeneous approximations of the Sakai-Sugimoto model

5.1 Introduction

To simplify the problem of studying the Sakai-Sugimoto model at high baryon number density one can assume spatial homogeneity in the non-holographic directions, reducing calculations to an effective one-dimensional problem. This approximation is justified by the studies of low-dimensional toy models, as in Chapter 4, in which the homogeneous approximation was found to qualitatively reproduce results from full numerical calculations.

In the higher-dimensional case it is easy to show that there are no smooth, spatially homogeneous gauge potentials with non-zero baryon number density and finite energy. One way to circumvent this, as in [58], is to impose homogeneity using singular gauge fields. This reduces the problem to the calculation of a single profile function dependent only on the holographic coordinate. Another approach is to replace the Euclidean spatial volume with a three-sphere [71], since then there are smooth, finite energy, spatially homogeneous gauge potentials whose finite baryon number density can be varied by changing the radius of the three-sphere.

In this chapter we begin by briefly discussing the singular configurations first introduced in [58], before introducing a new homogeneous approximation that can be viewed as a

hybrid of the two approaches mentioned above. We introduce homogeneity at the level of the field strength, rather than the gauge potential, in such a way that produces an expression for the field strength that is similar to that obtained on the three-sphere. However, where the study in [71] fixed dependence on the holographic direction by imposing self-duality conditions, here we will retain the arbitrary dependence on the holographic direction, leading us to an effective kink theory in the holographic direction. This kink theory demonstrates a first-order transition to lightly bound nuclear matter, as in QCD, and can be interpreted as a smeared crystal. We also expect the energy of the smeared crystal to provide a lower bound on the energy of the true soliton crystal, and justify this by analysing the simpler case of the Skyrme crystal (see Appendix C).

We will look for analogues of both the dyon salt and baryonic popcorn configurations in these homogeneous models. In our study of the singular model we only find analogues of the baryonic popcorn phase, while in the homogeneous kink model we find not only that there are analogues of the dyon salt and baryonic popcorn, but also that at high densities the popcorn phase is energetically preferred over the dyon salt, a result that was found when studying low-dimensional toy models [62, 6] based on sigma model instantons. We also find that the kink model predicts only one pop, rather than an infinite sequence of pops, and explain all the results in the kink model by analysing the form of the potential term in the effective Lagrangian.

We also find that the double-layer configurations in the kink model form the surface of a soliton bag that increases in size with increasing density. The interior of the bag is filled with abelian electric potential, and the instanton charge density is localised on the surface of the bag. This is similar to the magnetic bags [72] that approximate coincident non-abelian BPS monopoles, where the role of the abelian electric potential is played by the modulus of the Higgs field. It is, however, qualitatively different from the instanton bag proposed in [73], where monopole walls are embedded into the Sakai-Sugimoto model to produce a bag where the instanton charge density fills the interior, instead of being localised on the surface of the bag.

This chapter is based on collaborative work published in [9].

5.2 The Sakai-Sugimoto model

As previously mentioned (see Section 1.5), the Sakai-Sugimoto model is a candidate model for holographic QCD where, in its low energy description, solitons in a $(4+1)$-dimensional bulk correspond to baryons. This low energy model has a curved, "AdS-like" spacetime given by the metric

$$ds^2 = H(z)dx_\mu dx^\mu + \frac{1}{H(z)}dz^2\,, \tag{5.2.1}$$

where z is the holographic direction and we have used the $(-,+,+,+,+)$ metric signature. The warp factor $H(z)$ is given by

$$H(z) = \left(1+z^2\right)^{2/3}\,. \tag{5.2.2}$$

The static energy within this effective model is written in terms of an $SU(2)$ gauge field A_I and an abelian electric potential $\hat{A}_0$ as

$$\begin{aligned} E = \frac{1}{2}\int\Bigg\{ &-\frac{1}{H^{1/2}}\left(\partial_i\hat{A}_0\right)^2 - H^{3/2}\left(\partial_z\hat{A}_0\right)^2 \\ &+\frac{1}{H^{1/2}}\mathrm{Tr}\left(F_{ij}F_{ij}\right) + 2H^{3/2}\mathrm{Tr}\left(F_{iz}F_{iz}\right) \\ &+\frac{8}{\Lambda}\hat{A}_0\varepsilon_{ijk}\mathrm{Tr}\left(F_{iz}F_{jk}\right)\Bigg\}d^3\boldsymbol{x}dz\,. \end{aligned} \tag{5.2.3}$$

Upper case Latin letters $I, J, \ldots$ denote all four spatial directions, and lower case Latin letters $i, j, \ldots$ denote the three non-holographic spatial directions. The constant parameter $\Lambda = 8\lambda/27\pi$ is the rescaled 't Hooft coupling.

The high dimensionality of the Sakai-Sugimoto model makes numerical calculations within it very difficult, so we now seek a homogeneous ansatz to reduce the field equations to ODEs.

5.3 The singular ansatz: homogeneous gauge fields

Our first homogeneous ansatz is for a single layer of solitons at $z = 0$, and introduces the homogeneity at the level of the gauge fields. This ansatz is, arguably, less effective than the kink ansatz we will see later, and for this reason we will only perform a detailed

enough analysis in this subsection to reveal some key elements to be compared with the later ansatz.

The singular ansatz is given by

$$\begin{aligned} \hat{A}_0 = \omega(z)\,, \quad A_i = -\frac{\alpha}{2}h(z)\sigma_i\,, \qquad & A_z = 0\,, \\ F_{ij} = -\frac{\alpha^2}{2}h(z)^2\varepsilon_{ijk}\sigma_k\,, \quad & F_{iz} = \frac{\alpha}{2}h(z)'\sigma_i\,. \end{aligned} \tag{5.3.1}$$

The boundary conditions on the profile functions are $\lim_{z\to 0^\pm} h(z) = \pm 1$ and $h(\pm\infty) = 0$. The discontinuity of $h(z)$ at $z = 0$ is required for the topology of the soliton solutions to be nontrivial.

The constant α is fixed by calculating the baryon number density (i.e. the instanton number per spatial 3-volume V):

$$\rho \equiv \frac{N}{V} = -\frac{\alpha^3}{8\pi^2}\int_{-\infty}^{\infty}\left(h^3\right)'\,dz = -\frac{\alpha^3}{4\pi^2}\int_0^{\infty}\left(h^3\right)'\,dz = \frac{\alpha^3}{4\pi^2}\,. \tag{5.3.2}$$

For the analysis of the singular ansatz we shall work in the canonical ensemble (i.e. work at fixed baryon number density ρ, with zero chemical potential), giving boundary conditions on the abelian electric potential $\omega(z)$ as $\omega(\pm\infty) = 0$. This is because, in holographic QCD, the boundary value of the abelian electric potential is proportional to the chemical potential [74, 75]. We also impose symmetries that $h(z)$ and $\omega(z)$ are odd and even functions of z respectively, since we expect the energy minimising bulk solutions to have instanton number density and abelian electric potential that are even functions of z localised around $z = 0$.

In the following calculations we shall work in the domain $z \geq 0$ and extend to $z < 0$ using symmetry. The static energy per 3-volume for this ansatz is

$$\mathcal{E} \equiv \frac{E}{V} = \mathcal{E}_{YM} + \mathcal{E}_{CS}\,, \tag{5.3.3}$$

where

$$\mathcal{E}_{YM} = \int_0^{\infty}\left\{3\alpha^2 H^{3/2}\left(h'\right)^2 + \frac{3\alpha^4}{H^{1/2}}h^4 - H^{3/2}\left(\omega'\right)^2\right\}\,dz\,, \tag{5.3.4}$$

$$\mathcal{E}_{CS} = \int_0^{\infty}\left\{-\frac{8\alpha^3}{\Lambda}\omega\left(h^3\right)'\right\}\,dz\,. \tag{5.3.5}$$

The equations of motion for $\omega(z)$ and $h(z)$ are

$$\delta\omega : \qquad \left(H^{3/2}\omega'\right)' = \frac{4\alpha^3}{\Lambda}\left(h^3\right)' , \tag{5.3.6}$$

$$\Rightarrow \qquad H^{3/2}\omega' = \frac{4\alpha^3}{\Lambda}\left(h^3 - c_1\right) , \tag{5.3.7}$$

$$\delta h : \qquad \left(H^{3/2}h'\right)' = \frac{2\alpha^2}{H^{1/2}}h^3 + \frac{4\alpha}{\Lambda}h^2\omega' = \frac{2\alpha^2}{H^{1/2}}h^3 + \frac{16\alpha^4}{\Lambda^2 H^{3/2}}h^2\left(h^3 - c_1\right) , \tag{5.3.8}$$

where c_1 is an integration constant to be fixed. We can now see the leading-order decay behaviour of the profile function $h(z)$: for large z the equation of motion gives

$$z^2h'' + 2zh' = 0 \Rightarrow h(z) \sim \frac{1}{z} . \tag{5.3.9}$$

We can now eliminate the abelian electric potential, ω, from integrals (5.3.4) and (5.3.5). First note that we can substitute (5.3.7) directly into (5.3.4) to obtain

$$\mathcal{E}_{YM} = \int_0^\infty \left\{ 3\alpha^2 H^{3/2}\left(h'\right)^2 + \frac{3\alpha^4}{H^{1/2}}h^4 - \frac{16\alpha^6}{\Lambda^2 H^{3/2}}(h^3 - c_1)^2 \right\} dz . \tag{5.3.10}$$

Next, we multiply (5.3.6) by ω to get

$$\frac{4\alpha^3}{\Lambda}\left(h^3\right)'\omega = \left(H^{3/2}\omega'\omega\right)' - H^{3/2}\left(\omega'\right)^2 , \tag{5.3.11}$$

and substitute into (5.3.5) to obtain

$$\begin{aligned} \mathcal{E}_{CS} &= \int_0^\infty \left\{ \frac{32\alpha^6}{\Lambda^2 H^{3/2}}\left(h^3 - c_1\right)^2 \right\} dz - \left[2H^{3/2}\omega'\omega\right]_0^\infty \\ &= \int_0^\infty \left\{ \frac{32\alpha^6}{\Lambda^2 H^{3/2}}\left(h^3 - c_1\right)^2 \right\} dz + \frac{8\alpha^3}{\Lambda}(1 - c_1)\omega(0) , \end{aligned} \tag{5.3.12}$$

where we have used $\omega'(0) = 4\alpha^3(1 - c_1)/\Lambda$ from (5.3.7). This yields the final energy expression:

$$\mathcal{E} = \int_0^\infty \left\{ 3\alpha^2 H^{3/2}\left(h'\right)^2 + \frac{3\alpha^4}{H^{1/2}}h^4 + \frac{16\alpha^6}{\Lambda^2 H^{3/2}}\left(h^3 - c_1\right)^2 \right\} dz + \frac{8\alpha^3}{\Lambda}(1 - c_1)\omega(0) . \tag{5.3.13}$$

The variation of the integral part of this energy reproduces the equation of motion (5.3.8), so we can now fix $c_1 = 1$ to ensure the constant piece vanishes.

Notice that this value for c_1 in (5.3.7) then implies that $\omega'(0) = 0$, meaning that even

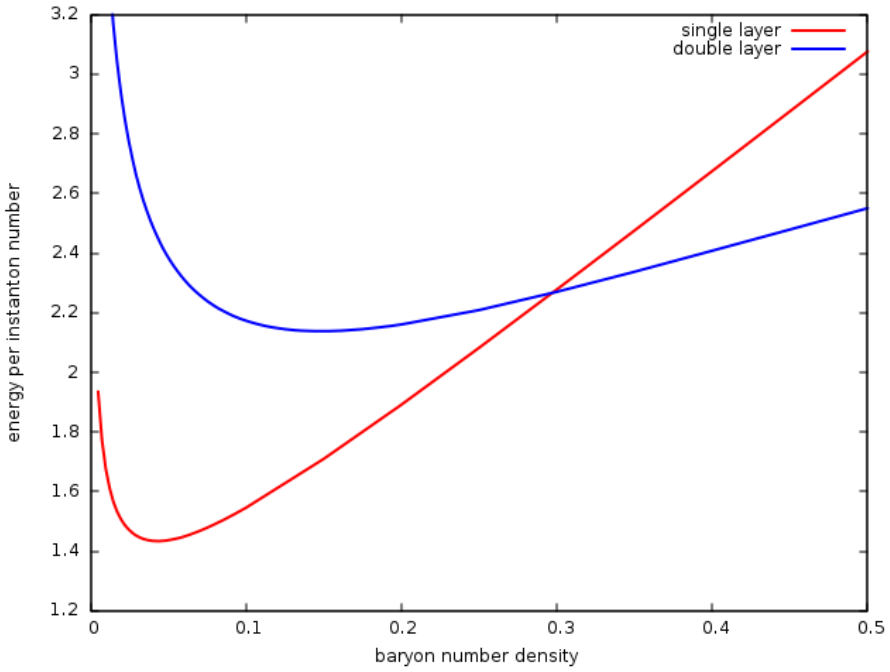

Figure 5.1: Energy per instanton number $\mathcal{E}/\rho$ (in units of $8\pi^2$) as a function of baryon number density ρ for the single-layer (red) and double-layer (blue) solutions in the singular homogeneous ansatz with $\Lambda = 10$.

though $h(z)$ is discontinuous at $z = 0$ for this ansatz, ω' is continuous. This should be expected, since ω' is a gauge invariant (and therefore physical) quantity.

Furthermore, we can take the limit of (5.3.7) as $z \to \infty$ to obtain

$$\lim_{z\to\infty} z^2\omega' = -\frac{4\alpha^3}{\Lambda} = -\frac{16\pi^2\rho}{\Lambda}\,. \tag{5.3.14}$$

This then reproduces the usual holographic result relating the asymptotic behaviour of the abelian electric potential to the baryon number density [76, 77]:

$$\omega(z) = \frac{16\pi^2\rho}{\Lambda z} + o\left(\frac{1}{z}\right)\,, \tag{5.3.15}$$

where we recall that we are working in the canonical ensemble with zero chemical potential.

We can find numerical solutions to (5.3.8) by using a gradient flow method, along with a change of variable $z = \tan u$ to map the holographic coordinate onto a finite range. The solutions described below were obtained on a grid of 2000 points equally spaced in $u > 0$, with $u < 0$ obtained by symmetry. Derivatives were calculated using fourth-order accurate approximations.

The red curve in Figure 5.1 shows the ratio of the energy per instanton number to the lower bound $\mathcal{E}/(8\pi^2\rho)$ as a function of the baryon number density ρ for the numerically obtained single-layer solutions. We find a critical density at $\rho_1 = 0.044$ at which the energy per soliton is minimal, corresponding to an analogue of the nuclear matter density in QCD.

Figure 5.2 shows the profile functions and instanton number densities per unit 3-volume of single-layer solutions with $\rho = 0.1$ and $\rho = 2$ and $\Lambda = 10$. Note that, even at high densities, it is difficult to see a clear indicator of the dyon salt configuration emerging, whereby the soliton splits into a number of constituents with fractional topological charge. This is another major drawback of the singular ansatz when compared to the kink ansatz, as we will see later. In fact, this is reminiscent of the problems encountered in the study of the low-dimensional homogeneous approximation of Chapter 4; there, the homogeneous ansatz forced solutions to lie in the dyon salt regime and so comparisons between salt and popcorn were impossible.

Previous work on low-dimensional toy models [62, 6] suggest that a popcorn transition [4] should appear before the formation of a dyonic salt. In other words, at high densities there should be a competing configuration corresponding to a double-layer of solitons with lower energy than any of the above configurations discussed. While it is difficult to identify the dyon salt within this singular ansatz, we nonetheless proceed by constructing such a double-layer solution, and find that at high densities the double-layer is indeed energetically favourable.

5.3.1 Baryonic popcorn in the singular ansatz

To create a solution with two layers of solitons separated in the holographic direction we add a discontinuity in $h(z)$ at some $z = z_0$ and minimise (5.3.3) piecewise in both $z \in (0, z_0)$ and $z \in (z_0, \infty)$, obtaining the profiles for $z < 0$ by symmetry. Our boundary conditions are now $h(0) = h(\infty) = \omega(\infty) = \omega'(0) = 0$, $h(z_0^{\pm}) = \pm 1$ and we demand ω' to be continuous across the discontinuity, since this should be a physical quantity. Furthermore, $h(z)$ and ω' should be odd functions of z.

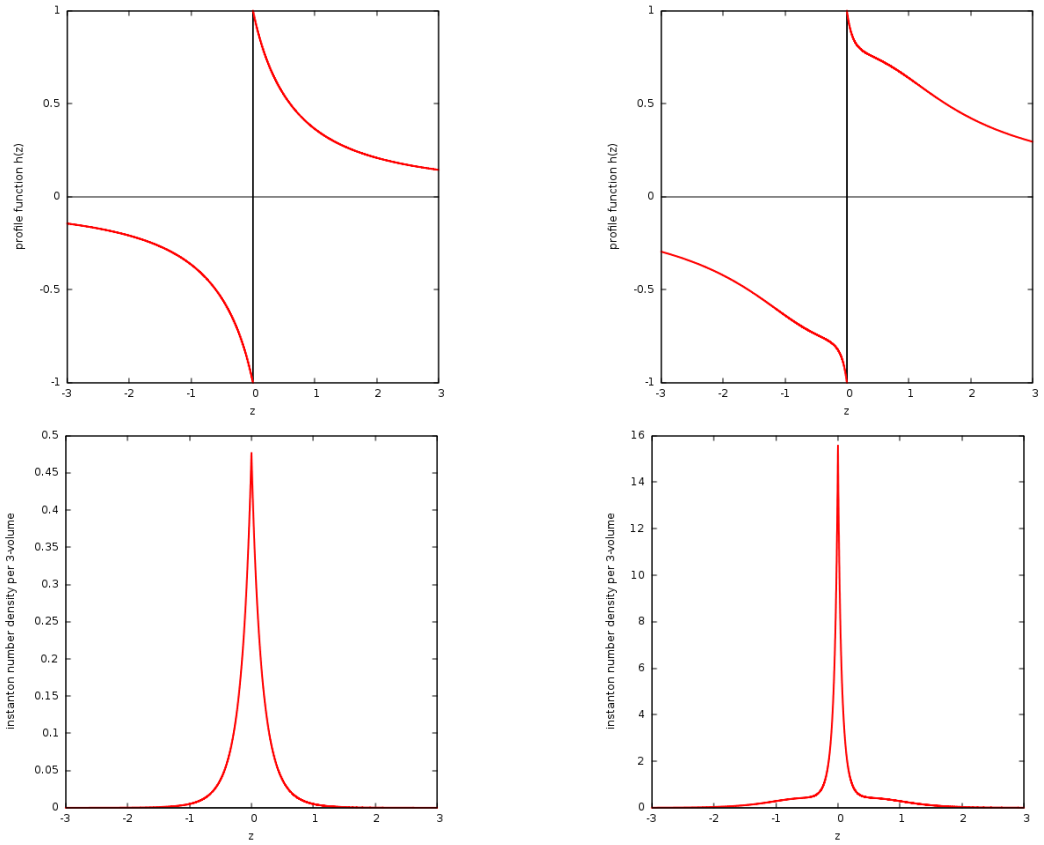

Figure 5.2: Profile functions $h(z)$ (top) and instanton number densities per unit 3-volume (bottom) for single-layer solutions in the singular homogeneous ansatz with $\rho = 0.1$ (left) and $\rho = 2$ (right) for $\Lambda = 10$.

The baryon number density is given by

$$\rho = -\frac{\alpha^3}{4\pi^2}\int_0^\infty \left(h^3\right)' dz = -\frac{\alpha^3}{4\pi^2}(-h^3(z_0^+) + h^3(z_0^-)) = \frac{\alpha^3}{2\pi^2}\,, \tag{5.3.16}$$

which implies $\alpha = (2\pi^2\rho)^{1/3}$. We see each layer carries half of the total baryon number density of the full configuration.

Piecewise, the equations of motion for the fields are the same as in (5.3.7) and (5.3.8), although we need to fix different integration constants in each piece. In $z \in (0, z_0)$ we set $c_1 = 0$ to ensure ω' is odd. Following similar steps to the previous section, we then find we can write

$$\mathcal{E}_{0<z<z_0} = \int_0^{z_0}\left\{3\alpha^2 H^{3/2}\,(h')^2 + \frac{3\alpha^4}{H^{1/2}}h^4 + \frac{16\alpha^6}{\Lambda^2 H^{3/2}}h^6\right\} dz + \frac{8\alpha^3}{\Lambda}\omega(z_0^-)\,, \tag{5.3.17}$$

where we have used $h(z_0^-) = -1$.

Fixing $c_1 = 0$ in $z \in (0, z_0)$ then implies $(H^{3/2}\omega')(z_0) = -\frac{4\alpha^3}{\Lambda}$, so for continuity we set

$c_1 = 2$ in $z \in (z_0, \infty)$. Using the same manipulations again we now find

$$\mathcal{E}_{z>z_0} = \int_{z_0}^{\infty} \left\{ 3\alpha^2 H^{3/2} (h')^2 + \frac{3\alpha^4}{H^{1/2}} h^4 + \frac{16\alpha^6}{\Lambda^2 H^{3/2}} \left(h^3 - 2\right)^2 \right\} dz - \frac{8\alpha^3}{\Lambda} \omega(z_0^+) \,. \quad (5.3.18)$$

If we require $\omega(z)$ to be continuous across the discontinuity then the constant terms in (5.3.17) and (5.3.18) cancel, and the variations of the two functionals yield consistent equations of motion for $h(z)$ in both pieces. As a further consistency check, substituting our choice $c_1 = 2$ for $z \in (z_0, \infty)$ into (5.3.7) and taking the limit as $z \to \infty$ gives

$$\lim_{z\to\infty} z^2 \omega' = -\frac{8\alpha^3}{\Lambda} = -\frac{16\pi^2 \rho}{\Lambda} \,, \quad (5.3.19)$$

and we obtain the same holographic relation (5.3.14) as in the single-layer case.

The ratio of the energy per instanton number to the lower bound $\mathcal{E}/(8\pi^2\rho)$ as a function of the baryon number density ρ for the double-layer is shown by the blue curve in Figure 5.1, and we can clearly see a critical density $\rho_2 = 0.30$ at which a double-layer of solitons becomes more energetically favourable than a single layer. This is the analogue of a popcorn transition in this singular model. The profile functions and instanton number densities per unit 3-volume of double-layer solutions with $\rho = 0.1$ and $\rho = 2$ can be found in Figure 5.3.

For the double-layer solutions it is easy to see that the layers begin to explore the holographic direction at higher densities, since the instanton number density peaks become more separated. However, it is difficult to compare the double-layer popcorn transition to the dyon salt configuration since the salt is not easily identifiable.

To conclude this section, we have (briefly) analysed a singular homogeneous ansatz for the Sakai-Sugimoto model and found that this does, indeed, predict a popcorn transition to a two-layered configuration at some critical density. However, the singular nature of the ansatz and the difficulty in identifying an analogue of the dyon salt arrangement make this ansatz somewhat undesirable. One could speculate that there would exist further popcorn transitions in this model, to further multi-layered configurations. These ansätze could be constructed by generalising the above method and adding extra discontinuities at the locations of each layer. However, we shall not perform such an analysis here, due to the aforementioned drawbacks of the ansatz, and will instead save this analysis for the following discussion of the kink ansatz.

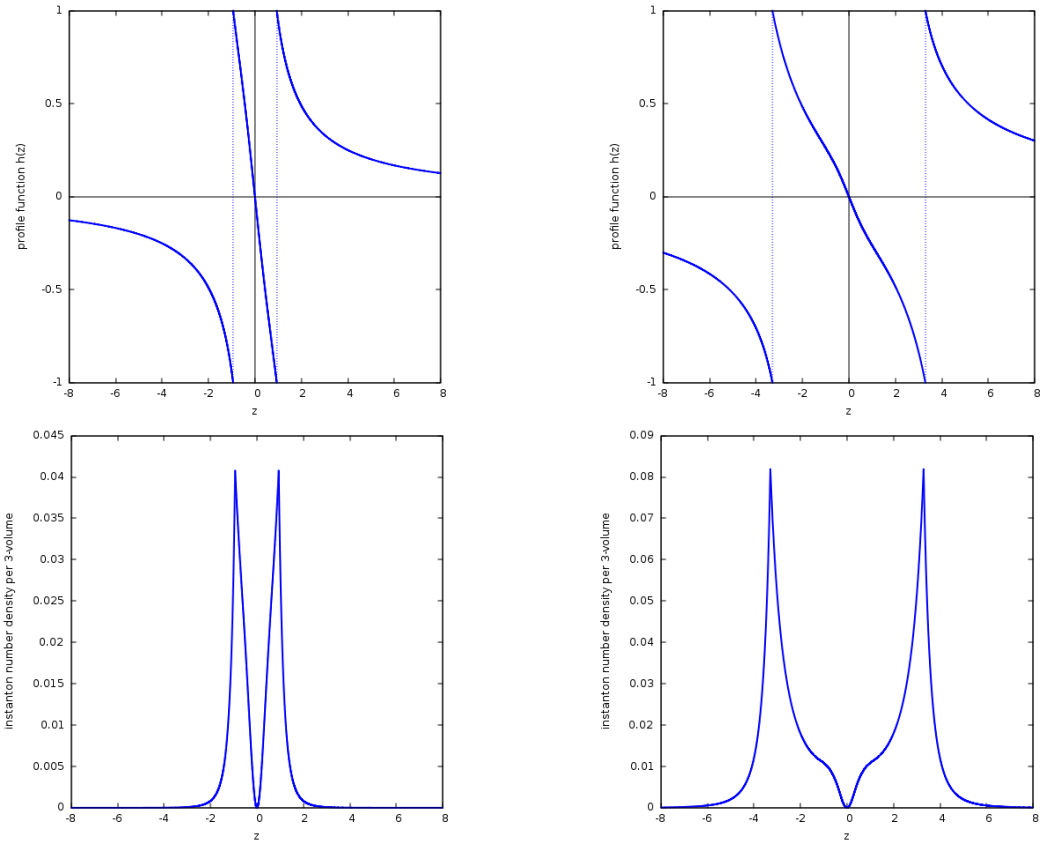

Figure 5.3: Profile functions $h(z)$ (top) and instanton number densities per unit 3-volume (bottom) for double-layer solutions in the singular homogeneous ansatz with $\rho = 0.1$ (left) and $\rho = 2$ (right) for $\Lambda = 10$.

5.4 The kink ansatz: homogeneous field strengths

When we studied homogeneous approximations in the low-dimensional toy model in Chapter 4 we found that the combination of imposing spatial homogeneity on the boundary conditions and periodicity in the non-holographic direction forced solutions to lie in the dyon salt phase. However, the nature of the high-dimensional model allows us to explore other options for imposing homogeneity. Crucially, the five-dimensional Sakai-Sugimoto model is a gauge theory and the boundary condition on the gauge fields is that they must approach pure gauge at $z = \infty$. The boundary values of the gauge fields must then satisfy a zero curvature condition, and this allows us to construct a new homogeneous approximation as detailed below. The low-dimensional model, on the other hand, approximates the gauge theory by an $O(3)$ sigma model. There is no such zero curvature condition we can exploit, and so the boundary conditions on the model force solutions to be salty.

Static solutions in the Sakai-Sugimoto model satisfy $A_z = 0$. On the other hand, in $A_z = 0$ gauge the gauge fields can be decomposed into eigenfunctions in the holographic direction as

$$A_i(\boldsymbol{x}, z) = iR_i(\boldsymbol{x})\psi(z) + \sum_{n=1}^{\infty} V_n(\boldsymbol{x})\psi_n(z)\,, \tag{5.4.1}$$

where $R_i = (\partial_i U)\, U^{-1}$, $U \in SU(2)$ and $\psi(z) \to 1$, $\psi_n(z) \to 0$ as $z \to \infty$. The R_i's satisfy the zero curvature condition

$$\partial_i R_j - \partial_j R_i = [R_i, R_j]\,. \tag{5.4.2}$$

At leading order (i.e. ignoring V_n), the field strength is then given by

$$F_{ij} = -i[R_i, R_j]\psi(\psi - 1)\,, \qquad\qquad F_{iz} = -iR_i\psi'\,. \tag{5.4.3}$$

We now apply a homogeneous approximation at the level of the field strength tensors by substituting $R_i = i\beta\sigma_i/2$. It is crucial we substitute into (5.4.3) as the approximation does not satisfy the zero curvature condition (5.4.2). The result gives

$$\hat{A}_0 = \omega(z)\,, \qquad F_{ij} = -\frac{\beta^2}{2}\psi(\psi - 1)\varepsilon_{ijk}\sigma_k\,, \qquad F_{iz} = \frac{\beta}{2}\psi'\sigma_i\,, \tag{5.4.4}$$

where $\psi(z)$ is both smooth and continuous with boundary conditions $\psi(-\infty) = 0$ and $\psi(\infty) = 1$. The advantage of this approximation is that it is no longer necessary to introduce any discontinuities of the fields since nontrivial topology now comes from a winding of the fields at $z = \infty$.

It is worth stressing that this approximation is not a solution to the field equations derived from (5.2.3), since we have utilised the zero-curvature condition which homogeneous fields do not satisfy. The approximation is, nevertheless, helpful and allows us to reduce a 4-dimensional problem to that of a kink in 1-dimension. We interpret our homogeneous approximation as a smeared version of the true spatial distribution of the fields in the non-holographic directions, which we expect to form a soliton crystal. We also expect the smeared approximation to provide a lower bound on the true crystal energy since the imposed homogeneity is an unattainable idealisation. This claim is justified by an analysis of the simpler case of the Skyrme crystal, which will be found in Appendix C.

Furthermore, the expressions in (5.4.4) are very similar to those that appear by replacing the Euclidean spatial volume by a finite radius three-sphere, as studied in [71]. The parameter β is then analogous to the inverse radius of the three-sphere. However, in [71] the form of the analogue of the kink function $\psi(z)$ was fixed to be of self-dual form, preventing a study of how the bulk soliton explores the holographic direction, which is the main purpose of this chapter. It may be interesting to repeat the analysis here for the case of the three-sphere without freezing the form of the kink field, since then a genuine homogeneous ansatz is possible.

We can (loosely) interpret the homogeneous approximation in Euclidean space as a spatial average of the three-sphere solution at infinite radius. After re-writing the three-sphere ansatz from [71] in a Cartesian basis, Euclidean space can be recovered by sending the three-sphere radius to infinity, and the approximation (5.4.4) can be obtained by taking an $O(1)$ expansion in the angular variables around $\psi = \theta = \phi = 0$.

We now seek solutions to the homogeneous approximation (5.4.4). Again, we begin by working in the canonical ensemble (i.e. zero chemical potential), so the abelian electric potential is also a smooth, continuous function with boundary condition $\omega(\pm\infty) = 0$.

The constant β is, again, fixed by calculating the baryon number density of the ansatz,

$$\rho = -\frac{3\beta^3}{8\pi^2}\int_{-\infty}^{\infty}\left(\frac{\psi^3}{3} - \frac{\psi^2}{2}\right)' dz = \frac{\beta^3}{16\pi^2}\,, \tag{5.4.5}$$

and the static energy per 3-volume is

$$\mathcal{E} \equiv \frac{E}{V} = \mathcal{E}_{YM} + \mathcal{E}_{CS}\,, \tag{5.4.6}$$

where

$$\mathcal{E}_{YM} = \frac{1}{2}\int_{-\infty}^{\infty}\left\{3\beta^2 H^{3/2}\left(\psi'\right)^2 + \frac{3\beta^4}{H^{1/2}}\psi^2(\psi-1)^2 - H^{3/2}\left(\omega'\right)^2\right\} dz\,, \tag{5.4.7}$$

$$\mathcal{E}_{CS} = \frac{1}{2}\int_{-\infty}^{\infty}\left\{-\frac{24\beta^3}{\Lambda}\omega\left(\frac{\psi^3}{3} - \frac{\psi^2}{2}\right)'\right\} dz\,. \tag{5.4.8}$$

With this ansatz the equations of motion for $\omega(z)$ and $\psi(z)$ are

$$\delta\omega: \qquad \left(H^{3/2}\omega'\right)' = \frac{12\beta^3}{\Lambda}\left(\frac{\psi^3}{3} - \frac{\psi^2}{2}\right)'\,, \tag{5.4.9}$$

$$\Rightarrow \qquad H^{3/2}\omega' = \frac{12\beta^3}{\Lambda}\left(c_1 + \frac{\psi^3}{3} - \frac{\psi^2}{2}\right)\,, \tag{5.4.10}$$

$$\delta\psi: \qquad \left(H^{3/2}\psi'\right)' = \frac{\beta^2}{H^{1/2}}\psi(\psi-1)(2\psi-1) + \frac{4\beta}{\Lambda}\psi(\psi-1)\omega'$$
$$\Rightarrow \quad \psi'' + \frac{3H'}{2H}\psi' = \frac{\beta^2}{H^2}\psi(\psi-1)\left[(2\psi-1) + \frac{48\beta^2}{\Lambda^2 H}\left(c_1 + \frac{\psi^3}{3} - \frac{\psi^2}{2}\right)\right], \quad (5.4.11)$$

where c_1 is a constant of integration that needs to be fixed. The leading order tail decay of the profile function is given by $\psi(z) \sim 1 + 1/z$.

Since the profile functions are all continuous, the constant c_1 can be fixed by requiring $\lim_{z\to\pm\infty} H^{3/2}\omega' = \pm C$. This gives $c_1 = 1/12$ and $C = -\beta^3/\Lambda$. In other words,

$$\lim_{z\to\infty} H^{3/2}\omega' = \lim_{z\to\infty} z^2\omega' = -\frac{\beta^3}{\Lambda} = -\frac{16\pi^2\rho}{\Lambda}\,, \quad (5.4.12)$$

and we obtain the same holographic relation (5.3.14) as before.

We can now eliminate the abelian electric potential from integrals (5.4.7) and (5.4.8) by multiplying (5.4.9) by ω and integrating by parts. The resulting boundary term vanishes and leaves us with

$$\mathcal{E} = \frac{1}{2}\int_{-\infty}^{\infty}\left\{3\beta^2 H^{3/2}\left(\psi'\right)^2 + \frac{3\beta^4}{H^{1/2}}\psi^2(\psi-1)^2 + \frac{144\beta^6}{\Lambda^2 H^{3/2}}\left(\frac{1}{12} + \frac{\psi^3}{3} - \frac{\psi^2}{2}\right)^2\right\} dz\,, \quad (5.4.13)$$

whose variation with respect to $\psi(z)$ then reproduces (5.4.11).

Note that imposing the self-duality equations on our ansatz (5.4.4) yields the equation

$$\psi' = -\beta\psi(\psi-1)\,, \quad (5.4.14)$$

which has the explicit solution

$$\psi(z) = \frac{1}{1+\mathrm{e}^{-\beta z}}\,. \quad (5.4.15)$$

Substituting this into the energy, ignoring the Chern-Simons term and going to the flat-space limit ($H = 1$) gives $\mathcal{E} = \beta^3/2 = 8\pi^2\rho$, and we recover the BPS behaviour of flat-space instantons.

We can find numerical solutions to (5.4.11) by using a gradient flow method, along with a change of variable $z = \tan u$ to map the holographic coordinate onto a finite range. Solutions were obtained on a grid of 2000 points equally spaced in $u > 0$, with $u < 0$ obtained by symmetry: again, the energy is minimised by a bulk configuration localised

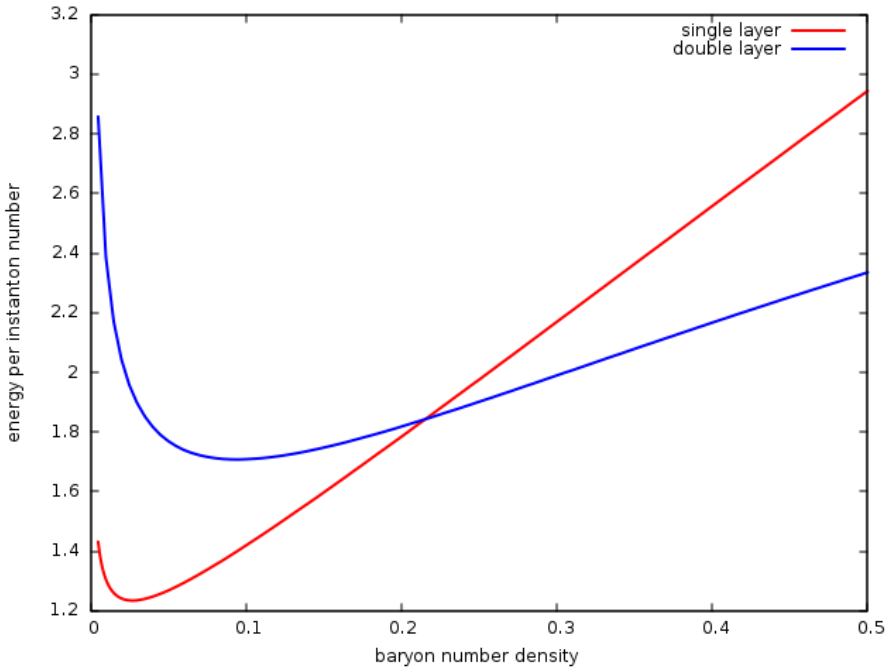

Figure 5.4: Energy per instanton number $\mathcal{E}/\rho$ (in units of $8\pi^2$) as a function of baryon number density ρ for the single-layer (red) and double-layer (blue) solutions in the second homogeneous ansatz with $\Lambda = 10$.

around $z = 0$ so we impose $\omega(-z) = \omega(z)$ and $\psi(-z) = 1 - \psi(z)$ to ensure that the instanton number density and abelian electric potentials are both even functions of z. Derivatives were calculated using fourth-order accurate approximations.

The red curve in Figure 5.4 shows the ratio of the energy per instanton number to the lower bound $\mathcal{E}/(8\pi^2\rho)$ as a function of baryon number density ρ for the numerically obtained single-layer solutions. We find there is a critical density $\rho_1 = 0.027$ at which the energy per instanton number is minimal, corresponding to an analogue of the QCD nuclear matter density. This optimal density corresponds to a first-order phase transition to an equilibrium of nuclear matter, as described below.

So far we have worked in a canonical ensemble (i.e. fixed baryon number density), but an alternative approach is to work in a grand canonical ensemble where we fix a chemical potential μ and allow the baryon number density to vary. In holographic theories a chemical potential usually corresponds to a boundary value for $\hat{A}_0$ [74, 75], and we can recover this from the above by transforming the energy into the grand potential (also known as the Landau free energy) $\Omega = \mathcal{E} - \mu\rho$. To do this we shift ω

by a constant, $\omega \to \omega - \mu\Lambda/32\pi^2$, which then gives us

$$\omega(\infty) = -\frac{\mu\Lambda}{32\pi^2}\,. \tag{5.4.16}$$

The free energy Ω can then be minimised with respect to the chemical potential μ, and the resulting function $\Omega(\mu)$ can be seen in Figure 5.5. The associated relationship between the baryon number density ρ and the chemical potential μ can be seen in Figure 5.6. We find that the equilibrium baryon number density is zero below a critical chemical potential $\mu_1 = 97.5$, where μ_1 is the critical value of the chemical potential at which the baryon number density is, indeed, equal to ρ_1 (for $\Lambda = 10$).

On general grounds, the critical chemical potential should be the same order as the baryon mass. With our choice of units, the flat space instanton approximation gives the baryon mass (to leading order in $1/\Lambda$) as

$$M_B = 2\pi^2\left(4 + \frac{32}{\Lambda}\sqrt{\frac{2}{15}}\right)\,, \tag{5.4.17}$$

(see [50]) which, when substituting in $\Lambda = 10$ gives us $M_B = 102$. This is seen to be greater than the critical chemical potential $\mu_1 = 97.5$, and so the baryons form bound states. In fact, the percentage binding energy, given by

$$\Delta = \left(1 - \frac{\mu_1}{M_B}\right) \times 100\%\,, \tag{5.4.18}$$

yields $\Delta = 4\%$ for our chosen value of $\Lambda = 10$. In the limit $\Lambda \to \infty$ we recover the BPS limit, $M_B \to 8\pi^2$ and $\mu_1 \to M_B$, which gives zero binding energy. Although we expect holographic QCD to only give qualitative predictions about physical three-colour QCD, our result implies that there should be a value of Λ greater than 10 at which a realistic binding energy of $\Delta \sim 0.9\%$ is obtained; we compute that the appropriate value is $\Lambda \sim 18$.

Returning to our value of $\Lambda = 10$, Figure 5.7 shows the profile functions, instanton number densities per 3-volume and abelian electric potentials of single-layer solutions with $\rho = 0.1$ and $\rho = 2$. At the higher density we observe the predicted dyon salt behaviour, where the instanton layer splits into two constituents, each carrying half the instanton charge of the full solution. This corresponds to the fact that a periodic instanton (a caloron) splits into monopole constituents at high density. Note that these

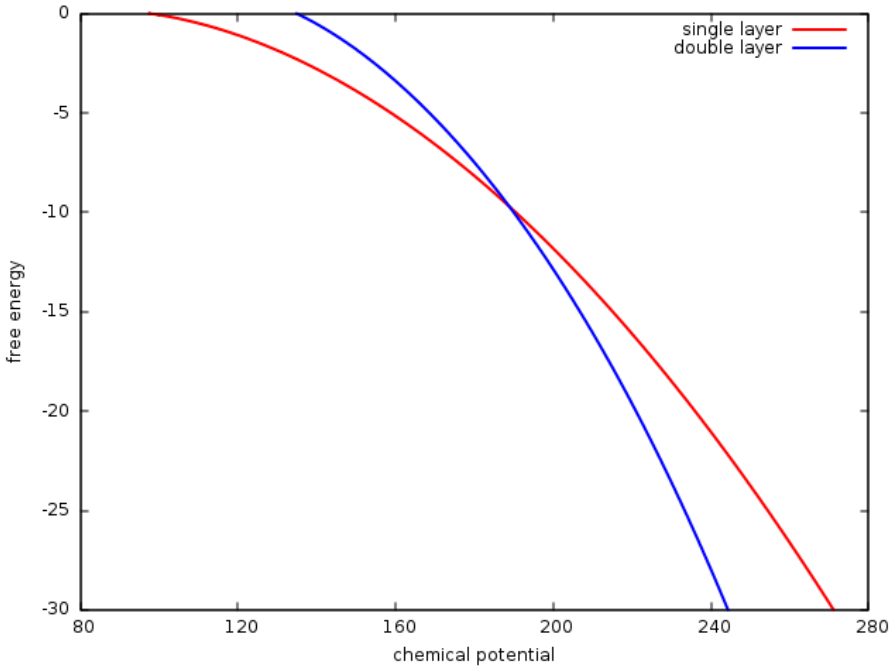

Figure 5.5: Landau free energy $\Omega = \mathcal{E} - \mu\rho$ as a function of chemical potential μ for single- (red) and double- (blue) layer configurations in the homogeneous kink ansatz with $\Lambda = 10$.

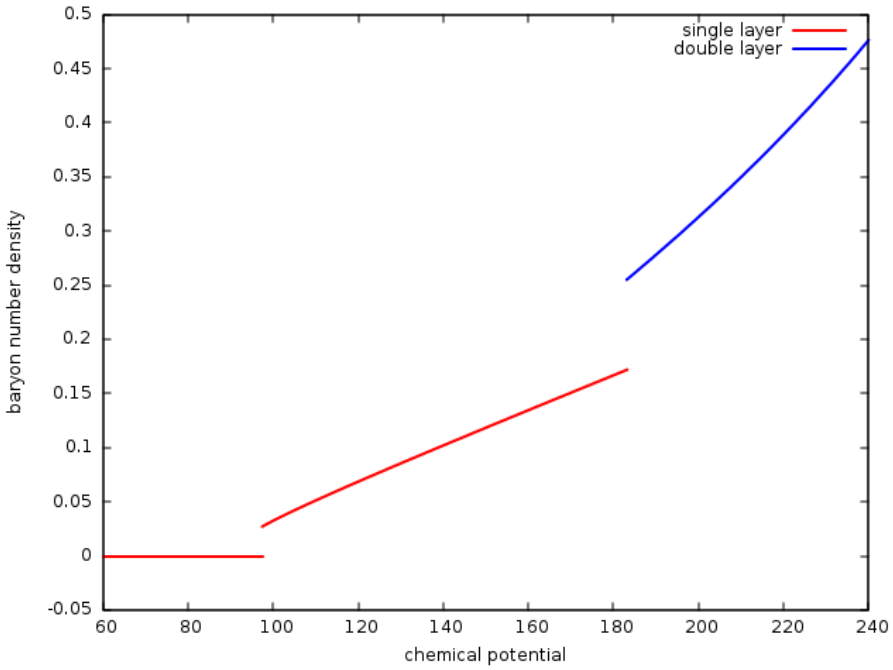

Figure 5.6: Baryon number density ρ as a function of chemical potential μ in the homogeneous kink ansatz with $\Lambda = 10$. The lower curve (red) corresponds to single-layer solutions and demonstrates a fist-order transition to nuclear matter just below the baryon mass, at $\mu = \mu_1 = 97.5$. The upper curve (blue) corresponds to double-layer solutions, demonstrating a first-order transition to baryonic popcorn at $\mu = \mu_2 = 189$.

half-kinks cannot exist in isolation as they interpolate between values that differ by 1/2, but this difference must be either 0 or ±1 for finite energy. This mirrors the splitting of calorons at high density, where the monopole constituents themselves are not solutions to the field equations in isolation, but combine to form a periodic instanton.

The emergence of the dyon salt splitting at high densities can be easily understood by looking at the potential terms in the effective energy (5.4.13). The term proportional to β^4 has an explicit spatial dependence that grows like $z^{-2/3}$ for large z, which does not decay fast enough to be integrable. This means that, as $z \to \pm\infty$, the multiplying factor must tend to zero. This, in fact, forces the boundary condition $\psi(\pm\infty) \in \{0, 1\}$. The term proportional to β^6, on the other hand, has explicit spatial dependence that grows like z^{-2}, which does decay fast enough to be integrable. This means that this term is minimised when the multiplying factor vanishes, which only occurs when $\psi(z) = 1/2$. As the baryon number density increases, the sixth-order term dominates over the fourth-order term, which induces the profile function ro remain as close to the value 1/2 over an increasingly large range of z, while still remaining fixed on the boundary due to the fourth-order term and finite energy requirement. This generates the splitting of the kink into a pair of half-kinks, and gives rise to the dyon salt configuration.

5.4.1 Baryonic popcorn and soliton bags in the kink model

One way to generate an ansatz for a double-layer configuration, in order to search for the possibility of baryonic popcorn, is to continuously patch together the kink solution with an anti-kink. An anti-kink with boundary conditions $\psi(-\infty) = 1$ and $\psi(\infty) = 0$ can be obtained by transforming $\psi \to 1 - \psi$; such a solution has the same energy per unit 3-volume as the kink but with negative baryon number density. However, if we also make the transformation $F_{ij} \to -F_{ij}$ in (5.4.4) we can make this baryon number density positive again, thus finding an anti-kink formulation of a single-layer solution that is equivalent to that described by a kink in the previous section.

We now patch together these two single-layer solutions in a continuous manner to create a double-layer solution. Explicitly, for $z \geq 0$ we take the kink solution (5.4.4) above with boundary conditions on the half-line, $\psi(0) = 0$ and $\psi(\infty) = 1$. For $z \leq 0$ we take the same approximation but with $F_{ij} \to -F_{ij}$ and solve for anti-kink boundary

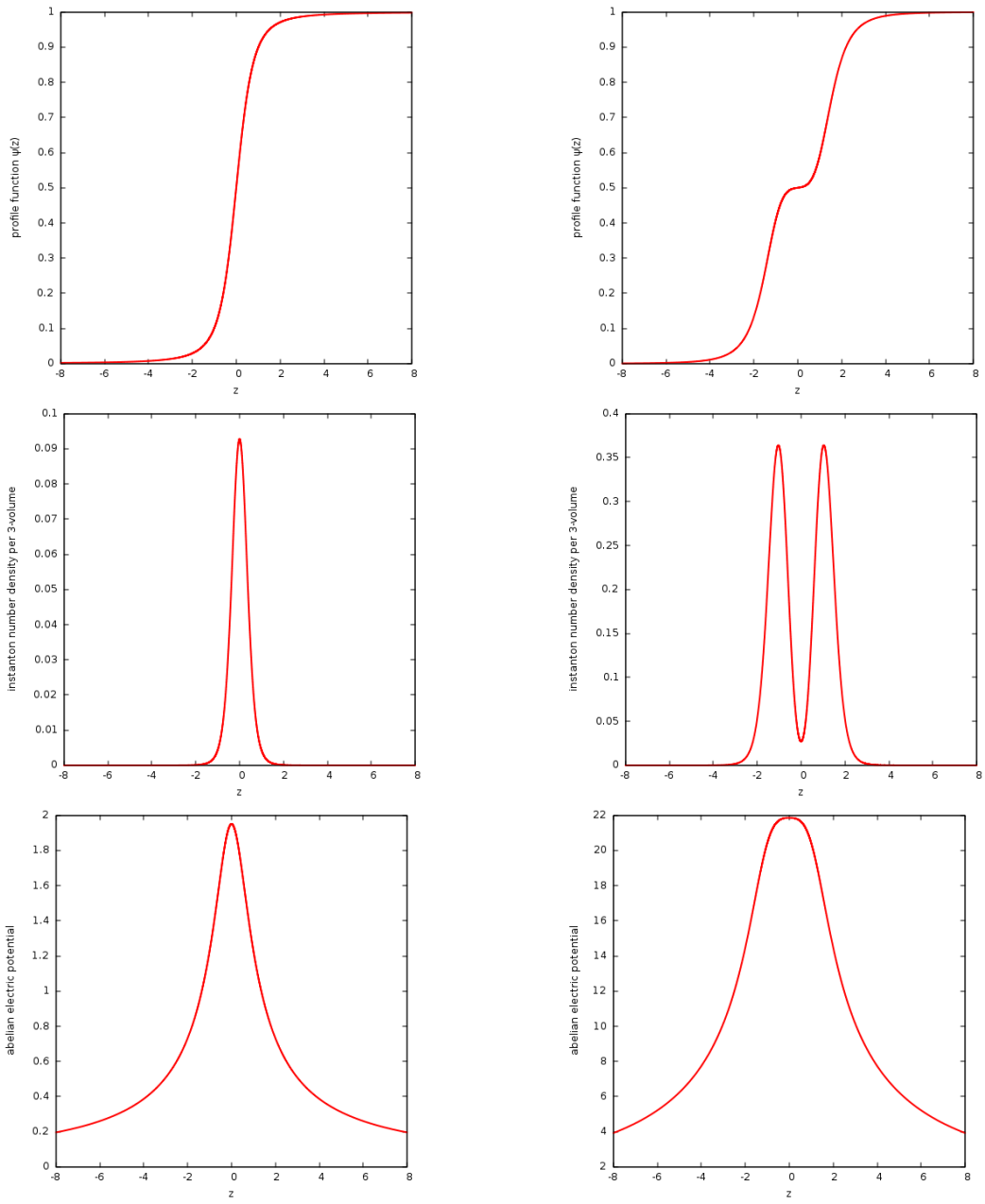

Figure 5.7: Profile functions $\psi(z)$ (top), instanton number densities per unit 3-volume (middle) and abelian electric potentials $\omega(z)$ (bottom) for single-layer solutions in the homogeneous kink ansatz with $\rho = 0.1$ (left) and $\rho = 2$ (right) for $\Lambda = 10$.

conditions on the half-line, $\psi(-\infty) = 1$ and $\psi(0) = 0$. This implies that $\psi(z)$ and $\omega(z)$ must be even functions of z. Furthermore, the instanton number density (per 3-volume) is continuous across the join (it vanishes at $z = 0$), although it is not smooth there. It should be noted that the sign flip in F_{ij} across $z = 0$ is analogous to the sign flip in the second component of $\boldsymbol{\phi}$ in the homogeneous ansatz in the low-dimensional toy model.

Restricting to $z \geq 0$, the baryon number density is then given by

$$\rho = -\frac{3\beta^3}{4\pi^2}\int_0^\infty \left(\frac{\psi^3}{3} - \frac{\psi^2}{2}\right)' dz = \frac{\beta^3}{8\pi^2}\,. \tag{5.4.19}$$

For the double-layer we fix the constant in the integrated field equation (5.4.10) using the new boundary conditions $\omega'(0) = 0$ and $\psi(0) = 0$, to obtain $c_1 = 0$. Taking the limit of this equation as $z \to \infty$ then gives us the holographic relation

$$\lim_{z\to\infty} z^2\omega' = -\frac{2\beta^3}{\Lambda} = -\frac{16\pi^2\rho}{\Lambda}\,, \tag{5.4.20}$$

and the correct asymptotic behaviour is reproduced once again.

As in the single-layer case, we can perform an integration by parts to obtain an expression for the double-layer energy,

$$\mathcal{E} = \int_0^\infty \left\{ 3\beta^2 H^{3/2}\left(\psi'\right)^2 + \frac{3\beta^4}{H^{1/2}}\psi^2(\psi-1)^2 + \frac{144\beta^6}{\Lambda^2 H^{3/2}}\left(\frac{\psi^3}{3} - \frac{\psi^2}{2}\right)^2 \right\} dz\,, \tag{5.4.21}$$

which has no explicit dependence on the abelian electric potential ω. The double-layer solution can then be obtained by numerically solving the field equation arising from the variation of this energy with respect to $\psi(z)$. The ratio of the energy per instanton number to the lower bound $\mathcal{E}/(8\pi^2\rho)$ as a function of the baryon number density ρ is shown by the blue curve in Figure 5.4 and we can clearly see a critical density $\rho_2 = 0.22$ at which the double-layer becomes more energetically favourable than the single-layer. This is the analogue of a popcorn transition in this homogeneous model. Crucially we find that this transition occurs well below the density at which the dyon salt configuration manifests, which is in agreement with the aforementioned low-dimensional studies.

The profile functions, instanton number densities (per unit 3-volume) and abelian electric potentials for double-layer solutions with $\rho = 2$ and $\rho = 10$ can be found in

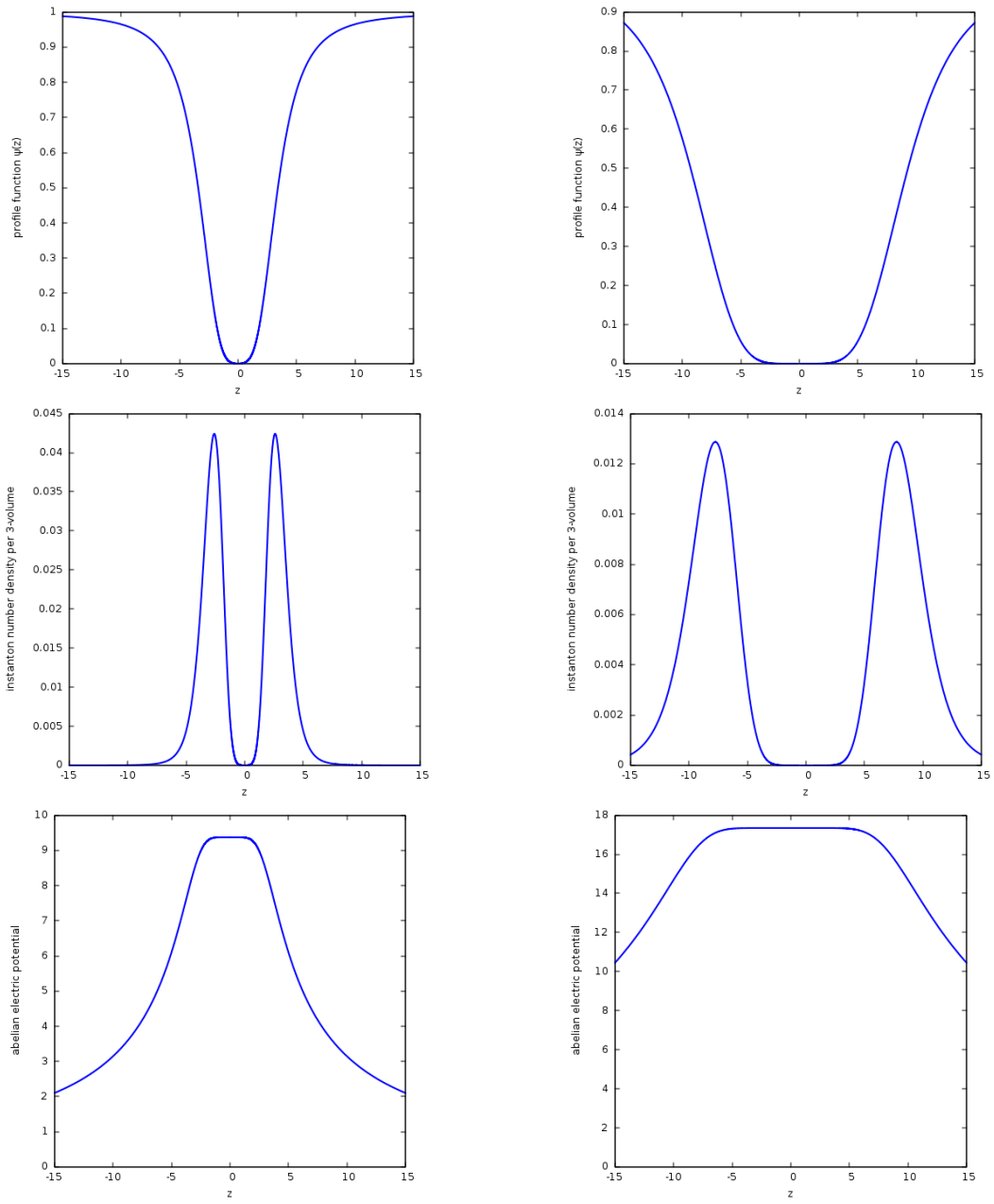

Figure 5.8: Profile functions $\psi(z)$ (top), instanton number densities per unit 3-volume (middle) and abelian electric potentials $\omega(z)$ (bottom) for double-layer solutions in the homogeneous kink ansatz with $\rho = 2$ (left) and $\rho = 10$ (right) for $\Lambda = 10$.

Figure 5.8. Although there are qualitative similarities between the double-layer and the dyon salt configurations, the two solutions are mathematically distinct since the half-layer constituents of the dyon salt may not exist in isolation. Furthermore, there are significant quantitative differences between the two, most notably that the double-layer configurations at these high densities have significantly lower energies per baryon number.

As before, we can extract the relationship between baryon number density and chemical potential for the double-layer by analysing the free energy of the configurations. The blue curve in Figure 5.5 shows the minimal free energies for the double-layer configurations as a function of the chemical potential, and we see a transition from the single- to the double-layer around chemical potential $\mu_2 = 189$. Furthermore, Figure 5.6 shows that this is a first-order phase transition: there is a discontinuous jump around $\mu = \mu_2$ as the curve switches from the single- to the double-layer. It should be noted that both curves shown in Figure 5.6 extend beyond the regions plotted, but in these extended regions the corresponding solutions are no longer global minima, and so are physically irrelevant.

We have also plotted the variation of the critical chemical potentials μ_1 and μ_2 as functions of the rescaled 't Hooft coupling Λ. The red and blue curves in Figure 5.9 correspond to the baryon onset and critical popcorn transition potentials respectively, and we see that the system tends towards a BPS limit in which the critical densities coincide with the baryon mass $M_B = 8\pi^2$ in the large Λ limit (as expected).

One might expect the individual layers of the double-layer configuration to split into half-kink constituents at high density, just as the single-layer splits into half-kink constituents. However, the plots in the right column of Figure 5.8 provide strong evidence to suggest that this does not occur, and instead the two layers simply increase their separation with increasing density. Once again there is a simple explanation for this behaviour which we can obtain by looking at the form of the effective kink potential in (5.4.21). This time, the sixth-order term is only minimised when $\psi = 0$ (if $\psi \in [0, 1]$), and so this term does not induce the field to stay close to any non-boundary value with increasing density. For this reason, the double-layer solutions do not undergo any splitting as the baryon number density increases, and

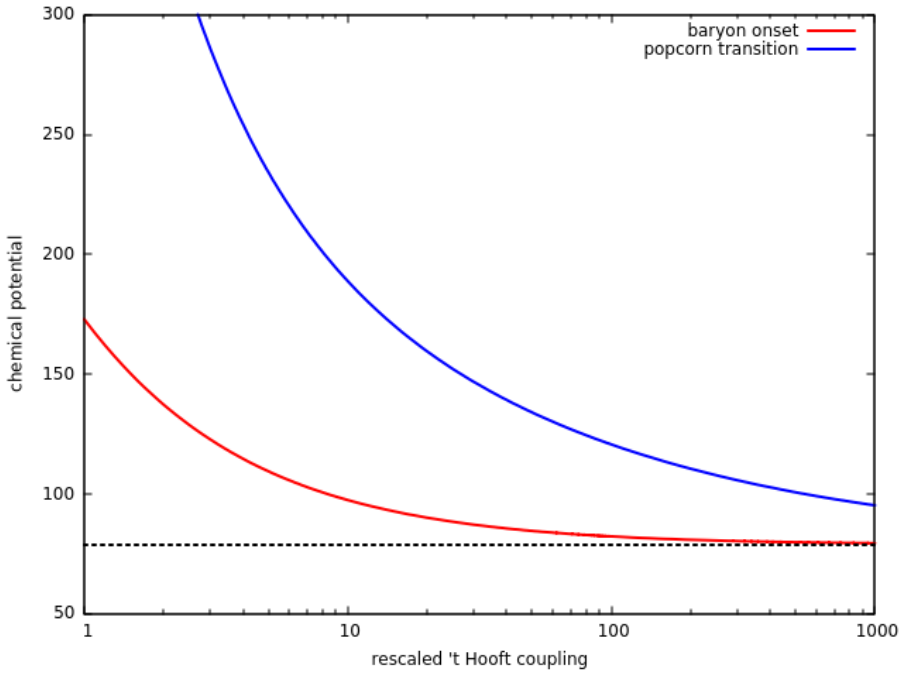

Figure 5.9: Critical chemical potentials μ_1 and μ_2 corresponding to the baryon onset (red) and first popcorn transition (blue) as a function of the 't Hooft coupling Λ in the homogeneous kink ansatz. The black dotted line corresponds to the chemical potential $\mu = 8\pi^2$, which coincides with the baryon mass in the large Λ limit.

instead their separation simply increases.

As the density increases it seems reasonable to expect further popcorn transitions to occur, to three- or four-layered configurations, and indeed this is what has been observed in a low-dimensional toy model [62]. As the layers of the double-layer configuration separate, one might expect a third layer to be generated in the region between them, localised around $z = 0$. However, this expectation ignores the fact that the region between the two layers is not empty, and is in fact filled with abelian electric potential, as demonstrated in Figure 5.8. The two layers form the surface of a soliton bag, whose interior is filled with (an almost constant) non-zero abelian electric potential. The electric potential decays to its boundary value outside the bag, and this transition region identifies the surface of the bag. The instanton number density (per unit 3-volume) and the electric field are then localised on the surface of the bag. This is similar to the magnetic bag description of large-charge non-abelian monopoles [72], where the surface of the bag separates regions of zero and non-zero values of the modulus of the Higgs field. Since the kink model studied here is periodic in three spatial directions (as approximated by homogeneity) the surface of the bag is not a

single connected component, as in the monopole case, but instead consists of two disconnected components separated in the holographic direction. This is why the soliton bag requires two layers.

Further popcorn transitions would produce a multi-layered bag configuration, and these have been studied in the context of magnetic monopoles in [78]. It was found that solutions took the form of a single bag surrounded by layers of isolated unit charge monopoles; any attempt at creating a multi-layered bag rules out the possibility of an interior bag carrying any significant fraction of the topological charge. Therefore, the soliton bag found in the homogeneous Sakai-Sugimoto model suggests that no further popcorn transitions occur beyond the first one. This view is further supported by an investigation into three- and four-layered ansätze within the kink model, obtained by continuously patching together longer strings of kinks and anti-kinks (with associated sign flips in F_{ij} at each join). The locations of the joins and the fraction of baryon number density held by each kink/anti-kink were allowed to vary, and the resulting energy minima were calculated numerically. In the four-layer case, as expected from the magnetic monopole bag study, no significant baryon number density was found in the inner layers, and only the outer layers were relevant. Similar results were also found in the three-layer case. This is in agreement with recent studies [79, 80] which, using different approximations, reached the same conclusion that a double-layer is preferred at high densities and no additional layers are generated. It is worth noting that these studies use the full string theory description of the Sakai-Sugimoto model, using a symmetric trace prescription to deal with the non-abelian DBI action, rather than the five-dimensional effective formulation we use here.

These results are qualitatively very different to those obtained in the low-dimensional toy models studied in [62] and Chapters 2 and 4, in which an infinite number of popcorn transitions were conjectured, and evidence for three-layer configurations were found. While the toy models were justified as low-dimensional analogues of Sakai-Sugimoto using (as described in Section 2.2), the fundamental difference between the two classes of model — $O(3)$ sigma model versus gauge theory — may be the source of the significant qualitative differences in their solutions. This has already been seen in the construction of the homogeneous approximations themselves:

in the high-dimensional case we were able to use the zero curvature condition of the boundary gauge fields to construct the kink ansatz, whereas there is no analogy of this technique in the toy models.

Finally, it should be emphasised that the soliton bag found here is not the same as the instanton bag proposed in [73] as a description of the high-density phase of the Sakai-Sugimoto model. In this paper the bag is obtained via a compactification of one spatial direction to allow the embedding of a monopole wall. A pair of such monopole walls are then patched together to form the surface of the instanton bag, and the interior of the bag is filled with instanton charge density. The soliton bag found in this kink model contrasts with this, since the instanton number density is localised on the surface of the bag. With an appropriate choice of shape for the kink profile function, the kink model introduced here could produce a bag filled with instanton number density, but such a shape does not appear when numerically minimising the effective kink model energy.

5.5 Conclusions

Understanding the phases of cold, dense holographic nuclear matter as a function of baryon number density or chemical potential is an open problem in theoretical physics. The distribution of baryonic matter is unknown in both the holographic and non-holographic directions, and this has led to the proposal of a number of approximate phenomena that may occur. In this chapter we have assumed spatial homogeneity in the non-holographic directions in two different ways in order to investigate the distribution in the holographic direction. Since the holographic coordinate corresponds to an energy scale in the boundary theory, an understanding of this distribution is likely to be important in discovering a holographic description of the baryonic Fermi surface of a quarkyonic phase.

Our first homogeneous ansatz assumed homogeneity at the level of the $U(2)$ gauge fields in the Sakai-Sugimoto model, and it was found that singular gauge fields were required for nontrivial topology. Within this ansatz there was no clear analogue of the proposed dyon salt phase, although a transition to a double-layer baryonic popcorn

phase was found to be preferable over a single-layer at high baryon number densities.

The second homogeneous ansatz imposed homogeneity at the level of the field strength, and reduced the $U(2)$ gauge theory to an effective kink model in one direction. Within this ansatz, no singular configurations were required, and the model was found to be capable of realising a number of previously suggested phases, including dyon salt, baryonic popcorn and soliton bags. The unification of these phases allows the preferred phases to be determined as the baryon chemical potential varies. The effective kink model also successfully predicted a first-order transition to lightly bound nuclear matter, as found in QCD.

Furthermore, we have found that the five-dimensional Sakai-Sugimoto model behaves qualitatively differently from the low-dimensional toy models, at least at the level of homogeneous approximations. There are a number of reasons why this may occur. Firstly, the toy model only has two spatial dimensions, as opposed to the four spatial dimensions of Sakai-Sugimoto, which could play a role. Secondly, the toy model uses a sigma model to approximate a gauge theory, and the differences between these classes of model could have significant effects. Finally, looking back to the vector meson model studied in [6] we see that the vector meson field, which plays the role of the abelian electric potential $\hat{A}_0$ in the Sakai-Sugimoto model, must have a nonzero mass term to allow for finite energy configurations, whereas there is no corresponding mass term in the Sakai-Sugimoto model. The presence of this mass means that the homogeneous equation of motion for the vector meson is no longer once-integrable, and the field cannot be eliminated from the Lagrangian as it was in this chapter.

In holographic QCD, the masses of the vector and axial vector mesons are determined by the spectrum of fluctuations in the holographic direction. As the background solution changes with increasing baryon number density so too does the spectrum, and this has been proposed [57] as a mechanism for approximate chiral symmetry restoration, with the vector and axial vector meson masses converging in the high density limit. The details of the correct background solutions, however, are unavailable, and studies so far into this idea have been primarily qualitative. This would still be a nontrivial calculation within the homogeneous kink model introduced here, but may be a tractable problem that would merit future research.

Chapter 6

Conclusions and outlook

The primary question in this thesis, motivated by an interest in finding a holographic analogue of cold, dense QCD, has been: "What structure does solitonic material have in the Sakai-Sugimoto model at finite density?" A variety of candidate configurations have been proposed in the literature, most notably dyonic salt and baryonic popcorn, although finding which state (if either) is preferred has been severely hampered by numerical and analytical limitations.

Despite full numerical solutions still being beyond the scope of this thesis, we have nevertheless been able to make progress by utilising a variety of toy models and approximations to study the validity of common methods used to simplify the Sakai-Sugimoto model.

In Chapter 2 we studied a low-dimensional analogue of the Sakai-Sugimoto model in the form of an $O(3)$ sigma model coupled to a vector meson term. We were able to find full numerical solutions for solitons, multi-solitons and finite density configurations, and compare these with both solitons of the holographic baby Skyrme model and instanton approximations. All three solutions were found to be similar within a certain parameter regime, and qualitative differences between the vector meson and holographic baby Skyrme model solutions were found outside this regime. The vector meson solutions at finite density allowed us to explore whether a dyon salt or baryonic popcorn configuration was preferred at high densities. A series of popcorn transitions was found to be energetically favourable, which was then conjectured to continue indefinitely. This then allowed us to test some common approximations

used, namely approximating spacetime as flat (for small soliton size) and using a leading-order series expansion of the spacetime metric. Both approximations were found to be energetically very close to the true solutions in the parameter regime studied.

In Chapter 3 we studied the static solitons and multi-solitons of baby Skyrmions in AdS spacetime. The curvature of the underlying spacetime was found to act by adding an effective mass to the model, allowing us to investigate solutions to the equations of motion without an explicit mass term. Solitons for a wide range of topological charges were numerically calculated, with higher charge solutions taking the forms of concentric rings of soliton constituents. The transitions to extra layers were reminiscent of the baryonic popcorn transitions examined earlier. A point-particle approximation for this model was then developed, and was able to accurately replicate the ring-like structures of multi-solitons for a large number of charges, as well as estimate with good accuracy the topological charges at which further popcorn transitions would occur.

Finally, in Chapters 4 and 5 we studied homogeneous approximations to finite density configurations in a low-dimensional toy model and the full Sakai-Sugimoto model. The homogeneous approximation was found to have a good qualitative fit to the toy model at high baryon number densities, reproducing evidence for an infinite number of popcorn transitions as baryon number density increased further. The main drawback of the homogeneous toy model was that it was unable to produce analogues of the dyon salt phase: the solutions were forced to be "salty" due to the constraint of homogeneity.

When applied to the true Sakai-Sugimoto model, however, the homogeneous approximation yielded strikingly different results. Firstly we imposed homogeneity at the level of the gauge fields, leading to a singular model in which no clear analogue of the dyon salt phase could be found. However, applying homogeneity at the level of the field strengths allowed us to find a kink model in which analogues of both the dyon salt and baryonic popcorn phases could be numerically calculated and compared. The kink model predicted one single popcorn-like transition, beyond which the energetically favourable finite density solution took a new form: that of a soliton bag filled with abelian electric potential, with the baryon density localised around the surface of the bag. The previous success of the homogeneous

approximation in the toy model led us to believe that this difference in behaviour was likely due to fundamental differences between the Sakai-Sugimoto model and the low-dimensional toy model. In particular, it was suggested that the low-dimensional model is not a very good analogue to the full Sakai-Sugimoto model.

There are a number of potential directions further research into this topic could take. The first would be to explore properties of the Sakai-Sugimoto model at finite nonzero temperature [81]. At a critical temperature T_c the underlying geometry of the Sakai-Sugimoto model undergoes a transition, and becomes cylinder-shaped as opposed to cigar-shaped. This is interpreted as a quark confinement/deconfinement transition. In this regime the $D8/\overline{D8}$-brane pairs no longer necessarily merge and so chiral symmetry restoration in the model occurs above (or at, depending on the model parameters) the deconfinement temperature. Exploring solutions of the Sakai-Sugimoto model in the deconfined phase would be of phenomenological interest, such as in the context of heavy ion collisions in hot QCD [82], and analysis of high-density configurations would be a useful way of probing the QCD phase diagram.

Additional analysis of low-dimensional geometries as analogues of holographic QCD would also merit further study. As we discovered in Chapter 5, at least at the level of homogeneous approximations, static solutions of the Sakai-Sugimoto and holographic baby Skyrme models give qualitatively very different results. One potential cause of this is the fact that the two theories are fundamentally quite different: the higher-dimensional model is a gauge theory whereas the lower-dimensional analogue is an $O(3)$ sigma model. Whether or not a low-dimensional gauge theory analogue of the Sakai-Sugimoto could be found is still an open question and, if such a model existed and could qualitatively reproduce the results of the Sakai-Sugimoto model at high densities, it would provide a useful tool for further analysing the properties of holographic QCD.

In addition to this, there is more work that could be done studying the homogeneous approximations themselves. The homogeneous approximation used in Chapter 5 was not a true solutions to the equations of motion since the field equations were derived using the zero-curvature condition, which the homogeneous fields do not satisfy. However, as has been mentioned, replacing the spatial $\mathbb{R}^3$ with an S^3 allows homogeneous fields to be true solution to the equation of motion. This model has

been studied already [71] assuming the fields take self-dual form, but a more detailed numerical study would allow an investigation of how the bulk solitons explore the holographic direction in this geometry.

Although there are other avenues of research that could be taken to follow on from the work in this thesis, any work in this area will ultimately remain speculative until full numerical computations or more sophisticated analytical techniques can be applied to the full Sakai-Sugimoto model. Until then, this thesis has demonstrated that understanding the Sakai-Sugimoto model is an interesting and open question in theoretical physics with many features still left to be uncovered.

Appendix A

Numerical gradient flow methods

Throughout this thesis, a number of numerical field calculations are performed as a way of gaining insight into the various problems studied. Most of these calculations will involve the minimisation of some functional, usually an energy associated with the fields in a model, so this appendix will outline and discuss the numerical algorithms most commonly employed.

Consider some energy functional $E[\boldsymbol{\phi}(\boldsymbol{x})]$. An initial field configuration, $\boldsymbol{\phi}$, can be relaxed to a (local) minimum of E, by implementing a gradient flow, or heat flow, method. To do this we introduce an artificial time coordinate, t, and allow $\boldsymbol{\phi}$ to evolve via the first-order equation

$$\dot{\boldsymbol{\phi}} = -\frac{\delta E[\boldsymbol{\phi}]}{\delta \boldsymbol{\phi}} \tag{A.0.1}$$

where the overdot denotes differentiation with respect to t. It is easy to show that E decreases along trajectories of this evolution equation, and that stationary points satisfy $\frac{\delta E}{\delta \boldsymbol{\phi}} = 0$. Therefore, if E is taken to be the static energy of some system, this evolves the initial condition towards an energy minimising solution and thus gives static solutions to the field equations. This is a functional analogue of the steepest descent method used to minimise real-valued functions of many variables. If the initial conditions are chosen to be within a given topological sector then this enables us to find static soliton solutions with a given topological charge.

While this method usually converges even for poor choices of initial condition, its convergence is usually very slow. It can be shown that if we approximate the field on a

lattice with spacing Δx and approximate the time-steps between iterations by Δt then a necessary condition for numerical convergence is $\Delta t \leq \frac{1}{2}(\Delta x)^2$.

A numerical scheme with faster convergence can be obtained by replacing the left-hand side of equation (A.0.1) by $\ddot{\boldsymbol{\phi}}$. This we will refer to as a modified gradient flow method. Since this scheme is second-order in time derivatives, rather than first-order, numerical convergence now requires $\Delta t \leq \Delta x$.

This allows us to take much larger time-steps when numerically evolving initial conditions, aiding the speed of convergence. However, evolution of $\dot{\boldsymbol{\phi}}$ introduces extra kinetic energy into the system, so the algorithm typically oscillates around the energy minimising solution. This can be avoided by artificially introducing a damping term to (A.0.1) to remove this excess energy and allow much faster convergence than regular gradient flow methods. We will usually impose a damping procedure by artificially removing the kinetic energy of the fields under circumstances in which the energy of the fields begins to grow.

These methods were explored by numerically finding static solitons in the massive, flat-space baby Skyrme model. The Lagrangian density for this system is as in (1.2.17), subject to the constraint $\boldsymbol{\phi} \cdot \boldsymbol{\phi} = 1$. Numerically this can be accounted for by adding a Lagrange multiplier λ to the gradient flow equation via

$$\dot{\boldsymbol{\phi}} = -\frac{\delta E[\boldsymbol{\phi}]}{\delta \boldsymbol{\phi}} - \lambda \boldsymbol{\phi}\,. \tag{A.0.2}$$

The constraint implies $\dot{\boldsymbol{\phi}} \cdot \boldsymbol{\phi} = 0$, which then allows us to calculate the Lagrange multiplier at each numerical iteration, yielding:

$$\dot{\boldsymbol{\phi}} = -\frac{\delta E[\boldsymbol{\phi}]}{\delta \boldsymbol{\phi}} + \left(\frac{\delta E[\boldsymbol{\phi}]}{\delta \boldsymbol{\phi}} \cdot \boldsymbol{\phi}\right) \boldsymbol{\phi}\,. \tag{A.0.3}$$

Again, this flow equation can be replaced by one second-order in time derivatives to improve the speed of convergence. As was previously mentioned, this necessitates some damping mechanism to make the method more efficient - this was achieved numerically by forcing the first derivative $\dot{\boldsymbol{\phi}}$ back to zero each time the energy of the configuration began to increase.

Figure A.1 shows the rates of convergence for the different gradient flow methods discussed above when applied to finding the static baby Skyrmion in flat space with

$\kappa = 1$ and $m = \sqrt{1/10}$. Calculations were performed on a numerical grid with 201×201 gridpoints and $\Delta x = 0.2$. Derivatives were calculated using fourth-order accurate finite differences. We can clearly see the oscilliatory behaviour of the undamped modified gradient flow method and the significantly faster convergence rate of the damped modified gradient flow method.

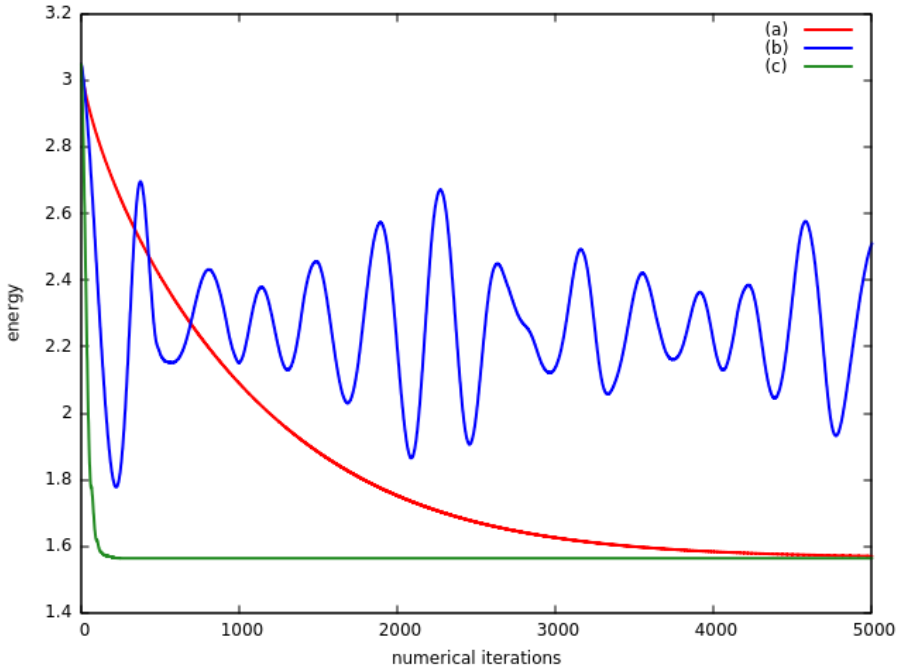

Figure A.1: Energies (in units of 4π) of the intermediate configurations during the calculation of the static flat-space baby Skyrmion with parameter values $\kappa = 1$ and $m = \sqrt{1/10}$ using (a) the usual gradient flow method with $\Delta t = 0.1(\Delta x)^2$, (b) the modified method with $\Delta t = 0.1\Delta x$, but without damping and (c) the modified method with damping.

Appendix B

Salt and homogeneity in the baby Skyrme model

Here we show that a salty ansatz is unavoidable when imposing periodicity in the (holographic) baby Skyrme model with the boundary conditions $\boldsymbol{\phi}(x,0) = (0,0,-1)$ and $\boldsymbol{\phi}(x,\infty) = (0,0,1)$. Note that the boundary condition at $z = 0$ corresponds to requiring a layer of solitonic material located there, and is unique to making the homogeneous ansatz. It is not a general feature of periodic baby Skyrmions.

The general form for the pion field $\boldsymbol{\phi}$ is given by

$$\boldsymbol{\phi}(x,z) = \left(f_1(x,z), f_2(x,z), \pm\sqrt{1-f_1^2-f_2^2}\right) , \tag{B.0.1}$$

and periodicity can be imposed in the x direction by expanding the functions f_1 and f_2 as Fourier series:

$$\begin{aligned} f_1(x,z) &= \sum_{n\in\mathbb{Z}} \alpha_n(z) e^{2in\pi x/L} , \\ f_2(x,z) &= \sum_{m\in\mathbb{Z}} \beta_m(z) e^{2im\pi x/L} . \end{aligned} \tag{B.0.2}$$

The boundary conditions then imply $\alpha_n(0) = \alpha_n(\infty) = \beta_m(0) = \beta_m(\infty) = 0$. The topological charge density of such a configuration is then given by

$$\mathcal{B} = -\frac{1}{4\pi}\boldsymbol{\phi}\cdot(\partial_x\boldsymbol{\phi}\times\partial_z\boldsymbol{\phi}) \tag{B.0.3}$$

$$= \frac{-1}{4\pi\sqrt{1-f_1^2-f_2^2}}\left(\partial_x f_1 \partial_z f_2 - \partial_x f_2 \partial_z f_1\right) \tag{B.0.4}$$

$$= \frac{-1}{2\sqrt{1-f_1^2-f_2^2}} \sum_{n,m} \frac{in}{L} \left(\alpha_n \beta'_m - \alpha'_m \beta_n\right) e^{2i(n+m)\pi x/L} \,. \tag{B.0.5}$$

We then see that the boundary conditions imply that $\mathcal{B}$ must vanish at $z = 0$ and $z = \infty$. In other words, the topological charge density, and therefore baryon number density, must be localised around a point away from $z = 0$. This means that, by imposing periodicity in the non-holographic direction, we have forced the homogeneous ansatz to be salty.

Appendix C

A homogeneous Skyrme crystal

In this appendix we consider the Skyrme model and explain how a homogeneous approximation may be thought of as a smeared version of the Skyrme crystal. This approximation is an unattainable idealisation that provides a lower bound on the energy of the true Skyrme crystal.

The static energy and baryon number (in Skyrme units) of the Skyrme model are given by

$$E = \frac{1}{2}\int \left\{ \mathrm{Tr}(R_i R_i) - \frac{1}{8}\mathrm{Tr}([R_i, R_j][R_i, R_j]) \right\} d^3\boldsymbol{x}\,, \tag{C.0.1}$$

$$B = \frac{i}{24\pi^2}\int \varepsilon_{ijk}\mathrm{Tr}(R_i R_j R_k)\, d^3\boldsymbol{x}\,, \tag{C.0.2}$$

where $R_i = i(\partial_i U)U^{-1}$ are the hermitian currents associated with the Skyrme field $U(\boldsymbol{x}) \in SU(2)$. The Fadeev-Bogomolny bound gives $E \geq 12\pi^2 B$, but this cannot be saturated for nonzero B since it would require the Skyrme field to be an isometry from $\mathbb{R}^3$ to $SU(2)$, which are not isometric spaces.

The energy minimising solution closest to the bound is the triply periodic Skyrme crystal [59, 60], which has energy per baryon $E/B = 12\pi^2 \times 1.04$. The crystal is formed on a cubic lattice of side length $L = 4.7$ containing four Skyrmions, giving rise to a baryon number density $\mathcal{B} = 4/L^3 = 0.04$.

Substituting an idealised homogeneous ansatz $R_i = -\beta\sigma_i/2$ into (C.0.1) and (C.0.2) yields energy per unit volume $\mathcal{E}$ and baryon number density $\mathcal{B}$ as

$$\mathcal{E} = \frac{3}{4}\beta^2 + \frac{3}{16}\beta^4\,, \qquad\qquad \mathcal{B} = \frac{1}{16\pi^2}\beta^3\,. \tag{C.0.3}$$

We can then recover the Fadeev-Bogomolny bound via a simple manipulation:

$$\mathcal{E} = \frac{3}{4}\left(\beta - \frac{1}{2}\beta^2\right)^2 + \frac{3}{4}\beta^3 \geq \frac{3}{4}\beta^3 = 12\pi^2\mathcal{B}\,. \tag{C.0.4}$$

Within the homogeneous approximation, the bound is attained by the value $\beta = 2$, which corresponds to baryon number density $\mathcal{B} = 1/(2\pi^2) = 0.05$. These values provide a good estimate of both the energy and baryon number density of the Skyrme crystal, and also provide a lower bound for the true Skyrme crystal energy since there are no Skyrme fields that can generate the idealised homogeneous currents required to attain the bound.

Bibliography

[1] T. Sakai and S. Sugimoto, *Low energy hadron physics in holographic QCD*, *Prog.Theor.Phys.* **113** (2005) 843, [hep-th/0412141].

[2] T. Sakai and S. Sugimoto, *More on a holographic dual of QCD*, *Prog.Theor.Phys.* **114** (2005) 1083, [hep-th/0507073].

[3] M. Rho, S.-J. Sin, and I. Zahed, *Dense QCD: a holographic dyonic salt*, *Phys.Lett.* **B689** (2010) 23, [arXiv:0910.3774].

[4] V. Kaplunovsky, D. Melnikov, and J. Sonnenschein, *Baryonic popcorn*, *JHEP* **1211** (2012) 047, [arXiv:1201.1331].

[5] V. Kaplunovsky, D. Melnikov, and J. Sonnenschein, *Holographic baryons and instanton crystals*, *Mod. Phys. Lett.* **B29** (2015) 1540052, [arXiv:1501.04655].

[6] M. Elliot-Ripley, *Phases and approximations of baryonic popcorn in a low-dimensional analogue of holographic QCD*, *J.Phys.* **A48** (2015) 295402, [arXiv:1503.08755].

[7] M. Elliot-Ripley and T. Winyard, *Baby Skyrmions in AdS*, *JHEP* **09** (2015) 009, [arXiv:1507.05928].

[8] M. Elliot-Ripley, *Salty popcorn in a homogeneous low-dimensional toy model of holographic QCD*, *J. Phys.* **A50** (2017), no. 14 145401, [arXiv:1610.09169].

[9] M. Elliot-Ripley, P. Sutcliffe, and M. Zamaklar, *Phases of kinky holographic nuclear matter*, *JHEP* **10** (2016) 088, [arXiv:1607.04832].

[10] J. S. Russell, *Report on waves*, *Proceedings of the British Association for the Advancement of Science, 14th meeting* (1845) 311–390.

[11] D. J. Korteweg and G. de Vries, *On the change of form of long waves advancing in a rectangular canal, and on a new type of long stationary waves*, *Philosophical Magazine Series 5* **39** (1895) 422.

[12] T. Skyrme, *A nonlinear field theory*, *Proc.Roy.Soc.Lond.* **A260** (1961) 127.

[13] T. H. R. Skyrme, *A unified field theory of mesons and baryons*, *Nucl. Phys.* **31** (1962) 556.

[14] P. W. Anderson and G. Toulouse, *Phase slippage without vortex cores: vortex textures in superfluid* ^{3}He, *Phys. Rev. Lett.* **38** (Feb, 1977) 508.

[15] J. Ketterson and S. Song, *Superconductivity*. Cambridge University Press, 1999.

[16] T. W. B. Kibble, *Topology of cosmic domains and strings*, *Journal of Physics A: Mathematical and General* **9** (1976), no. 8 1387.

[17] G. 't Hooft, *Magnetic monopoles in unified gauge theories*, *Nucl. Phys.* **B79** (1974) 276.

[18] J. Preskill, *Cosmological production of superheavy magnetic monopoles*, *Phys. Rev. Lett.* **43** (1979) 1365.

[19] M. Chernodub, S. Hu, and A. J. Niemi, *Topological solitons and folded proteins*, *Phys. Rev. E* **82** (Jul, 2010) 011916.

[20] A. Krokhotin, A. J. Niemi, and X. Peng, *Soliton concepts and protein structure*, *Phys. Rev. E* **85** (Mar, 2012) 031906.

[21] T. H. R. Skyrme, *Particle states of a quantized meson field*, *Proc. Roy. Soc. Lond.* **A262** (1961) 237.

[22] E. B. Bogomolny, *Stability of classical solutions*, *Sov. J. Nucl. Phys.* **24** (1976) 449.

[23] M. Ablowitz and P. Clarkson, *Solitons, Nonlinear Evolution Equations and Inverse Scattering*. Cambridge Studies in Social an. Cambridge University Press, 1991.

[24] J. K. Perring and T. H. R. Skyrme, *A model unified field equation*, *Nucl. Phys.* **31** (1962) 550.

[25] G. H. Derrick, *Comments on nonlinear wave equations as models for elementary particles*, *J. Math. Phys.* **5** (1964) 1252.

[26] W. J. Zakrzewski, *Low dimensional sigma models*, in *DPF '88: 1988 Meeting of the Division of Particles & Fields of the APS Storrs, Connecticut, August 15-18, 1988*, p. 790, 1989.

[27] N. Manton and P. Sutcliffe, *Topological Solitons:*. Cambridge University Press, Cambridge, 006, 2004.

[28] B. Piette, B. Schroers, and W. Zakrzewski, *Multisolitons in a two-dimensional Skyrme model*, *Z.Phys.* **C65** (1995) 165, [hep-th/9406160].

[29] S. L. Sondhi, A. Karlhede, S. A. Kivelson, and E. H. Rezayi, *Skyrmions and the crossover from the integer to fractional quantum Hall effect at small Zeeman energies*, *Phys. Rev.* **B47** (1993) 16419.

[30] X. Yu, Y. Onose, N. Kanazawa, J. Park, J. Han, Y. Matsui, N. Nagaosa, and Y. Tokura, *Real-space observation of a two-dimensional skyrmion crystal*, *Nature* **465** (2010) 901.

[31] E. Witten, *Baryons in the 1/N expansion*, *Nucl. Phys.* **B160** (1979) 57.

[32] E. Witten, *Global aspects of current algebra*, *Nucl. Phys.* **B223** (1983) 422.

[33] E. Witten, *Current algebra, baryons, and quark confinement*, *Nucl. Phys.* **B223** (1983) 433.

[34] R. Battye, N. S. Manton, and P. Sutcliffe, *Skyrmions and the alpha-particle model of nuclei*, *Proc. Roy. Soc. Lond.* **A463** (2007) 261, [hep-th/0605284].

[35] R. A. Battye, N. S. Manton, P. M. Sutcliffe, and S. W. Wood, *Light nuclei of even mass number in the Skyrme model*, *Phys. Rev.* **C80** (2009) 034323, [arXiv:0905.0099].

[36] G. S. Adkins, C. R. Nappi, and E. Witten, *Static properties of nucleons in the Skyrme model*, *Nucl. Phys.* **B228** (1983) 552.

[37] G. S. Adkins and C. R. Nappi, *The Skyrme model with pion masses*, *Nucl. Phys.* **B233** (1984) 109.

[38] P. Sutcliffe, *Skyrmions in a truncated BPS theory*, *JHEP* **04** (2011) 45, [arXiv:1101.2402].

[39] C. Adam, J. Sanchez-Guillen, and A. Wereszczynski, *A Skyrme-type proposal for baryonic matter*, *Phys. Lett.* **B691** (2010) 105, [arXiv:1001.4544].

[40] D. Harland, *Topological energy bounds for the Skyrme and Faddeev models with massive pions*, *Phys. Lett.* **B728** (2014) 518, [arXiv:1311.2403].

[41] M. Gillard, D. Harland, and M. Speight, *Skyrmions with low binding energies*, *Nucl. Phys.* **B895** (2015) 272, [arXiv:1501.05455].

[42] S. B. Gudnason, *Loosening up the Skyrme model*, *Phys. Rev.* **D93** (2016), no. 6 065048, [arXiv:1601.05024].

[43] A. A. Belavin, A. M. Polyakov, A. S. Schwartz, and Yu. S. Tyupkin, *Pseudoparticle Solutions of the Yang-Mills Equations*, *Phys. Lett.* **B59** (1975) 85–87.

[44] M. F. Atiyah, N. J. Hitchin, V. G. Drinfeld, and Yu. I. Manin, *Construction of instantons*, *Phys. Lett.* **A65** (1978) 185.

[45] M. Atiyah and N. Manton, *Skyrmions from instantons*, *Phys.Lett.* **B222** (1989) 438.

[46] P. Sutcliffe, *Skyrmions, instantons and holography*, *JHEP* **1008** (2010) 019, [arXiv:1003.0023].

[47] J. M. Maldacena, *The large N limit of superconformal field theories and supergravity*, *Int.J.Theor.Phys.* **38** (1999) 1113, [hep-th/9711200].

[48] K. Peeters and M. Zamaklar, *The string/gauge theory correspondence in QCD*, *Eur. Phys. J. ST* **152** (2007) 113, [arXiv:0708.1502].

[49] J. Polchinski, *String Theory: Volume 2, Superstring Theory and Beyond*. Cambridge Monographs on Mathematical Physics. Cambridge University Press, 1998.

[50] S. Bolognesi and P. Sutcliffe, *The Sakai-Sugimoto soliton*, *JHEP* **1401** (2014) 078, [arXiv:1309.1396].

[51] S. Baldino, S. Bolognesi, S. B. Gudnason, and D. Koksal, *A solitonic approach to holographic nuclear physics*, arXiv:1703.08695.

[52] D. K. Hong, M. Rho, H.-U. Yee, and P. Yi, *Chiral dynamics of baryons from string theory*, *Phys.Rev.* **D76** (2007) 061901, [hep-th/0701276].

[53] H. Hata, T. Sakai, S. Sugimoto, and S. Yamato, *Baryons from instantons in holographic QCD*, *Prog.Theor.Phys.* **117** (2007) 1157, [hep-th/0701280].

[54] M. A. Stephanov, *QCD phase diagram: An overview*, *PoS* **LAT2006** (2006) 024, [hep-lat/0701002].

[55] M. G. Alford, K. Rajagopal, and F. Wilczek, *QCD at finite baryon density: Nucleon droplets and color superconductivity*, *Phys. Lett.* **B422** (1998) 247, [hep-ph/9711395].

[56] L. McLerran and R. D. Pisarski, *Phases of cold, dense quarks at large N(c)*, *Nucl. Phys.* **A796** (2007) 83, [arXiv:0706.2191].

[57] J. de Boer, B. D. Chowdhury, M. P. Heller, and J. Jankowski, *Towards a holographic realization of the Quarkyonic phase*, *Phys. Rev.* **D87** (2013), no. 6 066009, [arXiv:1209.5915].

[58] M. Rozali, H.-H. Shieh, M. Van Raamsdonk, and J. Wu, *Cold nuclear matter in holographic QCD*, *JHEP* **01** (2008) 053, [arXiv:0708.1322].

[59] M. Kugler and S. Shtrikman, *A new Skyrmion crystal*, *Phys. Lett.* **B208** (1988) 491.

[60] M. Kugler and S. Shtrikman, *Skyrmion crystals and their symmetries*, *Phys. Rev.* **D40** (1989) 3421.

[61] K.-M. Lee and C.-h. Lu, *SU(2) calorons and magnetic monopoles*, *Phys. Rev.* **D58** (1998) 025011, [hep-th/9802108].

[62] S. Bolognesi and P. Sutcliffe, *A low-dimensional analogue of holographic baryons*, *J.Phys.* **A47** (2014) 135401, [arXiv:1311.2685].

[63] D. Foster and P. Sutcliffe, *Baby Skyrmions stabilized by vector mesons*, *Phys.Rev.* **D79** (2009) 125026, [arXiv:0901.3622].

[64] M. Atiyah and P. Sutcliffe, *Skyrmions, instantons, mass and curvature*, *Phys.Lett.* **B605** (2005) 106, [hep-th/0411052].

[65] T. Winyard, *Hyperbolic Skyrmions*, arXiv:1503.08522.

[66] S. Bolognesi and D. Tong, *Monopoles and holography*, *JHEP* **1101** (2011) 153, [arXiv:1010.4178].

[67] P. Sutcliffe, *Monopoles in AdS*, *JHEP* **1108** (2011) 032, [arXiv:1104.1888].

[68] P. Salmi and P. Sutcliffe, *Aloof baby Skyrmions*, *J.Phys.* **A48** (2015) 035401, [arXiv:1409.8176].

[69] R. S. Palais, *The principle of symmetric criticality*, *Comm.Math.Phys.* **69** (1979) 19.

[70] R. L. Graham, B. D. Lubachevsky, K. J. Nurmela, and P. R. Östergård, *Dense packings of congruent circles in a circle*, *Discrete Mathematics* **181** (1998) 139.

[71] K.-Y. Kim, S.-J. Sin, and I. Zahed, *Dense holographic QCD in the Wigner-Seitz approximation*, *JHEP* **09** (2008) 001, [arXiv:0712.1582].

[72] S. Bolognesi, *Multi-monopoles and magnetic bags*, *Nucl. Phys.* **B752** (2006) 93, [hep-th/0512133].

[73] S. Bolognesi, *Instanton bags, high density holographic QCD and chiral symmetry restoration*, *Phys. Rev.* **D90** (2014), no. 10 105015, [arXiv:1406.0205].

[74] K.-Y. Kim, S.-J. Sin, and I. Zahed, *Dense hadronic matter in holographic QCD*, *J. Korean Phys. Soc.* **63** (2013) 1515, [hep-th/0608046].

[75] N. Horigome and Y. Tanii, *Holographic chiral phase transition with chemical potential*, *JHEP* **01** (2007) 072, [hep-th/0608198].

[76] S. Kobayashi, D. Mateos, S. Matsuura, R. C. Myers, and R. M. Thomson, *Holographic phase transitions at finite baryon density*, *JHEP* **02** (2007) 016, [hep-th/0611099].

[77] S. K. Domokos and J. A. Harvey, *Baryon number-induced Chern-Simons couplings of vector and axial-vector mesons in holographic QCD*, *Phys. Rev. Lett.* **99** (2007) 141602, [arXiv:0704.1604].

[78] N. S. Manton, *Monopole planets and galaxies*, *Phys. Rev.* **D85** (2012) 045022, [arXiv:1111.2934].

[79] F. Preis and A. Schmitt, *Layers of deformed instantons in holographic baryonic matter*, *JHEP* **07** (2016) 001, [arXiv:1606.00675].

[80] F. Preis and A. Schmitt, *Phases of dense matter with holographic instantons*, in *12th Conference on Quark Confinement and the Hadron Spectrum (Confinement XII) Thessaloniki, Greece, August 28-September 2, 2016*, 2016. arXiv:1611.05330.

[81] O. Aharony, J. Sonnenschein, and S. Yankielowicz, *A Holographic model of deconfinement and chiral symmetry restoration*, *Annals Phys.* **322** (2007) 1420–1443, [hep-th/0604161].

[82] J. Casalderrey-Solana, H. Liu, D. Mateos, K. Rajagopal, and U. A. Wiedemann, *Gauge/String Duality, Hot QCD and Heavy Ion Collisions*, arXiv:1101.0618.